JYU DISSERTATIONS 544

Teemu Järvinen

Molecular Dynamics View on Matrix Isolation

UNIVERSITY OF JYVÄSKYLÄ
FACULTY OF MATHEMATICS
AND SCIENCE

JYU DISSERTATIONS 544

Teemu Järvinen

Molecular Dynamics View on Matrix Isolation

Esitetään Jyväskylän yliopiston matemaattis-luonnontieteellisen tiedekunnan suostumuksella
julkisesti tarkastettavaksi Ylistönrinteen auditoriossa KEM4
elokuun 15. päivänä 2022 kello 12.

Academic dissertation to be publicly discussed, by permission of
the Faculty of Mathematics and Science of the University of Jyväskylä,
in building Ylistönrinne, auditorium KEM4, on August 15, 2022, at 12 o'clock.

JYVÄSKYLÄN YLIOPISTO
UNIVERSITY OF JYVÄSKYLÄ

JYVÄSKYLÄ 2022

Editors
Jan Lundell
Department of Chemistry, University of Jyväskylä
Päivi Vuorio
Open Science Centre, University of Jyväskylä

ISBN 978-951-39-9356-6 (PDF)
URN:ISBN:978-951-39-9356-6
ISSN 2489-9003

Permanent link to this publication: http://urn.fi/URN:ISBN:978-951-39-9356-6

SUPERVISOR
Jan Lundell
University of Jyväskylä

PRE-REVIEWERS
Martin Suhm
Georg-August-Universität Gottingen

Juha Vaara
University of Oulu

OPPONENT
Kari Laasonen
Aalto University

ACKNOWLEDGEMENTS

First and foremost, I would like to thank you my supervisor professor Jan Lundell, for offering me a position to do this Thesis in Jyväskylä.

The work on this Thesis started in University of Wrocław at autumn 2015, where I was introduced to a beautiful county called Poland and the wonderful people who live there. First, I would like to thank you professor Zdzisław Latajka for welcoming me to his group. A great thank you also belongs to Dr. Przemysław Dopieralski, who taught me to do molecular dynamics. I would also like to thank Dr. Adriana Olbert-Majkut, for helping to organize an apartment in Wrocław and professor Sławomir Berski, for teaching me a lot about Polish culture, as well as telling me a lot of other stories.

I am also indebted to professor Dage Sundhom and, by now Dr., Maria Dimitrova from University of Helsinki, who were working on benzene matrix spectra that was left by Dr. Leonid Khriachtchev, after his unfortunate passing away. I ended up helping them on the benzene spectra, which ended up to be a major part of the Thesis. I am also very happy that we managed to mostly finish the work Leonid started, as we all felt that we needed to do it to honor Leonid's memory. I would also like to thank Dr. Markus Metsälä for looking Leonid's records and finding additional spectra and laboratory notes that were essential in interpreting the spectra.

I will also like to thank my fellow Ph.D. students in Jyväskylä, for our common journey and all the people who taught me in Jyväskylä.

I am also grateful for professors Martin Schum and Juha Vaara for reviewing the Thesis and suggesting improvements.

This work would not have been possible without the financial help that I got Erasmus program and Academy of Finland projects 258806, 286644 and 332023. The computational resources of the CSC where also an absolute necessity to complete this work.

Lastly, I need to mention my high school chemistry teacher Mauri Toivonen. Who forced me to take part of the national chemistry competition and thus started the events that lead to this Thesis.

Helsinki, July 2022

Teemu Järvinen

ABSTRACT

Ability to identify different molecules is one of key goals in chemistry. A common modern way is to identify molecules based on their vibrations that can be detected by infrared spectroscopy or vibrational Raman spectroscopy. This is the way how molecules are identified in matrix isolation experiments, where individual molecules or molecule clusters are enclosed in solid noble gas or nitrogen matrix, an inert environment that allows long term storage of highly reactive molecules and radicals.

Surrounding matrix changes the infrared signal of the molecules enclosed within, by changing the shape of observed vibrational transtions and possibly causing extra peaks to appear. While these rarely prevent identification, it is important to understand where these effects originate, as it gives us information how the matrix atoms are positioned around the embedded molecule(s), called as local site structure. They will give information on how reactions happen in the matrix and where the extra structures in the observed spectra originate.

This Thesis introduces a way to calculate these matrix effects based on molecular dynamics. The method also allows modeling of chemical reactions within the matrix. Resulting calculations present novel information about local site structures of certain molecule and some results on dynamical behavior of vibrationally induced reactions. Such insights include answers to some decades old questions on the local structures and their spectroscopic evidences in the experimental investigations.

In the future the method presented here, and the suggested future developments are likely to become a standard part of matrix isolation experiments. Such an approach as presented here could open up a new era in matrix isolation field, where the matrix effects appearing and observed in experimental spectra can be consistently understood and the reactions therein may be modeled with good accuracy.

TIIVISTELMÄ

Kyky tunnistaa eri molekyyleja on yksi kemian päätavoitteista. Yleinen nykyaikainen menetelmä on havainnoida molekyylien värähtelyä infrapunaspektrin tai Raman-spektroskopian avulla. Tätä menetelmää käytetään matriisieristyskokeissa, joissa yksittäisiä molekyyleja tai komplekseja eristetään kiinteän jalokaasusta tai typestä tehtyyn matriisiin. Tällöin alhaisissa lämpötiloissa kiinteytyvä jalokaasuympäristö on inertti ympäristö, jossa voidaan säilöä kemiallisesti reaktiivisia molekyyleja ja radikaaleja.

Tutkittavia molekulaarisia systeemejä ympäröivä matriisi vaikuttaa sen sisällä olevien molekyylien värähdyksiin, jonka seurauksena spektroskopialla nähtävissä signaaleissa on muutoksia. Vaikka nämä muutokset eivät yleensä estä molekyylien tunnistamista, on muutosten alkuperän ymmärtäminen tärkeää. Se antaa informaatiota, jolla voidaan selvittää, miten matriisin atomit ovat asettuneet tutkittavan molekyylin ympärille. Tästä käytetään termiä saittirakenne, joka tarkoitaa matriisissa esiintyviä paikallisia, lokaaleja rakenteita. Nämä paikalliset rakenteet ovat spektroskooppisesti havaittavia ja tunnistettavia, jotka puolestaan antavat viitteitä siitä, miten kemialliset reaktiot matriisissa tapahtuvat ja mistä spektrissä nähtävät erilaiset rakenteet syntyvät.

Tämä väitöskirja esittelee menetelmän, jolla näitä matriisin aiheuttamia muutoksia voidaan mallintaa perustuen molekyylidynamiikkaan. Menetelmä mahdollistaa myös kemiallisten reaktioiden mallintamisen matriisissa. Menetelmän avulla lasketut tuloksen sisältävät uutta tietoa tiettyjen molekyylien saittirakenteista ja molekyylien värähtelyjen kautta käynnistetyistä reaktioista. Tulokset sisältävät vastauksia muutamiin vuosikymmeniä vanhoihin ongelmiin, jotka käsittelevät kiinteän matriisiympäristön vaikutuksia kemiallisten systeemien rakenteisiin ja spektroskopiaan.

Tulevaisuudessa tässä väitöskirjassa esitetyistä menetelmästä ja kehitys ehdotuksista, kehitysehdotuksista voi tulla todennäköisesti osa standardia laskennallista tutkimusta matriisieristyskokeiden tukemisessa. Tämä mahdollistaa tällä tutkimuksen saralla uuden aikakauden, jolloin matriisin aiheuttamat muutokset spektriin on järjestäen ymmärrettävissä ja reaktiot ovat mallinnettavissa riittävällä atomitason tarkkuudella.

PUBLICATIONS

[1] T. Järvinen, J. Lundell and P. Dopieralski. Ab initio molecular dynamics study of overtone excitations in formic acid and its water complex. *Theor Chem Acc* **137,** 100 (2018).

AUTHOR CONTRIBUTIONS

ARTICLE [1] Performed all the calculations, devised the excitation method and wrote the article.

MONOGRAPH Developed the programs, invented the calculation scheme, performed all the calculations and interpreted the spectra.

CONTENTS

LIST OF FIGURES

LIST OF TABLES

ACRONYMS

AIMD ab initio molecular dynamics

AO atomic orbital

AD automatic differentation

CC couple cluster

BOMD Born-Oppenheimer molecular dynamics

BSSE basis set superposition error

CCSD coupled cluster singlets and doublets

CCSD(T) coupled cluster single, double and perturbative triple

CCSDT coupled cluster singlets, doublets and triplets

CI configuration interaction

CISD configuration interaction single and double

CISDT configuration interaction single, double and triple

CPMD Car-Parrinello molecular dynamics

cFA cis-formic acid

CoM center of mass

CSVR canonical sampling through velocity rescaling

DDR Darling-Dennison resonance

DE differential equation

DFT density functional theory

DoS density of states

F12 explicity correlated

FA formic acid

fcc face-centered cubic

FR Fermi resonance

FCI full configuration interaction

FWHM full width half maximum

GGA generalized gradient approximation

GOT great orthogonality theorem

GTO gaussian type orbital

GVPT general vibrational perturbation theory

HF Hartree-Fock

IR infrared

KS Kohn-Sham theory

LCAO linear combination of atomic orbitals

LDA local density approximation

LSDA local spin density approximation

MD molecular dynamics

MI matrix isolation

MM molecular mechanics

MP2 Møller-Plesset perturbation theory

NPT constant particle number, pressure and temperature

NVE constant particle number, volume and energy

NVT constant particle number, volume and temperature

PW plane-wave

PES potential energy surface

QED quantum electrodynamics

QM quantum mechanics

QM/MM quantum-mechanical molecular-mechanical

RDF radial distribution function

RMSD root-mean-square deviation

RTE Renner-Teller effect

PES Potential Energy Surface

SO special orthogonal group

SO(3) 3-dimensional special orthogonal group

SU special unitary group

SU(2) 2-dimensional special unitary group

tFA trans-formic acid

U Unitary Group

U(N) N-dimensional unitary group

VCC vibrational coupled cluster

VCI vibrational configuration interaction

VDMRG vibrational density matrix renormalization group

VMP2 vibrational second order Møller-Plesset theory

VPT2 vibrational perturbation theory 2

VSCF vibrational self-consistent field

WKB Wentzel–Kramers–Brillouin approximation

1 INTRODUCTION

Matrix isolation (MI) spectroscopy [1, 2] is a method where a gas phase noble gas or some other inert gas has an added impurity. When this gas mixture is then condensed to solid in low temperatures the impurity molecules became trapped inside the solid noble gas, called as (host) matrix.

This process of condensing pre-prepared gas mixture or separate gaseous samples mixed with matrix host gas is called as deposition. It produces a solid where individual molecules are isolated by surrounding matrix molecules. It can also produce molecule clusters depending on mixture ratio, with typically rations 1:1000 to 1:10000 being used to generate isolated molecules [3].

The deposited molecules can be detected using, for example, optical spectroscopy and they can be irradiated with lasers to induce chemical reactions. Because noble gases are chemically inert it is possible to produce and store highly reactive, high energy compounds and radicals, such as individual fluorine atoms or argon compounds [4].

Because temperatures of solid noble gases are close to absolute zero the reactions are low temperature by nature. Meaning that matrix isolation as a technique is well suited to study naturally occurring environments like atmospheric chemistry or astrochemistry. An example of an atmospheric reaction studied by MI is the mixture of N_2O and H_2O in matrix [5]. Radiating the sample dissociates N_2O to N_2 and O. Annealing at ~25 K causes the O atoms to move in the solid environment, and to form $H_2O \cdots O$ complex. Subsequent irradiation of the sample with 300 nm irradiation causes the complex to rearrange to H_2O_2 with 50% total yield.

The movement of the trapped atoms depends on the level of delocalization of host matrix atoms [6]. With heavier atoms having smaller zero-point motion, this leads to lower mobility. Increasing temperature causes the host atoms to move more resulting in higher mobility. The exception is He, which forms superfluid [6] instead of solid in normal pressure under 2.18 K. The main defining feature of superfluid is that it has no viscosity resulting in frictionless motion of objects in it. Superfluid helium can be used as matrix, but the experiments need to be done in droplets due to extremely small solubility of foreign species in the superfluid. Therefore, different equipment is needed for superfluid helium experiments compared with MI in the temperature range of 5-50 K.

The type of experiments of interest in this Thesis are vibration overtone-induced reactions in low temperature matrix environment. This type of reaction is not as common as electronic excitation reactions, but there is a large set of literature of it [7–12] adopted to study molecular rearrangements induced by infrared light.

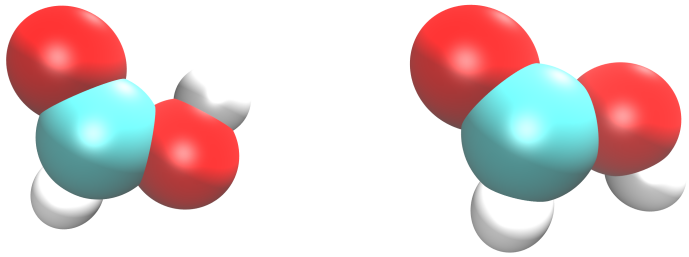

(a) (b)

Figure 1.1: Formic acid trans (a) and cis (b) conformers

The initial article that started the study of overtone-induced reactions in MI was published by Pettersson et al. [13], in which exciting OH vibration mode of formic acid to first overtone resulted in a conformational change. This allowed production of cis-formic acid Figure 1.1 that then could be further studied.

The next advancement happened when it was discovered that using visible laser it is possible to excite high vibrational overtones [14]. In such experiment the 532 nm laser was used to excite the same OH mode to sixth excited state, and the same change of conformers resulted. Today, there is an extensive amount of publications related to overtone-induced chemistry in matrix [15–39], to name a few.

It has become a normal procedure along low temperature MI experiments that experimental studies are accompanied by calculations for vibrational levels which are used to interpret the spectra. These calculations are done for isolated gas phase molecules, which differs from the experimental spectra of molecules trapped in matrix. The concept of matrix effect is used to describe the changes that matrix causes to the observed spectrum compared with gas-phase vibrational data. These effects arise from interaction between the studied molecule and matrix atoms.

A common effect in MI-studies is to find that molecule rotation is suppressed. This is demonstrated in the experimentally recorded spectrum as the disappearance of rotation branches. An other effect is that in many cases there are multiple peaks instead of one. The main reason behind this is the different positions of host matrix atoms around the trapped molecule, which causes small changes to the vibrational frequencies. These changes are then detected as individual peaks. The different positions are called as *sites*.

The gas-phase calculations do not include matrix effects and normally there is no information on what kind of structures are behind the different sites in the solid matrix. The main goal of this Thesis was to develop methods which would allow us to take into account the effects that matrix causes. This was done by developing a quantum-mechanical molecular-mechanical (QM/MM) framework for MI, where the matrix is modeled classically and the deposited molecules quantum mechanically. Spectra are calculated using molecular dynamics (MD).

With MD it is also possible to simulate overtone excitations and this was also explored in this Thesis.

Part I

LITERATURE REVIEW

2

SYMMETRY

Normally symmetry is used in chemistry as a way of classification or to assign an integral to be zero [40]. These both are very useful tools, but the problem here is that for many chemists, these are the only ways they understand symmetry.

One goal in this Thesis is to introduce a broader view of symmetry, by demonstrating how symmetry can be used as a tool to create scientific theories. Or, rather that scientific theories can be expressed as symmetries in higher level of abstraction, and a lower level of abstraction can be generated from the symmetry version. In this way, an extremely compact and clean way of deriving sometimes difficult results can be achieved with ease.

In the case of this Thesis symmetry principles allow easy derivation of molecular vibrations, statistical mechanics and some aspects of theoretical and computational chemistry like coupled-cluster theory.

2.0.1 *Historical Development of Symmetry*

Historically[1] the way of how symmetry was used in language was different from today. Modern use of symmetry is based on explicit notation, while implicit notation was used earlier.

Explicit notation was introduced in 19th century in a form of classification of crystal structures. Nevertheless, a crucial change in symmetry thinking took place with the development of group theory. This enabled attribution of symmetry to abstract concepts like laws of physics or to mathematical concepts. We can, for example, say that sine is an odd function while cosine is even, which is an application symmetry to mathematical functions.

This way of using symmetry is called as using *symmetry principles* as opposed to *symmetry arguments* that is deriving consequences based of symmetry of physical situation or phenomena.

A good example of symmetry arguments is Archimedes's equilibrium law for the balance: if equal weights are hung at equal distances along the arms of a balance, then it will remain in equilibrium since there is no reason for it to rotate one way or the other about the balance point.

Another important development in symmetry thinking was related to the relationship between physical theory and symmetry. Originally the relationship was that symmetry was a feature of theory. This way of thinking persisted a long time. Even though the first use of thinking in an opposite way was introduced by Galileo in 1632, when he argued that one can not experimentally verify, whether or not a

1 *Symmetries in Physics: Philosophical Reflections* [41] is a good reference for the development of symmetry and its applications and this section is based on it.

ship is stationary or moving smoothly, when the experiments are done inside the cabin of the ship. This symmetry that assumes similarity between rest and certain kind of movement is better know as *Galilean principle of relativity*.

It should be noted here that even though this was before Newton published his theory of mechanics, he did still state, in a corollary of *Principia*, that Galilean principle of relativity was a consequence of his laws of mechanics, not the other way around.

The change in the direction of thinking happened when Einstein published *special relativity* in 1905. Here the starting point was that speed of light is the same for everyone. Therefore, this is starting with a symmetry statement that is followed by a derivation of a theory from it. Later on, this way of creating theories has become a standard way in particle physics, like in formulation of the *standard model* [42]. While it is used less across the disciplines of physics and chemistry, it can be used to derive all the theories of physics and, thus, also chemistry.

Galilean principle of relativity and *special relativity* are examples of what are called as *geometrical symmetries*. In the beginning of 20th century new kind of symmetries were also discovered that are not related to geometry. These are called as *dynamical symmetries*. Good examples of dynamical symmetries are *permutation symmetry* of fermions and bosons, as well as $U(1)$ symmetry of *quantum electrodynamics* (QED).

Another important development happened in the beginning of 20th century, when Emmy Noether published her famous theories in 1918.[2] These state that every symmetry operation has an associated conservation law. For example, conservation of momentum follows from uniform space symmetry. It is also believed that all measurable quantities are conserved quantities of some symmetry operation [42], like energy is related to time symmetry and temperature to irrelevance of zero energy level.

2.1 GROUP THEORY

Mathematical definition of a *group* is a set of G together with a law of composition that has following axioms [44–46]

Sometimes closure is omitted from the definition, but it is good to emphasize it for the case that G is a subgroup.

1. **Closure,** if $g, h \in G$ then composition $k = gh \in G$
2. **Associativity**, $g(hk) = (gh)k$, for all $g, h, k \in G$
3. **Identity element**, there exist an element $e \in G$, such that
$$eg = ge = g \quad \text{for all } g \in G$$
4. **Inverse**, for each $g \in G$ there is $g^{-1} \in G$ such that
$$gg^{-1} = g^{-1}g = e.$$

If group satisfies an additional property

$$gh = hg \quad \text{for all } g, h \in G$$

2 For a mathematical introduction to Noether's theories see [43], for philosophical one see [41].

it is called *Abelian*. A *subgroup* is a subset of a group that satisfies all the group axioms.

2.2 FINITE GROUPS

In *finite groups* number of group/symmetry elements is countable. Common shapes like cube, triangle and octahedron belong to this category.

In the context of chemistry, there are two categories of symmetry addressing individual molecules and solid-state crystals. The difference between these two is that in crystals there exist translation symmetry, which is not present in individual molecules. There are total of 32 *crystallographic symmetry groups* and in theory an infinite amount of *molecular symmetry groups* [47]. Usually, molecular groups are among the 32 crystallographic ones. There is a different naming convention for these two categories and the one presented here is the molecular point group one.

The term *point group* is given to symmetry groups which have a common point shared by all symmetry operations. There are 5 types of different symmetry operations [47, 48]

E Identity operation

C_n rotation of angle $\frac{2\pi}{n}$

σ reflection by plane (symmetry plane)

S_n improper rotation - rotation of C_n and reflection in rotation plane afterwards

i inversion of coordinates around a point.

Of these, σ can be further divided to σ_v and σ_h for vertical and horizontal with respect to the highest rotation axis and σ_d for other rotation axes.

All point groups belong to *matrix groups*, a set of matrices that reproduce group multiplication when using matrix product as a group operation. This is an example of *group representation theory*, which in general means *homomorphism* of abstract group to some concrete mathematical objects. The reason why this is important is that, if a molecule has symmetry group Γ then that molecule is a representation of that abstract group Γ, which in turn means that Hamiltonian for the molecule has that same symmetry group. Then it is possible to gain information from the system using some other representation, which ideally identifies as an easier way to calculate group operations.

Every matrix group has an infinite amount of (matrix) representations, but all of these representations have same trace [47]. This makes trace, also called as *character*, a good way to characterize groups. Thus, tables of traces called *character tables* can be constructed, e.g., Table 2.1. Tables are constructed so that in the left-most column are the representations followed by the characters for each group operation. In the

Table 2.1: D_{6h} character table [49].

D_{6h}	E	$2C_6(z)$	$2C_3$	C_2	$3C_2'$	$3C_2''$	i	$2S_3$	$2S_6$	$\sigma_h(xy)$	$3\sigma_d$	$3\sigma_v$	
A_{1g}	+1	+1	+1	+1	+1	+1	+1	+1	+1	+1	+1	+1	x^2+y^2, z^2
A_{2g}	+1	+1	+1	+1	-1	-1	+1	+1	+1	+1	-1	-1	R_z
B_{1g}	+1	-1	+1	-1	+1	-1	+1	-1	+1	-1	+1	-1	
B_{2g}	+1	-1	+1	-1	-1	+1	+1	-1	+1	-1	-1	+1	
E_{1g}	+2	+1	-1	-2	0	0	+2	+1	-1	-2	0	0	R_x, R_y, xy, yz
E_{2g}	+2	-1	-1	+2	0	0	+2	-1	-1	+2	0	0	x^2-y^2, xy
A_{1u}	+1	+1	+1	+1	+1	+1	-1	-1	-1	-1	-1	-1	
A_{2u}	+1	+1	+1	+1	-1	-1	-1	-1	-1	-1	+1	+1	z
B_{1u}	+1	-1	+1	-1	+1	-1	-1	+1	-1	+1	-1	+1	
B_{2u}	+1	-1	+1	-1	-1	+1	-1	+1	-1	+1	+1	-1	
E_{1u}	+2	+1	-1	-2	0	0	-2	-1	+1	+2	0	0	x, y
E_{2u}	+2	-1	-1	+2	0	0	-2	+1	+1	-2	0	0	

far right are listed the representations of some common operators that have use in spectroscopy.

Great orthogonality theory (GOT) states [47, 48] that the different representations form an orthogonal vector space. This has a consequence that any function or mathematical object can be given a representation in any given group, so that it is a linear combination of representations of that group. An example is a group that only has one symmetry operation in addition to identity, the plane symmetry over y-axis. This group has two representations called even and odd. Thus, all functions can be expressed as a sum of even and odd functions. This is easy to prove, as polynomials with even powers are even functions and polynomials with odd powers are odd functions, meaning that any function that can be expressed as a polynomial is either even or odd or a sum of even and odd functions.

If an operator has a symmetry group Γ then all of its eigenstates belong to one of the group's representations, e.g., harmonic oscillator has only identity and symmetry plane and thus its eigenstates that are either even or odd.

The main use of GOT is to classify integrals to either zero or non zero. To see how this is done let us take a general group Γ and a constant function $f(x) = a \neq 0$. If this function is integrated over any area, the result is non zero. Function f(x) has a representation in group Γ. Because it is a constant function it does not change under any group operation and thus belongs to totally symmetric representation. GOT says that any other representation is orthogonal to this representation. Thus, if a function g(x) does not have totally symmetric representation then the integral

$$\int_\Gamma f(x)g(x)\mathrm{d}x = 0. \tag{2.1}$$

Any general integral can be written as a integral over constant function times the original function

$$\int_\Gamma h(x)\mathrm{d}x = \frac{1}{a}\int_\Gamma ah(x)\mathrm{d}x = \frac{1}{a}\int_\Gamma f(x)h(x)\mathrm{d}x, \tag{2.2}$$

meaning that, if the representation of integrand does not the include totally symmetric representation, the integral is zero.

2.3 LIE GROUPS AND ALGEBRAS

In case of continuous symmetry the groups became continuous as well. Among these continuous groups is a set of groups called *Lie groups*[3], named after Sophus Lie. These groups are very important because of their relationship with differential equations [44–46, 50, 51]. In short all differential equations have an associated Lie group (and Lie algebra). For example, algebraic solutions of differential equations are

*Short definition is that a **Lie group** is a continuous transformation of a continuous space to some other continuous space, where these continuous spaces can be functions, matrices, fields, operators, geometric shapes* etc..

3 Proper definition of Lie groups is a rather complicated matter and out of scope of this Thesis. For those interested Gilmore has a good introduction [45] (it takes him over 100 pages to define Lie groups!!!).

done using Lie algebra. Harmonic oscillator solution using creation and annihilation operators is a good example of this.

To demonstrate the use of Lie groups, lets take for example time symmetry [52], which states that laws of physics are independent of time. We now have an element of the Lie group $U(t_0, t_1)$ that will transform time from point t_0 to point t_1. Because we took independence of time as an axiom, we must have an additional property

$$U(t_0, t_0 + \Delta t) = U(t_1, t_1 + \Delta t) = U(\Delta t). \tag{2.3}$$

The identity element must be no translation at all

$$U(0) = \mathbb{1}. \tag{2.4}$$

Lie groups that have these additional properties are called ***connected Lie groups*** *[45].*

Group multiplication must be summation in time

$$U(\Delta t_1)U(\Delta t_2) = U(\Delta t_1 + \Delta t_2), \tag{2.5}$$

so the inverse element must satisfy

$$U(\text{-}\Delta t)U(\Delta t) = U(\Delta t)U(\text{-}\Delta t) = U(0) = \mathbb{1}. \tag{2.6}$$

We can use this group to operate, for example, to wave functions, which will result as a translation in time

$$U(\Delta t)\,|\Psi(0)\rangle = |\Psi(\Delta t)\rangle \tag{2.7}$$

To make sure that inner product stays same (we do not create or destroy particles), we must have

$$\langle\Psi(0)\,|\,\Psi(0)\rangle = \langle\Psi(t)\,|\,\Psi(t)\rangle \tag{2.8}$$

$$\langle\Psi(0)\,|\,\Psi(0)\rangle = \langle\Psi(0)U(t)\,|\,U(t)\Psi(0)\rangle \tag{2.9}$$

$$\mathbb{1} = U(t)^\dagger U(t) \tag{2.10}$$

that is we have

$$U(t)^\dagger = U(t)^{\text{-}1}, \tag{2.11}$$

Unitary groups are donated with symbol $U(N)$, where N is the dimension of the group.

which means that the group is *unitary*.

Because the group is continuous and connected it can be expanded as a Taylor series around an arbitrary point

$$U(\epsilon) = \mathbb{1} - i\epsilon H + \mathcal{O}(\epsilon^2), \tag{2.12}$$

There is some freedom in the sign of H here. In this case it is more convenient to use - than +, which will become evident in the following.

where H is Hermitian operator. We can note that this form satisfies all the requirements in first order of ϵ

$$\begin{aligned} U(\epsilon)U(\epsilon) &= \left(\mathbb{1} - i\epsilon H + \mathcal{O}(\epsilon^2)\right)\left(\mathbb{1} - i\epsilon H + \mathcal{O}(\epsilon^2)\right) \\ &= \mathbb{1} - i\epsilon H - i\epsilon H + \mathcal{O}(\epsilon^2) \\ &= U(\epsilon + \epsilon) \end{aligned} \tag{2.13}$$

$$U(\epsilon)^\dagger = \mathbb{1} + i\epsilon H + \mathcal{O}(\epsilon^2) = U(\text{-}\epsilon) \tag{2.14}$$

General time translation can be generated from this form with a multiplication

$$U(\Delta t) = \lim_{N\to\infty} U\left(\frac{\Delta t}{N}\right)^N = \lim_{N\to\infty}\left(\mathbb{1} + \frac{\text{-}i\Delta t H}{N}\right)^N \tag{2.15}$$

The last form of this equation can be recognized to be the definition of exponential function [53]

$$\exp(x) = \lim_{N\to\infty}\left(1 + \frac{x}{N}\right)^N. \tag{2.16}$$

Thus an arbitrary element of the group can be expressed as

$$U(\Delta t) = \exp(\text{-}iH\Delta t). \tag{2.17}$$

This is a *group form* or *exponential map* of Lie group, *differential form* can be generated by taking the derivative of the object being transformed with the group

$$\begin{aligned}\frac{\partial}{\partial t}|\Psi(t)\rangle &= \frac{\partial}{\partial t}U(t)\,|\Psi(0)\rangle \\ &= -iHU(t)\,|\Psi(0)\rangle\end{aligned}$$

$$i\frac{\partial}{\partial t}|\Psi(t)\rangle = H\,|\Psi(t)\rangle\,. \tag{2.18}$$

Operator H is said to be *generator of the group*, or in this case generator of time translations, which is usually named as Hamiltonian operator. It has unit of one over unit of time ($1/\mathrm{s}$ if using SI-units), but for general convenience it is good to introduce an unit conversion factor, here marked as $\hbar$. With it the group takes a form

$$U(\Delta t) = \exp(\text{-}iH\Delta t/\hbar) \tag{2.19}$$

$$i\hbar\frac{\partial}{\partial t}|\Psi(t)\rangle = H\,|\Psi(t)\rangle\,, \tag{2.20}$$

which can be recognized as *general Schrödinger equation*.

It should be noted that we do not have any information about the form of Hamiltonian operator yet, other than it is Hermitian.

2.3.1 *Lie groups with multiple generators*

The time translation group has only one generator, but in general Lie groups can have multiple generators. Group multiplication in this case is (**using Einsteins summation rule**) [46]

$$\exp(i\alpha_a X_a)\exp(i\beta_b X_b) = \exp(i\delta_c X_c), \tag{2.21}$$

because the group is closed. If the group is Abelian then $\delta_a = \alpha_a + \beta_a$ and everything is simple, but if the group is not Abelian the situation is more complicated.

In this case a logarithm can be taken of both sides of equation (2.21)

$$\begin{aligned}i\delta_c X_c &= \ln\left(\exp(i\alpha_a X_a)\exp(i\beta_b X_b)\right) \\ &= \ln\left(1 + \exp(i\alpha_a X_a)\exp(i\beta_b X_b) - 1\right).\end{aligned} \tag{2.22}$$

Then by expression $\ln(1+x) = x - \frac{1}{2}x^2 + \ldots$ on the right hand side, with first expanding the internal part as

$$\begin{aligned} x =& \exp(i\alpha_a X_a)\exp(i\beta_b X_b) - 1 \\ =& (1 + i\alpha_a X_a - \frac{1}{2}(\alpha_a X_a)^2 + \ldots) \\ & * (1 + i\beta_b X_b - \frac{1}{2}(\beta_b X_b)^2 + \ldots) - 1 \\ =& + i\alpha_a X_a + i\beta_b X_b - \alpha_a X_a \beta_b X_b \\ & - \frac{1}{2}(\alpha_a X_a)^2 - \frac{1}{2}(\beta_b X_b)^2 + \ldots \end{aligned} \tag{2.23}$$

and use it to expand the logarithm in first two orders

$$\begin{aligned} i\delta_c X_c =& \ln(1+x) \\ =& x - \frac{1}{2}x^2 + \ldots \\ =& i\alpha_a X_a + i\beta_b X_b - \alpha_a X_a \beta_b X_b \\ & - \frac{1}{2}(\alpha_a X_a)^2 - \frac{1}{2}(\beta_b X_b)^2 \\ & + \frac{1}{2}(\alpha_a X_a + \beta_b X_a)^2 + \ldots \end{aligned}$$

Simplifying this equation leads to

$$i\delta_c X_c = i\alpha_a X_a + i\beta_b X_b - \frac{1}{2}[\alpha_a X_a, \beta_b X_b] + \ldots \tag{2.24}$$

From which an expression for commutator can be taken

$$[\alpha_a X_a, \beta_b X_b] = -2i(\delta_c - \alpha_c - \beta_c)X_c + \ldots \equiv i\gamma_c X_c. \tag{2.25}$$

This equation must hold for every α and β, so it must be that

$$\gamma_c = \alpha_a \beta_b f_{abc} \tag{2.26}$$

and thus a *Lie algebra* must hold

$$[X_a, X_b] = i f_{abc} X_c, \tag{2.27}$$

where for f must also have antisymmetry rule

$$f_{abc} = -f_{bac}, \tag{2.28}$$

because $[A, B] = -[B, A]$.

With this relationship it is possible to generate all the elements of a Lie group. Also notable here is that because the generators form an algebra, the generators then form an orthogonal vector space.

In general Baker-Campbell-Hausdorff formula is used to generate new Lie group elements. Because Lie groups are infinitesimal we only need to take the first extra term in the formula into account.

Also, several different Lie groups can have same algebra, like 2-dimensional special unitary group (SU(2)) and 3-dimensional special orthogonal group (SO(3)). However, only one of the groups that have same algebra has a property called *simply connected*, which means that any loop on the group can be continuously transformed to any point on the group. This group is then called as *universal covering group* for

that algebra [45]. In an example SU(2) is the universal covering group for algebra

$$[J_n, J_m] = iJ_k \qquad n, m, k = 1, 2, 3. \tag{2.29}$$

In practice this means that certain 2-dimensional object that have SU(2) can be understood as 3-dimensional rotations. One example is 2-dimensional harmonic oscillator that can be understood as a rotating object.

2.4 UNITARY GROUP

The importance of unitary group is based largely on Schrödinger equation, which is a differential form of time symmetry group. This means that a system of N degrees of freedom is represented with a *N-dimensional unitary group* (U(N)).

If system has some form of symmetry, such as a point group, then the Hamiltonian of this system has also this symmetry. This means that the Hamiltonian belongs to totally symmetric representation of the group. Eigenstates on the other hand can belong to any of the representations. This means that, if the degrees of freedom of the system belong to different representations, the Hamiltonian is in block form, because there are no totally symmetric elements that would couple these representations. As an example, if states are represented in A_1, A_2 and E representations, the Hamiltonian would be in the form

$$H = U(4) = U(1) \otimes U(1) \otimes U(2) = H_{A_1} + H_{A_2} + H_E. \tag{2.30}$$

Unitary group is defined to be formed of all complex valued matrices that are unitary

$$UU^\dagger = U^\dagger U = \mathbb{1}. \tag{2.31}$$

Determinant of these matrices is either +1 or -1. This means that unitary group has a subgroup that includes all the matrices that have +1 determinant. This subgroup is called as *special unitary group* (SU) [45].

Unitary group has a property

$$U(N) = U(1)SU(N), \tag{2.32}$$

which can be expressed also as

$$U(N) = e^{i\alpha}SU(N), \tag{2.33}$$

with α being a hermitian N-dimensional operator.

To demonstrate these properties, let us consider 3-dimensional harmonic oscillator [45, 46, 54], which has following Hamiltonian

$$H = \hbar\omega(a_1^\dagger a_1 + a_2^\dagger a_2 + a_3^\dagger a_3 + \frac{3}{2}). \tag{2.34}$$

$U(3)$ group is defined by 9 generators of form

$$U_{ij} = a_i^\dagger a_j, \tag{2.35}$$

with following algebra

$$[U_{ij}, U_{sr}] = U_{is}\delta_{jr} - U_{rj}\delta_{si}. \tag{2.36}$$

Note that this form is actually $SO(3)$ group representation of $U(3)$ generators. $\mathscr{H}$ is scalar, L_k are vectors and T_{ij} are second rank tensors.

By defining following operators

$$\mathscr{H} = a_0^\dagger a_0 = a_1^\dagger a_1 + a_2^\dagger a_2 + a_3^\dagger a_3 \tag{2.37}$$

$$L_k = a_i^\dagger a_j - a_j^\dagger a_i \tag{2.38}$$

$$T_{ij} = a_i^\dagger a_j + a_j^\dagger a_i - \frac{2}{3}\mathscr{H}\delta_{ij} \tag{2.39}$$

these generators can be transformed to a more familiar form. $\mathscr{H}$ is the generator of a $U(1)$ group and defines energy. Other generators define degeneracy by forming a $SU(3)$ group. L_k generators also form a $SO(3)$ subgroup that defines angular momentum.

2.4.1 *Special Orthogonal Group and Rotations*

Unitary group, that is defined over complex numbers, has a subgroup that is defined on real numbers, which is related to rotations. A rotation is defined as a real linear transformation that leaves the scalar product between two vectors invariant [52]

$$\langle V|U\rangle = \langle V|R^T R|U\rangle\,, \tag{2.40}$$

which means

$$R^T R = \mathbb{1}. \tag{2.41}$$

So that the determinant of R is ± 1. A Lie group of this kind is called as *orthogonal group* and abbreviated as $O(N)$. It has a subgroup with determinants $+1$, which is called as *special orthogonal group* $SO(N)$. The difference between these two is that SO-group does not include space inversions and is thus continuous, while O-group also includes inversions.

For infinitesimal rotations ω, rotation matrix is

$$R = \mathbb{1} + \omega + \mathcal{O}(\omega^2). \tag{2.42}$$

Adding this to 2.41 leads to

$$\begin{aligned}\mathbb{1} &= \left(\mathbb{1} + \omega^T + \mathcal{O}(\omega^2)\right)\left(\mathbb{1} + \omega + \mathcal{O}(\omega^2)\right) \\ &= \mathbb{1} + \omega^T + \omega + \mathcal{O}(\omega^2),\end{aligned} \tag{2.43}$$

so that

$$\omega^T + \omega = 0$$

$$\omega^T = -\omega \tag{2.44}$$

$$\omega_{ji} = -\omega_{ij}. \tag{2.45}$$

This is a definition of an *antisymmetric matrix* [55].

By using a notation $\boldsymbol{\omega} = \omega_{ij} J_{ij}$, where J_{ij} is an operator and ω_{ij} is a rotation angle, we can express $SO(N)$ algebra in conventional form [52]

$$\frac{1}{\hbar}\left[J_{ij}, J_{kl}\right] = -\delta_{il} J_{kl} + \delta_{ik} J_{lj} + \delta_{jk} J_{il} - \delta_{jl} J_{ik}. \tag{2.46}$$

Also, for a general vector $\boldsymbol{V}$ there is a commutation rule [52]

$$\frac{1}{\hbar}\left[V_k, J_{ij}\right] = \delta_{ik} V_j - \delta_{jk} V_i. \tag{2.47}$$

It should be noted that if $\boldsymbol{A}$ is an antisymmetric matrix then $i\boldsymbol{A}$ is Hermitian [45]

$$(i\boldsymbol{A})^\dagger = \text{-}i\boldsymbol{A}^T = i\boldsymbol{A}. \tag{2.48}$$

Exponential map can then be used to create an associated Lie group element

$$i\boldsymbol{A} \rightarrow e^{i(i\boldsymbol{A})} = e^{\text{-}\boldsymbol{A}}. \tag{2.49}$$

This way it is possible to create all the possible elements of $SO(N)$ group, using a linear combination of complete orthogonal basis of antisymmetric matrices $\boldsymbol{A}_n$, total of $\frac{1}{2}N(N-1)$ basis matrices. A general element of $SO(N)$ group then has an exponential map

$$\exp(\text{-}\sum_n \omega_n \boldsymbol{A}_n). \tag{2.50}$$

This means that, if $\hat{u}$ is an unit vector, then any unit vector in that space can be expressed as

$$\exp(\text{-}\sum_n \omega_n \boldsymbol{A}_n)\hat{u}. \tag{2.51}$$

2.5 SO(3) TENSOR OPERATORS AND WIGNER-ECKART THEOREM

Commutator algebra allows assigning angular momentum to operators [46, 52]. This is done according to commutation rules

$$[J_z, O_j^m] = \hbar m O_j^m \tag{2.52}$$

$$[J_x \pm iJ_y, O_j^m] = \hbar\sqrt{j(j+1) - m^2 \mp m}\, O_j^{m\pm 1}, \tag{2.53}$$

or alternatively as

$$[\boldsymbol{J}, O_j^m] = \hbar \sum_{m'} \langle j, m' | \boldsymbol{J} | j, m \rangle\, O_j^{m'}. \tag{2.54}$$

This means that an operator O_j^m is considered of having same the transformation rules under SO(3) (or SU(2)) rotation as rotation state $|j, m\rangle$.

As an example for a vector [52]

$$V_1^1 = \frac{V_x + iV_y}{\sqrt{2}} \qquad V_1^{\text{-}1} = \frac{V_x - iV_y}{\sqrt{2}} \qquad V_1^0 = V_z. \tag{2.55}$$

An alternative way of seeing this is to note that

$$x = r\cos\phi\sin\theta = \sqrt{\frac{8\pi}{3}}r(Y_1^1 + Y_1^{-1}) \tag{2.56}$$

$$y = r\sin\phi\sin\theta = i\sqrt{\frac{8\pi}{3}}r(Y_1^1 - Y_1^{-1}) \tag{2.57}$$

$$z = r\cos\theta = \sqrt{\frac{4\pi}{3}}rY_1^0, \tag{2.58}$$

where Y_j^m are the spherical harmonics, so

$$rY_1^1 = \sqrt{\frac{3}{8\pi}}(x + iy) \tag{2.59}$$

$$rY_1^{-1} = \sqrt{\frac{3}{8\pi}}(x - iy) \tag{2.60}$$

$$rY_1^0 = \sqrt{\frac{3}{4\pi}}z. \tag{2.61}$$

In a case of operator being a tensor product of two tensors, the following commutation rule is useful in forming representations [46]

$$[J_a, O_{j_1}^{m_1}O_{j_2}^{m_2}] = [J_a, O_{j_1}^{m_1}]O_{j_2}^{m_2} + O_{j_1}^{m_1}[J_a, O_{j_2}^{m_2}]. \tag{2.62}$$

Alternatively addition of angular momentum can be used.

For example, symmetric second-rank tensor $\boldsymbol{T} = \boldsymbol{V} \otimes \boldsymbol{V}$ has representations for $J = 0, 2$ (because $J = 1$ is antisymmetric). To get these representations a simple use of Clebsch-Gordan coefficients [52] is all that is needed

$$T_2^2 = V_1^1V_1^1 = \frac{1}{2}\left(T_{xx} - T_{yy}\right) + iT_{xy} \tag{2.63}$$

$$T_2^1 = \sqrt{\frac{1}{2}}\left(V_1^1V_1^0 + V_1^0V_1^1\right) = \frac{1}{2}\left(T_{xz} + iT_{yz}\right) \tag{2.64}$$

$$T_2^0 = \sqrt{\frac{1}{6}}\left(V_1^1V_1^{-1} + V_1^{-1}V_1^1\right) - \sqrt{\frac{2}{3}}V_1^0V_1^0 = \frac{T_{xx} + T_{yy}}{\sqrt{6}} - \sqrt{\frac{2}{3}}T_{zz} \tag{2.65}$$

$$T_2^{-1} = \sqrt{\frac{1}{2}}\left(V_1^{-1}V_1^0 + V_1^0V_1^{-1}\right) = \frac{1}{2}\left(T_{xz} - iT_{yz}\right) \tag{2.66}$$

$$T_2^{-2} = V_1^{-1}V_1^{-1} = \frac{1}{2}\left(T_{xx} - T_{yy}\right) - iT_{xy} \tag{2.67}$$

$$T_0^0 = \sqrt{\frac{1}{3}}\left(V_1^1V_1^{-1} + V_1^0V_1^0 + V_1^{-1}V_1^1\right) = \frac{T_{xx} + T_{yy} + T_{zz}}{\sqrt{3}}. \tag{2.68}$$

The reason why representing tensors in SO(3) is usable relies on the fact that they can then be separated to magnitude and orientation components, with the *Wigner-Eckart theorem* [46, 52]. The theorem states that a matrix element of operator O_j^m can be calculated as follows

$$\langle r', J', M'|O_j^m|r, J, M\rangle = C_{jJ}(J'M'; mM)\,\langle r'||O||r\rangle\,, \tag{2.69}$$

where $C_{jJ}(J'M'; mM)$ is *Clebsch-Gordan coefficient* [46, 52]

$$C_{jJ}(J'M'; mM) = \langle J'M'; jJ|j, m; J, M\rangle \tag{2.70}$$

and $\langle r'||O||r\rangle$ reduced matrix element that is independend of quantum numbers M', M and m.

2.6 SPECIAL RELATIVITY AND POINCARÉ GROUP

Special relativity is a symmetry that states that the speed of light is same for all observers. This is a Lie group, which is usually called with name *Poincaré group*. Lie algebra for this group can be generated by requiring Minkowski distance ($c^2t^2 - r^2$) to be constant for all inertial frames of reference [42]. This leads to following Lie algebra ($\hbar = 1$, $c = 1$)

It should be noted that special relativity includes time, space and rotation symmetries as its subgroups.

$$[J_i, J_j] = i\epsilon_{ijk}J_k \tag{2.71}$$
$$[J_i, K_j] = i\epsilon_{ijk}K_k \tag{2.72}$$
$$[K_i, K_j] = -i\epsilon_{ijk}J_k \tag{2.73}$$
$$[J_i, p_j] = i\epsilon_{ijk}p_k \tag{2.74}$$
$$[K_i, p_j] = iH\delta_{ij} \tag{2.75}$$
$$[J_i, H] = [p_i, H] = [H, H] = 0 \tag{2.76}$$
$$[K_i, H] = -ip_i, \tag{2.77}$$

where

$H = p_0$ zero coordinate of momentum, also called *Hamiltonian*

p_i space translation generator, or *momentum*

J_i space rotation generator, or *angular momentum*

K_i *Lorentz boost* - operator that changes momentum

ϵ_{ijk} *Levi-Civita symbol* - totally antisymmetric tensor

Additionally there are also *space inversion* (P) and *time-reversal* (T) symmetries:

$$\mathrm{P}\boldsymbol{J}\mathrm{P}^{-1} = +\boldsymbol{J} \tag{2.78}$$
$$\mathrm{P}\boldsymbol{K}\mathrm{P}^{-1} = -\boldsymbol{K} \tag{2.79}$$
$$\mathrm{P}\boldsymbol{p}\mathrm{P}^{-1} = -\boldsymbol{p} \tag{2.80}$$
$$\mathrm{T}\boldsymbol{J}\mathrm{T}^{-1} = -\boldsymbol{J} \tag{2.81}$$
$$\mathrm{T}\boldsymbol{K}\mathrm{T}^{-1} = +\boldsymbol{K} \tag{2.82}$$
$$\mathrm{T}\boldsymbol{p}\mathrm{T}^{-1} = -\boldsymbol{p} \tag{2.83}$$
$$\mathrm{P}H\mathrm{P}^{-1} = \mathrm{T}H\mathrm{T}^{-1} = H. \tag{2.84}$$

The reason why these are important is that all physics excluding gravity obeys special relativity, and thus also all chemistry. **Most importantly, the total system Hamiltonian must satisfy these commutation rules!**

To demonstrate this, let us take as an example free-particle Hamiltonian. According to commutation rules, Hamiltonian commutes with momentum, as shown in Equation 2.76. Thus, the most general form of Hamiltonian is that of a sum of a term that commutes with momentum and some general function of momentum that can be expanded in a Taylor series

$$H = A + f(\boldsymbol{p}) = A + a_0 + a_1\boldsymbol{p} + a_2\boldsymbol{p}^2 + \dots. \tag{2.85}$$

Because the Hamiltonian does not change sign under space inversions, all odd terms in this sum must be zero. Secondly, we can change the zero-energy level, so that the constant term vanishes. Thus, we are left with

$$H = a_2 \boldsymbol{p}^2 + a_4 \boldsymbol{p}^4 + \dots . \tag{2.86}$$

We can make a low-velocity approximation, by dropping higher momentum powers, to get

$$H = a_2 \boldsymbol{p}^2. \tag{2.87}$$

At this point we can change a_2-term to different form

$$H = \frac{\boldsymbol{p}^2}{2m} \tag{2.88}$$

and call the variable m with name *mass*.

Because laws of physics are independent of location (included in special relativity), we have a space symmetry. For this we can generate a Lie group the same way we did earlier for time symmetry. Therefore, we can generate a differential form for momentum operator the same way we did it for Hamiltonian earlier. By choosing the sign so that the Minkowski metric is obeyed, that is a different sign for time and space symmetries, we get

$$p_i = \text{-}i\hbar \frac{\partial}{\partial x_i}, \tag{2.89}$$

so the Hamiltonian is then

$$H = \text{-}\frac{\hbar^2}{2m} \nabla^2 \tag{2.90}$$

and the free-particle Schrödinger equation is

$$i\hbar \frac{\partial}{\partial t} \left| \Psi(t, \boldsymbol{r}) \right\rangle = \text{-}\frac{\hbar^2}{2m} \nabla^2 \left| \Psi(t, \boldsymbol{r}) \right\rangle . \tag{2.91}$$

In a case of multiple non-interacting particles Hamiltonian is just a sum individual particle Hamiltonians. In the interacting case there is an additional interaction therm V called *potential energy*. Thus, for the interacting case the Hamiltonian is

Form of potential energy is so that it obeys the symmetries of the standard model $U(1) \otimes SU(2) \otimes SU(3)$ and that it fulfills the Poincaré group commutation relations.

$$H = \text{-}\sum \frac{\hbar^2}{2m} \nabla^2 + V. \tag{2.92}$$

This is actually a formal derivation of *Schrödinger equation* that is also called as non-relativistic wave equation for spinless (scalar) particles.[4]

Mathematically, Schrödinger equation is used to find a representation of Poincaré's group, and then the Poincaré group element is

4 It should be noted that there are several wave equations, and that there is a systematic way of deriving them. Most notably, relativistic wave equation for spin-half particles is called as the Dirac equation and relativistic equation for spinless particles is called as the Klein-Gordon equation. To see how these equations can be derived see Weinberg [42].

used to translate the system in some useful way (usually in time). The standard way of finding this representation is done by writing a Schrödinger equation in position basis and manipulating it to an easier-to-use representation that ideally could be diagonalized.

However, there is an alternative way. Because all that is needed is a representation of Poincaré's group, it would be perfectly valid to just generate a representation in some other way and then using the group elements of that representation to translate the system in some meaningful way. In the case of time translations, it is possible to just generate a new representation to Hamiltonian in the same way that was shown here, and thus avoid the use of the position basis completely. The point of doing this is that sometimes this way is easier than taking the traditional way of starting from the position representation.

3

ELECTRONIC STRUCTURE

The most general wave function for a molecule has a form

$$|\Psi\rangle = \sum_{n,e} a_{n,e} |\psi_n\rangle |\psi_e\rangle , \tag{3.1}$$

where $|\psi_n\rangle$ and $|\psi_e\rangle$ are nuclear and electronic basis functions. Because nucleons are several orders of magnitude more massive than electrons the coupling between them is weak. Based on this an approximate form of wave function can be formed, by explicitly decoupling electronic and nuclear motions as

$$|\Psi\rangle \approx \left(\sum_n a_n |\psi_n\rangle \right) \left(\sum_e b_e |\psi_e\rangle \right) = |\Psi_n\rangle |\Psi_e\rangle , \tag{3.2}$$

which is called as *Born-Oppenheimer approximation*.

Also, in practical calculations the nucleons are considered to be stationary, so that they can be added parametrically, as stationary point charge parameters to electronic structure calculations, while their kinetic energy can be ignored.

There are two main ways of doing electronic structure calculations: wave function methods and density functional theory (DFT) methods. The aim of wave function methods is to find electronic wave function(s), eigenstate(s) of electronic Hamiltonian, and the aim of DFT is to calculate the electron density.

3.1 WAVE FUNCTION METHODS

All wave function methods work the following way:

1. Generate initial wave function – vector in Hilbert space.
2. Use SO-group element to rotate initial wave function to an eigenvector of the system Hamiltonian.

Methods differ from each other, by how or what kind of initial state is generated and by what kind of (approximative) form they use for the SO-group element.

For an example, an initial electronic state can be taken to be a single *Slater determinant*

$$\Phi = \frac{1}{\sqrt{N!}} \begin{vmatrix} \phi_1(1) & \phi_2(1) & \cdots & \phi_N(1) \\ \phi_1(2) & \phi_2(2) & \cdots & \phi_N(2) \\ \vdots & \vdots & \ddots & \vdots \\ \phi_1(N) & \phi_2(N) & \cdots & \phi_N(N) \end{vmatrix} , \tag{3.3}$$

where ϕ are called as *orbitals* and that are populated with two electrons in spin-zero configuration called as *closed-shell wave function* [56–58].

The true state can then be represented as a linear combination of several different Slater determinants

$$\Psi = \sum_i a_i \Phi_i.$$

The mathematical difference between orbital space and Hilbert space is that orbitals form a vector space and the system Hilbert space is a product space of N fermion orbital space.

3.1.1 *Hartree-Fock*

Hartree-Fock (HF) is a method used to generate initial state for more accurate methods. The aim is to find a Slater determinant that is the closest to the true electronic state. Mathematically this is the Slater determinant that has the largest overlap with the true state. In practice, calculating overlap with the true state cannot be done unless true state is known, which defeats the purpose of finding a good initial state. Hartree-Fock thus tries to find the second best thing, i.e., the Slater determinant that has the lowest energy, which is called as HF ground state Φ_{HF}. Mathematically this is equivalent to rotating orbital space, so that in Hilbert Space a single Slater determinant is in the global energy minimum respect to orbital space rotations.

The HF ground state is calculated with the help of *Fock matrix* [56–58], which for closed shell representation is

$$F = h_1 + \sum_i (2J_i + K_i), \tag{3.4}$$

where $\sum_i$ is over all occupied orbitals, h_1 is one-electron Hamiltonian, J_i the Coulomb operator

$$J_i(r_1) = \int \mathrm{d}\boldsymbol{r}_2 \psi_i^*(r_2)\psi_i(r_2)\frac{1}{|r_1 - r_2|} \tag{3.5}$$

and K_i the exchange operator

$$K_i(r_1)\psi_a(r_1) = \left(\int \mathrm{d}\boldsymbol{r}_2 \psi_i^*(r_2)\psi_a(r_2)\frac{1}{|r_1 - r_2|}\right)\psi_i(r_1). \tag{3.6}$$

Orbitals are eigenvectors of the Fock matrix and they need to be solved iteratively, because Coulomb and Exchange operators depend on them. Slater determinant is then constructed from the calculated orbitals with the lowest eigenvalues.

3.1.2 *Post Hartree-Fock methods*

Post-HF methods take the HF state as an initial state and rotate it to get a more accurate state. The most general form of the SO-group element (rotation matrix) is

$$\exp(-\sum_n \omega_n \boldsymbol{A}_n), \tag{3.7}$$

where A_n are antisymmetric matrices, as was discussed in subsection 2.4.1. The base vectors in the Hilbert space are formed from a complete set of Slater determinants. Thus, an orthogonal set of antisymmetric operators has the form

$$A_{ij} = |\Phi_i\rangle \langle\Phi_j| - |\Phi_j\rangle \langle\Phi_i| . \tag{3.8}$$

Because Slater determinants consist of orbitals, and different determinants differ from each other by a number of orbitals, the operators A_{ij} can be categorized based on how many orbitals they change. Thus, if a operator A only changes one orbital, it is called as a single excitation ($\hat{S}$), if it changes two orbitals it is called as a double excitation ($\hat{D}$) and so on. Thus, a general SO-group element can be written as

$$\exp(\sum_n s_n \hat{S}_n + \sum_n d_n \hat{D}_n + \sum_n t_n \hat{T}_n + \ldots) \tag{3.9}$$

and the ground state of the system can be found by finding constants $s_n, d_n, \ldots$ that minimize the energy of a wave function of the form

$$\Psi_{CC} = \exp(\sum_n s_n \hat{S}_n + \sum_n d_n \hat{D}_n + \sum_n t_n \hat{T}_n + \ldots)\Phi_{HF}. \tag{3.10}$$

This kind of method is called as *couple cluster* (CC) [57, 58].

In practical calculations the number of excitations has to be limited. Thus, a method including only single and double excitations is called as *coupled cluster singlets and doublets* (CCSD), if triple excitations are also included abbreviation CCSDT is used and so on. This truncation of excitations means that the state vector is rotated in fewer number of dimensions and, thus, the resulting state differs from the true state. This difference can be expected to be smaller the more excitations are included.

Also, in numerical calculations, the exponential function needs to be calculated by using a Taylor series, which in turn needs to be truncated. From the theory of the Taylor series [53], it is known that truncating limits the accuracy of the function far away from the point around which the series was developed. This means that the angle of rotation needs to be small for couple cluster approach to be accurate, which on the other hand means that the final state needs to be close to the initial state. Moreover, the final state needs to have large contribution from the initial state, for CC to work. In case a single Slater determinant is used as an initial state, the resulting final state has a large contribution from that Slater determinant. This kind of methods are called as *single-reference methods*, opposed to methods that have initial state as a linear combination of different Slater determinants that are called as *multi-reference methods* [58].

A special mention should be given to a method named *coupled cluster single, double and perturbative triple* (CCSD(T)), in which triple excitations are added with perturbation theory [58]. The reasoning here is that perturbation theory tends to give too low energies while CCSDT gives too high and thus using perturbation theory for triple excitations has error cancellation between the two. Perturbation theory is also significantly lower in computational cost than computing true

triple excitations computationally. Thus, it usually gives better results in less time than CCSDT. CCSD(T) is commonly titled as "the golden standard of quantum chemistry", because of its accuracy.

There is an alternative form for the exponential representation of SO-group element (3.9)

$$\exp(\sum_n s_n \hat{S}_n + \sum_n d_n \hat{D}_n + \ldots) = a\mathbb{1} + \sum_n \tilde{s}_n \hat{S}_n + \sum_n \tilde{d}_n \hat{D}_n + \ldots \quad (3.11)$$

With this form wave function can be expressed as

$$\Psi_{CI} = \left(a\mathbb{1} + \sum_n \tilde{s}_n \hat{S}_n + \sum_n \tilde{d}_n \hat{D}_n + \ldots \right) \Phi_{HF} \quad (3.12)$$

and the associated method is called as *configuration interaction* (CI) [57, 58].

Same kind of naming scheme exists as for CC, where CISD denotes configuration interaction single and double, CISDT singlets, doublets and triples and so on. When all the excitations are included the method is called as *full configuration interaction* (FCI).

3.2 DENSITY FUNCTIONAL THEORY

In *density functional theory* (DFT) the aim is to find electron density for the electronic ground state. This is based on a theorem by Hohenberg and Kohn [59] that states that there is one-to-one correspondence between the electronic ground-state wave function and the associated density

$$\rho(r) = N \int \ldots \int |\Psi(\boldsymbol{r}_1, \boldsymbol{r}_2, \ldots, \boldsymbol{r}_N)|^2 \mathrm{d}\boldsymbol{r}_2 \ldots \mathrm{d}\boldsymbol{r}_N, \quad (3.13)$$

and because the ground state is also unique for a Hamiltonian, the ground-state density is also unique for the Hamiltonian.

This means that there exists a functional of electron density that gives the energy of the system

$$E = E[\rho]. \quad (3.14)$$

The Hohenberg-Kohn theorem itself does not say anything of the form of this functional other than it must exist, which meant that the true form was up to a guess.

To solve this problem, a new theory by Kohn and Sham followed soon [60]. The Kohn-Sham theory (KS) reintroduced orbitals back to DFT, which allowed the majority of kinetic energy to be calculated as (using atomic units)

$$T_{KS}[\rho] = \sum_i n_i \langle \phi_i | -\frac{1}{2} \nabla^2 | \phi_i \rangle \,, \quad (3.15)$$

with n_i being the occupation number of orbital ϕ_i. A side effect of orbitals is that electron exchange needs to taken into account. This leads to an energy functional of the following form [57]

$$E[\rho] = T_{KS}[\rho] + E_{ne}[\rho] + J[\rho] + E_{xe}[\rho], \quad (3.16)$$

where *nuclear-electron potential energy functional* is

$$E_{ne}[\rho] = -\sum_n \int \frac{Z_n(\boldsymbol{R}_n)\rho(\boldsymbol{r})}{|\boldsymbol{R}_n - \boldsymbol{r}|} \mathrm{d}\boldsymbol{r} \tag{3.17}$$

and *electron repulsion functional*

$$J[\rho] = \frac{1}{2} \int \int \frac{\rho(\boldsymbol{r}_1)\rho(\boldsymbol{r}_2)}{|\boldsymbol{r}_r - \boldsymbol{r}_2|} \mathrm{d}\boldsymbol{r}_1 \mathrm{d}\boldsymbol{r}_2. \tag{3.18}$$

For practical calculation this leads to the Kohn-Sham equations [61, 62]

$$\left[-\frac{1}{2}\nabla^2 + v_{nuc}(r) + v_{Coulomb}[\rho](r) + v_{xc}[\rho](r)\right] \phi_i(r) = \varepsilon_i \psi_i(r), \tag{3.19}$$

where functional derivatives v_{nuc}, $v_{Coulomb}$ and v_{xc} are defined by differentiating the corresponding energy term relative to electron density

$$v_{nuc}[\rho](r) = \frac{\delta E_{ne}[\rho]}{\delta \rho(r)} \tag{3.20}$$

$$v_{Coulomb}[\rho](r) = \frac{\delta J[\rho]}{\delta \rho(r)} \tag{3.21}$$

$$v_{xc}[\rho](r) = \frac{\delta E_{xc}[\rho]}{\delta \rho(r)} \tag{3.22}$$

and the electron density is defined as

$$\rho(\boldsymbol{r}) = \sum_i n_i |\phi_i|^2. \tag{3.23}$$

Orbitals are then calculated as eigenvectors of the operator in the square brackets in Equation 3.19, called as Kohn-Sham Hamiltonian, in a similar way as orbitals are calculated form Fock matrix in HF calculation.

One way to describe difference between DFT and wave function methods is that in DFT correlation is included in the functional and the density is simple, while with wave function methods, the wave function includes correlation and the Hamiltonian is simple.

Various different functionals have been developed [63], and many electronic structure books also include a section for different functionals [57, 64].

In general, an exchange-correlational functional needs to take into account the whole topology of the electron density, but in practice this is not done. The simplest functionals only take into account point density and are categorized as *local density approximation* (LDA) or *local spin density approximation* (LSDA), meaning that they are fast and mostly inaccurate. The next class of functionals additionally take into account the gradient of electron density and they are called as *generalized gradient approximation* (GGA).[1] Functionals that also include

1 MD simulations in this Thesis where mainly done with the BLYP functional [65], which is a combination of B88 [66] and LYP functionals [67], both of which are GGA functionals. The only other functional used was M06l [68] in high excitation simulations, which is a meta-GGA.

higher-order gradients are called as meta-GGA functionals. The next level of functionals, called *hybrid functionals*, add exchange in the form of Hartree-Fock exchange, by adding the exchange integrals

$$\int \phi_1(r_2)\phi_2(r_1)\frac{1}{|r_1 - r_2|}\phi_2(r_2)\phi_1(r_2)\mathrm{d}r_1\mathrm{d}r_2, \tag{3.24}$$

which has a consequence of severe computational cost increase. After this there are *double-hybrid functionals* that add virtual orbitals to model correlation with perturbation theory.

Finally, special functionals are needed to take into account dispersion. This is usually done using functionals developed by the Grimme group, mainly D2 [69], D3 [70], D3(BJ) [71] and D4 [72]. From these functionals it is recommended to use the latest available functional. The differences between them is that D2 is empirical, does not take environment into account and goes to minus infinity when atoms approach each other. D3 takes environment into account and goes to zero when atoms approach each other. D3(BJ) adds damping to D3, so that it goes to some fixed, non-zero value when atoms approach each other. Finally D4 is an improvement over all the previous functionals, but it has limited availability in programs at this moment, due to it being a relatively new one.

3.3 BASIS SETS

There are many different kinds of available basis sets, but in general most of the calculations are done either with gaussian type orbital (GTO) [58] or plane-wave (PW) [73] basis sets. The main difference between the two is that GTOs are better suited for isolated systems, while PWs are suited for continuous systems.

In real use cases the basis sets employed are subsets of complete basis sets, due to limitations imposed by numerical calculation. This means that a large number of different basis sets exist, with different accuracies and cases in which they are used. From it follows that in real calculations knowledge of these limitations is necessary for proper calculations and interpretation of the results.

3.3.1 *Gaussian Basis*

Gaussian-type orbitals are used to mimic real atomic orbitals (AOs). Their use is based on the property that the product of two gaussians functions is a single Gaussian function, which results in large savings in computational time.

In the calculations molecular orbitals are built from linear combination of atomic orbitals (LCAO). In the simplest basis sets each electron has only a single orbital, which is called as *the minimal basis set*. In a more realistic calculation more basis functions are added to increase accuracy. To categorize these larger basis sets terms double-zeta, triple-zeta and so on, are used. These terms mean that there are two orbitals per electron (double-zeta), three orbitals per electron (triple-zeta) [57, 58] and so on.

In addition to these basis sets also include the polarization functions, which are used to describe the polarization of atomic charge and are essential to describe dipole-dipole and hydrogen bonding, and diffusion functions that are needed to describe long-range electronic interactions such as anions and dispersion [58].

3.3.2 *Plane-Wave Basis*

Plane waves are a natural way to describe continuous systems due to translational symmetry and therefore, they are used in many molecular dynamics programs. Usage of PWs requires defining a simulation box, which is then repeated. PWs are then defined in the box by using a plane-wave cutoff that defines the maximum-energy PW. The cutoff is usually stated in Rydberg units.

The major advantage of PWs is that they use the fast Fourier transform, which is more efficient in integral calculations than the Gaussian basis set algorithms.

A major disadvantage of PWs is that representing high electron density needs a very large number of PWs, which, in turn, causes major increase in computational time. Because high density is caused by core electrons, a way to solve this problem is to represent the core electrons in some other way. This is usually done with either pseudopotentials or the projector augmented-wave approach[64, 73].

If PWs are used for an isolated molecule, the periodic images that are part of periodic PWs need to be decoupled in addition of changing to non-periodic boundary conditions. This is done with a Poisson-equation solver [74–77]. In general, the different solvers are optimized for different sizes/kinds of systems, e.g., Martyna and Tuckerman's solver [76] is good for small gas-phase molecules.

3.4 POTENTIAL ENERGY SURFACE CALCULATIONS FOR A PAIR OF MOLECULES

A naive way of calculating the Potential Energy Surface (PES) between two molecules would be to calculate energy for the molecule pair and then subtract energy of the individual molecules from it. There are, however, two issues that need to be considered before doing this: Different calculations use different basis sets or the used calculation method works differently for different molecules.

The first of these problems is called *basis set superposition error* (BSSE) [78]. Because the basis set is different for different calculations it causes an error in the result. The way to solve this issue is to use the basis of the combined system for all calculations. In literature this is usually called as *counterpoise correction* [57, 58].

The second problem can be demonstrated with a method that represents wave function with two Slater determinants. In this case the wave functions for individual molecules would be

$$\Psi_A = a_1\Phi_{A1} + a_2\Phi_{A2} \tag{3.25}$$
$$\Psi_B = b_1\Phi_{B1} + b_2\Phi_{B2}. \tag{3.26}$$

Assuming that the molecules do not interact with each other the wave function for combined system would be

$$\begin{aligned}\Psi_{AB} &= \Psi_A\Psi_B \\ &= a_1b_1\Phi_{A1}\Phi_{B1} + a_1b_2\Phi_{A1}\Phi_{B2} \\ &\quad + a_2b_1\Phi_{A2}\Phi_{B1} + a_2b_2\Phi_{A2}\Phi_{B2}\end{aligned} \tag{3.27}$$

that is, a total of four Slater determinants. However, because the method does have wave function with only two Slater determinants, it would not be able to give this wave function. As a result, the energy of the non-interacting system would not be the sum of its two parts. The term used for this kind of behavior is *size inconsistency* [57, 58], and a method that does give same energy for the combined system is called *size consistent*.

Note that for a method to be a size consistent, the number combined-system wave function Slater determinants needs to be the same as the number non-interacting systems multiplied together.

In general, configuration interaction is size inconsistent, while couple cluster is size consistent.

It has become a norm that potential energy surface is usually calculated with CCSD(T) using the best available basis set, which in practice means the use of the *explicity correlated* (F12) method [79, 80] and the use of complete basis set approximation techniques [57] on top of that.[2]

2 A general attention should be paid in the method called DLPNO-CCSD(T)-F12 . While it is fast, the DLPNO part causes some bumps in PES at certain distances, and as a result it cannot be used in molecule pair PES calculations. By tuning DLPNO parameters this might be possible, but in general some kind of solution for this would be good in the future.

4

MOLECULAR VIBRATIONS

Born-Oppenheimer approximation leads to separation of nuclear and electronic motion. This results in a Hamiltonian that is in approximate block form, with blocks to nuclei and electrons, and their motion can be studied separately.

N atoms correspond to a vibrational Hamiltonian of $3N$ degrees of freedom. The resulting Schrödinger equation is thus a representation of a $3N$-dimensional unitary group. Because of special relativity, the Hamiltonian of this group commutes with space translations and rotations, as shown in Equation 2.76. This means that the Hamiltonian can be expressed in the block form related to these operators, *center of mass* (CoM) movement block that is a U(3) group, rotation block that is a SU(2) group and U$(3N-5)$ group for the rest of the degrees of freedom

$$H = \mathrm{U}(3N-5) \otimes \mathrm{SU}(2) \otimes \mathrm{U}(3). \tag{4.1}$$

This means that the eigenstates of this Hamiltonian are of the form

$$|\Psi\rangle = |\psi_{3N-5}\rangle \, |L, M_L\rangle \, |\boldsymbol{p}_{CoM}\rangle \, . \tag{4.2}$$

Molecular symmetry that is commonly used is the same as *symmetry of its vibrational ground state*. **This is different than the symmetry of the Hamiltonian!** The symmetry of the Hamiltonian is the highest symmetry that every term in the Hamiltonian satisfies. This means that the vibrational Hamiltonian can include terms that have different symmetry than that of the system system ground state. The reason behind this are conformers and isomers, all of which are states of the same Hamiltonian. Also broken symmetry means that, in practice, the true symmetry is hidden. For example, this can be seen in a case of Darling-Dennison resonance where it causes mixing between states of different symmetries (see section 4.3).

4.1 DIATOMIC VIBRATIONS

In a case of a diatomic molecule the Hamiltonian has the form

$$H = \mathrm{U}(1) \otimes \mathrm{SU}(2) \otimes \mathrm{U}(3) \tag{4.3}$$

and the resulting eigenstates are, by omitting CoM movement

$$|\Psi\rangle = |n\rangle \, |L, M_L\rangle \, . \tag{4.4}$$

The Hamiltonian can now be expressed with these quantum numbers as a Taylor series

$$H = \sum_{i,j,k} a_{ijk} (n + \frac{1}{2})^i [L(L+1)]^j M_L^k. \tag{4.5}$$

Because Hamiltonian commutes with rotation generators expressed in Equation 2.76, it must not depend on M_L and the final representation is

$$H = \sum_{i,j} a_{ij}(n + \frac{1}{2})^i [L(L+1)]^j \tag{4.6}$$

which is called as *Dunham expansion* [81].

Generally the Dunham expansion is considered to be semi-classical [82], because Dunham derived it using WKB-approximation. The derivation here points out that it is a much more general theory than is usually believed. In reality it is a consequence of special relativity and thus it is valid within quantum field theory.

Mesons are particles consisting of a quark and an anti-quark and their energies can also be expressed with the Dunham expansion

The first approximation of Dunham expansion is

$$H = (n + \frac{1}{2})\hbar\omega, \tag{4.7}$$

which is equivalent to harmonic oscillator approximation, where ω is a frequency at which the molecule is vibrating.[1] Adding next term to expansion yields

$$H = (n + \frac{1}{2})\hbar\omega - (n + \frac{1}{2})^2\hbar\omega x, \tag{4.8}$$

which is the Morse oscillator approximation [54, 83–85].

Rotations can be taken into account with term

$$H_{rot} = BL(L+1), \tag{4.9}$$

where B is called as *rotation constant*. Adding a term to this, it becomes centrifugal potential

$$H_{rot} = BL(L+1) - DJ^2(J+1)^2 \tag{4.10}$$

where D is the *centrifugal distortion constant*.

Terms that include both vibrational and rotational contributions such as

$$\alpha(n+1)L(L+1) \tag{4.11}$$

can be interpreted two ways: either the bond length is changing due to the increase of vibrational level (that affects the moment of inertia), or that increased rotation causes a change in vibrational energy due to the increase in centrifugal potential.

1 The method here is to use Lie groups and algebra to generate general form of systems and then realize them (homomorphism) as concrete physical equations. This is similar to what was done earlier in case of Schrödinger equation, and is also the way how Steven Weinberg is deriving physical theories in his quantum field theory book [42].

4.2 MULTI-ATOMIC MOLECULES

4.2.1 *Three-Atomic Molecule*

The simplest 3-atomic molecule consist of 3 atoms in a linear configuration (along the same axis) in either $D_{\infty h}$ or $C_{\infty v}$ symmetry. In both of these cases the Hamiltonian is partitioned to (omitting CoM movement)

$$H = \mathrm{U}(1) \otimes \mathrm{U}(1) \otimes \mathrm{U}(2) \otimes \mathrm{SU}(2), \tag{4.12}$$

where in $D_{\infty h}$ case the U(1) groups have different representations and in $C_{\infty v}$ case they have the same representation. U(1) modes are the symmetric and asymmetric stretching modes along bond axis (z-axis), and the U(2) group is bending modes perpendicular to the z axis [86].

The U(2) group can be divided to U(1) and SU(2) groups, see Equation 2.32, to give the Hamiltonian a representation

$$H = \mathrm{U}(1) \otimes \mathrm{U}(1) \otimes \mathrm{U}(1) \otimes \mathrm{SU}(2) \otimes \mathrm{SU}(2). \tag{4.13}$$

This means that degenerate vibration states can form internal rotations in the molecule. In terms of algebra, the operators for SU(2) are, using atomic units, [54]

$$J_+ = a_1^\dagger a_2 \tag{4.14}$$
$$J_- = a_2^\dagger a_1 \tag{4.15}$$
$$J_z = \frac{1}{2}(a_1^\dagger a_1 - a_2^\dagger a_2). \tag{4.16}$$

From these the quantities needed for the Hamiltonian in the position basis can be formed as

$$q = \sqrt{J} \sin\frac{\theta}{2} \cos\phi \qquad p = -\sqrt{J} \sin\frac{\theta}{2} \sin\phi, \tag{4.17}$$

so that the vibrational Hamiltonian for U(2) is defined by the U(1) part

$$H = \frac{p^2}{2m_{eff}} + V(q). \tag{4.18}$$

In harmonic approximation the energy is expressed as

$$H = (a_1^\dagger a_1 + a_2^\dagger a_2 + 1)\hbar\omega \tag{4.19}$$

and there is degeneracy with SU(2) group.

The first excited state has two states $|1\rangle|0\rangle$ and $|0\rangle|1\rangle$ that have the same energy. The second excited state has three states (left side harmonic oscillator states, right side the resulting rotation state)

$$|2\rangle|0\rangle = |1,1\rangle_{jm} \tag{4.20}$$
$$|1\rangle|1\rangle = |1,0\rangle_{jm} \tag{4.21}$$
$$|0\rangle|2\rangle = |1,\text{-}1\rangle_{jm} \tag{4.22}$$

which have same energy only in the harmonic approximation. When anharmonicity is taken into account, the state $|1,0\rangle_{jm}$ has different energy than the other two states and the energy depends on the square of the rotation quantum number m. It is customary to use letter "K" for this rotation number [85, 87].

Rotation changes sign under time-reversal operation, but Hamiltonian does not. Thus the Hamiltonian must depend on even powers of rotation quantum numbers.

The general state for the vibrations of a three-atomic molecule is thus

$$|\Psi\rangle = |\nu_1\rangle\,|\nu_2\rangle\,|\nu_3\rangle\,|\frac{\nu_3}{2}, K\rangle\,|L, M\rangle\,, \tag{4.23}$$

which means that molecule has 3 degrees of freedom for CoM (not shown here), 3 degrees of vibrations and 3 degrees of rotations. Two of the rotation degrees are associated with space rotations and one to internal rotation. The energy depends on 8 of these numbers, because the Hamiltonian commutes with rotation generators in Equation 2.76, and therefore it does not depend on M.

When molecule is linear, the ground state can only have $K = 0$. Additionally quantum number K can be ignored for the first excited states, because K^2 is same for all the first excited states and can thus be included in the vibrational energy change. In case of a V-shaped molecule, K is not limited to zero in the ground state and cannot be ignored. In general, the energy can depend only on the even powers of K, because the Hamiltonian is invariant under time-reversal symmetry. This leads to the Hamiltonian having a term

$$\frac{K^2}{2I}, \tag{4.24}$$

where moment of inertia I can be related to the anharmonicity constants.

4.2.2 *Four and More Atomic Molecule*

Adding an additional atom to linear molecule adds extra $\mathrm{U}(1) \otimes \mathrm{U}(2)$ term to Hamiltonian. For 4-atomic molecule the Hamiltonian is

$$H = \mathrm{U}(1) \otimes \mathrm{U}(1) \otimes \mathrm{U}(1) \otimes \mathrm{SU}(2) \otimes \mathrm{U}(1) \otimes \mathrm{U}(1) \otimes \mathrm{SU}(2) \otimes \mathrm{SU}(2). \tag{4.25}$$

Here, adding an extra atom introduces two vibrations and one internal rotation.

When constructing the Hamiltonian for this system, it can be noted that it depends on the K-values of both internal rotations and possibly from their combination K_1K_2. Based on this, the Hamiltonian includes terms such as

$$H \sim a_1K_1^2 + a_2K_2^2 + a_3K_1K_2, \tag{4.26}$$

because K_1K_2 is invariant under time-reversal symmetry. This $\mathrm{SU}(2) \otimes \mathrm{SU}(2)$ coupling causes an extra splitting for states that have excitations on both vibrations [54, 88, 89].

With this methodology, the vibrational state can be constructed to any molecule, using a linear molecule as a basis. The important message here is that molecules have potentially several internal rotation degrees of freedom that can absorb angular momentum, and that these rotations make it difficult to get simple Hamiltonian for vibrational systems.

Molecules can have higher symmetries too, all the way to 6-fold degeneracy in icosahedral molecules. In these cases there can be even SU(6)-SU(6) couplings.

4.3 COUPLINGS, RESONANCES AND SPLITTINGS

The resonance concept has its origin in experimental spectrum, where it was found experimentally that extra terms need to be added to the Hamiltonian in order to get a good fit [90]. The name resonance comes from the fact that only states that are relatively close in energy are mixed.

4.3.1 *Coriolis Coupling*

Internal rotation quantum numbers K and external rotation M can couple to each other in terms like

$$c_{11}KM \qquad c_{22}K^2M^2 \qquad c_{13}KM^3 \tag{4.27}$$

and so on. There are some restrictions to these because the Hamiltonian commutes with M, i.e., Hamiltonian does not depend on the axis of rotation. This means that these terms are a result of differences of internal and external angular momentum axes, or terms of type

$$c_i(M_i + K_i) \qquad c_i(M_i - K_i), \tag{4.28}$$

which must be in a product form due to Hamiltonian being a scalar

$$c_i(M_i + K_i)^m(M_i - K_i)^n, \tag{4.29}$$

with $m + n$ even. This kind of terms describe Coriolis-coupling [85, 91].

There is also a coupling related to Coriolis that lifts the degeneracy for $\pm K$ called called *l-doubling* [85, 86].

4.3.2 *Fermi Resonance*

Quantum mechanics in general has a property that states that have similar energy couple to each other. This effect is present in vibrational states, too. This kind of resonance coupling is called as *Fermi resonance* (FR) [54, 90, 92].

The simplest case is when the second excited state of a mode and the first excited state of a different mode have approximately the same energy. In this case the Hamiltonian includes a term like

$$K_{21}(a_2^\dagger a_1 a_1 + a_1^\dagger a_1^\dagger a_2). \tag{4.30}$$

This is called as 2:1 FR because one of the modes has 2nd excitation and the other has 1st excitation. In more complicated cases there can be 3:1, 2:1,1 etc.. Fermi resonance that have terms

$$K_{31}(a_2^\dagger a_1 a_1 a_1 + a_1^\dagger a_1^\dagger a_1^\dagger a_2) \tag{4.31}$$

$$K_{211}(a_2^\dagger a_3^\dagger a_1 a_1 + a_1^\dagger a_1^\dagger a_2 a_3) \tag{4.32}$$

The effect of FR on spectra is that it causes extra peaks to appear. The reason is that FR couples states that have a large difference in the intensities between them. Thus, the peak that normally has small intensity "borrows" some of the intensity from the other peak, which will result in a "new" peak appearing in spectrum. There is a symmetry rule for FR. The states that couple need to belong to same symmetry representation.

4.3.3 *Darling-Dennison Resonance*

If we pump energy to symmetric stretching modes such as O-H in water or C-H in benzene, we would expect that at some point all O-H and C-H should break at the same time. From experience we know that this is not the case and that the bonds break one by one. There must thus be an mechanism that changes the vibrations to be local. This effect is called the *Darling-Dennison resonance* (DDR) based on the original discovery on water [92–95].

The canonical DDR couples two quanta from one mode to two quanta on an other mode, resulting in Hamiltonian term of form

$$K_{DD}(a_1^\dagger a_1^\dagger a_2 a_2 + a_2^\dagger a_2^\dagger a_1 a_1), \tag{4.33}$$

which is also called as 2:2 DDR. Other types of DDR also exist, such as 3:3 and 4:4, or n:n in general.

This localization of vibrations is called as *local mode*. In general, all vibration modes became increasingly localized with higher excitations and it is standard to consider high overtone excitations as local modes.

The feature of DDR is that it couples modes with different symmetry together. This feature causes the symmetry of highly excited molecule to break, which is what we expect to happen.

While DDR is usually considered to occure between vibrations, it also couples internal rotation modes, such as the one described in subsection 4.2.2, which are example of 1:1 or 2:2 DDR [54].

Lastly there are couplings that do not fit either FR or DDR. These are called generally as *anharmonic resonances* [92].

4.3.4 *Polyadd*

When two vibrational modes do not interact with each other the Hamiltonian is in block form (here for two non-degenerate vibrations)

$$H = \begin{pmatrix} H_1 & 0 \\ 0 & H_2 \end{pmatrix}, \tag{4.34}$$

which in terms of Lie groups is two separate U(1) groups

$$H = \begin{pmatrix} H_1 & 0 \\ 0 & H_2 \end{pmatrix} \rightarrow \begin{pmatrix} U_1(1) & 0 \\ 0 & U_2(1) \end{pmatrix}. \tag{4.35}$$

The wave function is then the product of the individual vibrational Hamiltonians

$$|\Psi\rangle = |v_1\rangle |v_2\rangle . \tag{4.36}$$

If the two modes of vibrations have a weak interaction between them, which is the case in FR or DDR, the Hamiltonian have off-diagonal elements

$$H = \begin{pmatrix} H_1 & h_{12} \\ h_{21} & H_2 \end{pmatrix}. \tag{4.37}$$

In this case, the Hamiltonian is not composed of two separate Lie groups, but instead is a one two-dimensional unitary group

$$H = \begin{pmatrix} H_1 & h_{12} \\ h_{21} & H_2 \end{pmatrix} \rightarrow U(2). \tag{4.38}$$

The U(2) group can be expressed as a product of U(1) and SU(2) groups

$$H = \begin{pmatrix} H_1 & h_{12} \\ h_{12} & H_2 \end{pmatrix} \rightarrow U(2) = U(1)SU(2). \tag{4.39}$$

The wave function is then

$$|\Psi\rangle = |n\rangle |f(n), K\rangle , \tag{4.40}$$

where $f(n)$ depends on the type of resonance.

There is a connection between n and v_1 and v_2, which, i.e., in the case of 2:1 FR is

$$n = 2v_1 + v_2 \tag{4.41}$$

and in the case of 2:2 DDR is

$$n = 2v_1 + 2v_2. \tag{4.42}$$

The SU(2) group couples states that have the same quantum number n with ladder operators to form different K states. This means that the quantum number n called *polyadd* [54, 90, 92] can be used to indicate quantum numbers that couple to each other. In general, polyadd is better quantum number than the quantum numbers associated with the individual vibrations, because it stays relevant even on high excitation states, where the vibrations become localized.

When more than two vibrational modes couple, the Schrödinger equation is a $U(N)$ group, which can be transformed to an U(1) and a SU(N) groups. Polyadd is then the quantum number of the U(1) group.

4.3.5 *Renner-Teller effect*

Renner-Teller effect (RTE) [96–98] results from a coupling of internal rotations to the electronic angular momentum. The outcome of this coupling is that, in vibrational spectrum of degenerate modes the observed bands are split when molecule has electron angular momentum.

RTE is similar to spin-orbit coupling and it is a good reminder that all different angular momentums couple to each other.

4.3.6 *Broken Symmetry and Tunneling Splitting*

Symmetry breaking is a phenomenon where the symmetry of the Hamiltonian does not manifest itself in realized states [41, 52].

To demonstrate this, Figure 4.1 describes the eigenstates of the Hamiltonian

$$H = -\frac{1}{200}\frac{\mathrm{d}^2}{\mathrm{d}x^2} + x^4 - 3.4x^2 \tag{4.43}$$

that have been solved numerically. The Hamiltonian is even in the variable x because $H(x) = H(-x)$ and thus eigenstates are either even or odd functions. However, this is not the case for states 1 and 2, which are localized on different sides of the central (energy) barrier, and the symmetry of system is broken for these states. States 5 and 6 on the other hand, are clearly even and odd, and thus they represent the system symmetry. In this case the symmetry breaks because of numerical inaccuracies in the differential equation solver. When the eigenvalues of the two states become too small to be represented by floating point numbers, the symmetry breaks. In reality, symmetry breaking happens because of disturbances caused by fluctuations in quantities such as environment or temperature.

In this example, we could take linear combinations of states 1 and 2 and the symmetry would be restored, or that the symmetric states 5 and 6 are linear combinations of localized states. In the latter case we would say that there is a Darling-Dennison resonance that couples the localized states, which does give an explanation to why DDR exists. In a form of clear statement: when Darling-Dennison resonance couples two states with different symmetry, it is caused by broken symmetry being restored to original symmetry.

The most common example of symmetry breaking in chemistry is ammonia, which has a trigonal pyramid shape (C_{3v}) and can tunnel through a planar (D_{3h}) structure to the inverted state [52, 85–87]. Thus, D_{3h} would be the representation of the unbroken symmetry of ammonia. This is not true, however, because the four atoms of ammonia can be put on a line to form a linear $C_{\infty v}$ symmetric molecule, where the linear structure would be a local maximum. This same procedure applies for every molecule. Their atoms can be put on a line to form either a $C_{\infty v}$ or a $D_{\infty h}$ symmetric molecule. The outcome of this way of thinking is that every molecule that does not have either of these symmetries, is in a broken symmetry state.

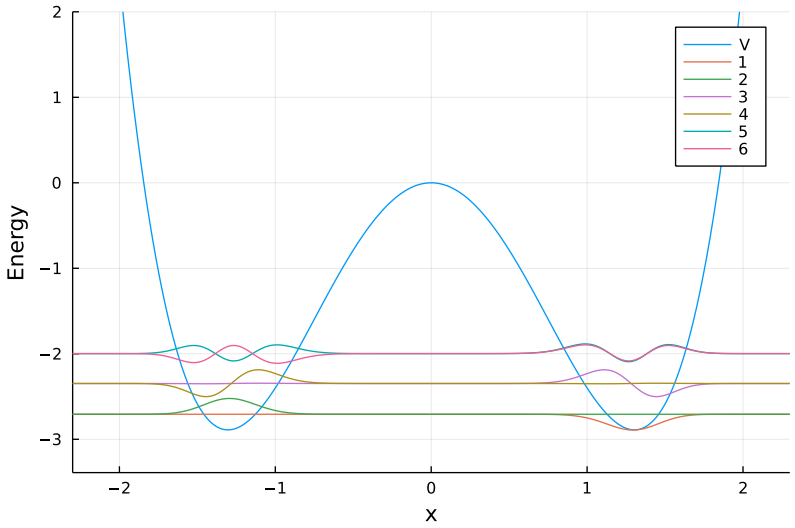

Figure 4.1: Symmetry breaking in vibrational states. States 1 and 2 are localized on one side, while states 5 and 6 are unbroken.

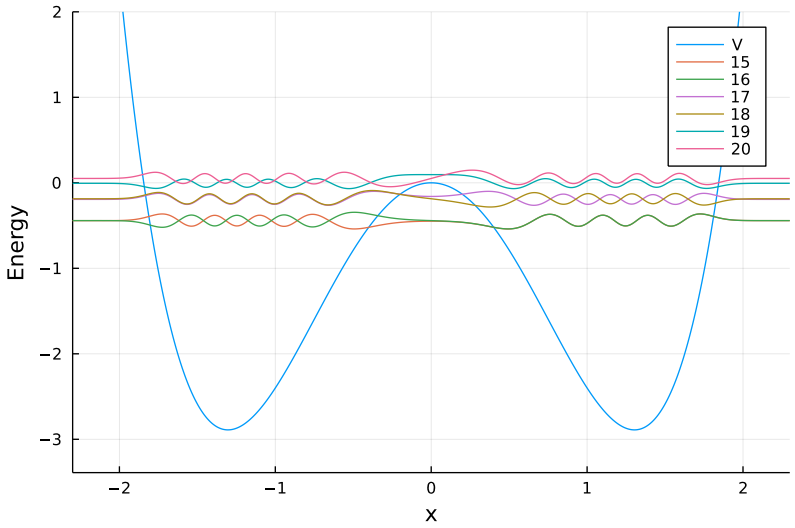

Figure 4.2: Tunneling splitting. States 17 and 18 have a small difference in energy called tunneling splitting.

In Figure 4.2, the higher excited states of the same Hamiltonian are pictured. From these states it is possible to see that the energy difference of a pair of states is getting larger the higher energy they have. This energy difference is called as tunneling splitting or sometimes as inversion doubling [85, 99, 100]. In general it is present when there is a potential barrier through which the wavefunction can tunnel.

4.4 NOMENCLATURE OF VIBRATION STATES

It is customary to use the Greek letter ν to mark vibrational quantum numbers. Numbering of vibrational modes starts from the highest-energy fundamental (normal mode) excitation and goes down in fundamental modes, so that the second-highest mode has number 2 and so on [87]. The ground state has quantum number zero. Table 4.1 presents a summary of the rest of the notation conventions [101].

4.5 METHODS TO CALCULATE MOLECULAR VIBRATIONS

The simplest way of calculating vibration states is the harmonic approximation, which is based on calculating potential energy Hessian. Expanding the potential energy in a Taylor series

$$V = E_0 + \sum_n a_n x_n + \sum_{m,n} b_{mn} x_m x_n + \dots \tag{4.44}$$

and taking the Hessian leads to

$$\frac{\partial^2 V}{\partial x_m \partial x_n} = b_{mn} + \dots . \tag{4.45}$$

By taking eigenvectors from the Hessian and using them as a basis for the Hamiltonian, results in a Hamiltonian that is diagonal to the second order of potential energy

$$H = \sum_i \left(-\frac{\hbar^2}{2m_q} \frac{\partial^2}{\partial q_i^2} + \frac{1}{2} b_i q_i^2 \right), \tag{4.46}$$

which yields normal modes and fundamental energies. This is the way how most quantum-chemical programs calculate vibrational states.

Harmonic approximation is a crude approximation and in practice it is only good for finding the normal modes, as the predicted energies can be hundreds of wavenumbers off. This is mostly because anharmonicity is ignored. Also, no rotation-vibration coupling is present and FR and DDR resonances are not present.

Rotation-vibration couplings can be taken into account with the Watson Hamiltonian [91, 102, 103] (here shown as expressed in the literature)

$$\begin{aligned} H = & \frac{\hbar^2}{2} \sum_{\tau,\eta} \mu_{\tau\eta} (J_\tau + \pi_\tau)(J_\eta - \pi_\eta) \\ & - \frac{\hbar^2}{8} \sum_\tau \mu_{\tau\tau} + \frac{1}{2} \sum_i p_i^2 + V \end{aligned} \tag{4.47}$$

Table 4.1: Explanation for vibrational state notation

Term	Description	Quantum state
ν_n	First excited (fundamental) state for mode n	$\|1_n\rangle$
$3\nu_n$	Third excited state for mode n	$\|3_n\rangle$
$\nu_n + 2\nu_m$	Combination state of states ν_n and $2\nu_m$	$\|1_n 2_m\rangle$
$2\nu_n\nu_m$	2:1 Fermi resonance for states n and m	$a_1 \|2_n 0_m\rangle + a_2 \|0_n 1_m\rangle$
$3\nu_n\nu_m + \nu_k$	Combination of Fermi resonance and mode k	$a_1 \|3_n 0_m 1_k\rangle + a_2 \|0_n 1_m 1_k\rangle$

Where J is the rotation angular momentum, π vibrational angular momentum, p_i the linear momentum, μ reciprocal inertia tensor and τ and η run though x, y and z coordinates. Term $-\frac{\hbar^2}{8}\sum_\tau \mu_{\tau\tau}$ is mass dependent and equal to zero for linear molecules.

The advantage of this form is that it can be expressed in terms with increased accuracy [104, 105]

$$H = H_{20} + H_{30} + H_{40} + \ldots \text{ vibration terms} \tag{4.48}$$
$$+ H_{21} + H_{31} + H_{41} + \ldots \text{ Coriolis terms} \tag{4.49}$$
$$+ H_{02} + H_{12} + H_{22} + \ldots \text{ rotation terms.} \tag{4.50}$$

From this form the different levels of theories can be generalized by taking into account different terms.

When these terms are added using perturbation theory the method in general is called as *general vibrational perturbation theory* (GVPT) [105]. The most common of these theories is *vibrational perturbation theory 2* (VPT2) [106, 107]. There are several VPT2 versions that differ from each other, according to the terms that are taken into account. Usually vibrational the potential energy is taken into account by including all 3rd-order and linear 4th order terms. This has consequences. Foremost, there is no DDR, as 2:2 DDR needs nonlinear 4th order terms, which means that VPT2 is not very good for higher excitation states [104].

There are vibrational calculation methods corresponding to most of the electronic-structure methods including vibrational self-consistent field (VSCF) [108, 109], vibrational second order Møller-Plesset theory (VMP2) [110–112], vibrational configuration interaction (VCI) [109, 113–115], vibrational coupled cluster (VCC) [115, 116] and vibrational density matrix renormalization group (VDMRG) [117] theories.[2]

These methods differ in the cases they are used for, as well as in their accuracy and computational expense. VPT2 is very cheap and does not need a PES calculation but it has limitations in its accuracy and it is applicable only to semi-rigid molecules. VCI, on the other hand is very accurate, but expensive and limited to systems consisting of up to about 20 atoms. It also needs a PES calculation and can handle molecules which are not rigid or semi-rigid, such as CH_5^+ [118].

The basis used in the calculations can consist of harmonic normal modes or solutions from VSCF. Methods that use PES also need some coordinate system in terms of which PES is defined. There is plenty of research in this direction [119–121]. On the negative side this can make very accurate calculations challenging, as a lot of time might be needed to find good custom coordinates.

When the PES is well constructed the more accurate methods VCI, VCC and VDMRG can reach one wavenumber accuracy that is sometimes referred to "spectroscopical accuracy".

2 VPT2 can be found on many programs such as Gaussian, Molpro and in the future also in ORCA. It is recommended to use it over harmonic calculations, as it is very easy to use and more accurate. VCI can be found from Molpro, but it is harder to use and needs some delving into. VDMRG is as accurate as VCI, but uses less resources. It is most likely that in the future VDMRG will become generally used golden standard method. however, at the time of writing this, its availability is scarce.

5 MOLECULAR DYNAMICS

In general, MD has use for two purposes of use: Calculation of dynamical properties and modeling statistical mechanics. Good understanding of the latter is needed to be able to properly apply MD.

There are two kinds of MD in common use at this moment. Classical MD, also called molecular mechanics (sometimes just molecular dynamics), uses parameterized force fields to calculate forces and ab initio molecular dynamics (AIMD) calculates forces by calculating electronic structure. There is also a combination of these two, QM/MM, where part of the system is handled quantum mechanically and part classically.

5.1 AB INITIO MOLECULAR DYNAMICS

When the Born-Oppenheimer approximation is valid, the wave function has the form

$$|\Psi\rangle = |R\rangle\,|\psi_e(R)\rangle \tag{5.1}$$

and the Hamiltonian has the form

$$H = -\frac{\hbar^2}{2M_R}\nabla_R^2 + H_e, \tag{5.2}$$

where H_e is electronic Hamiltonian, which includes nuclear repulsion potential.

Molecular dynamics uses classical point nuclei. The corresponding dynamical equations can be generated from the quantum Hamiltonian by taking the expectation value [73]

$$\begin{aligned} H_{classical} &= \langle H \rangle \\ &= -\langle R|\frac{\hbar^2}{2M_R}\nabla_R^2|R\rangle + \langle\psi_e(R)|H_e|\psi_e(R)\rangle \\ &\quad - \langle\psi_e(R)|\frac{\hbar^2}{2M_R}\nabla_R^2|\psi_e(R)\rangle \\ &= \frac{1}{2}M_R\dot{R}^2 + E_e - \langle\psi_e(R)|\frac{\hbar^2}{2M_R}\nabla_R^2|\psi_e(R)\rangle\,. \end{aligned} \tag{5.3}$$

The first term is the nuclear kinetic energy, E_e is the electronic potential energy or electronic potential energy surface, and the last term is similar to the kinetic energy and it can be considered to express the energy related to the change in the form of electronic density when nucleons move.

There are three different ways to handle the last term, leading to three different dynamical schemes [73]. The first one is to use quantum mechanics to propagate the changes to electronic state, which leads to *Ehrenfest molecular dynamics*. The second option is to ignore

The derivation here leads to non-adiabatic molecular dynamics, where nuclear motion does not affect the electronic state. When nuclear motion affects electronic states the corresponding dynamics is called as adiabatic, which is out of the scope of this Thesis.

There is an analogy here. Consider an air balloon. The air inside (electrons) has its own equation of motion that is confined to the shape of the balloon. When the balloon is deformed, the energy of the air inside stays same, but some energy is needed to reshape the confined air, which corresponds to the third term in equation (5.3).

the whole term, which is very small, leading to *Born-Oppenheimer molecular dynamics* (BOMD). The third option is to use classical field theory to propagate electron orbitals. This is a solution that works when a considerable band gap is present, so that the shape of the electron density can be considered to behave classically. In this case the Hamiltonian is

$$H = \frac{1}{2} M_R \dot{R}^2 + E_e + \sum_i \mu \dot{\phi}_i{}^2. \tag{5.4}$$

The last term includes an unknown fictive electron mass term μ and the time derivatives of orbitals $\dot{\phi}$. There is also an added constraint that the orbitals are orthogonal. This method is called as *Car-Parrinello molecular dynamics* (CPMD) [122].

The problem with the CPMD method is that mass related to the orbital shape change is unknown. The energy of the last term is, on the other hand small, so in practical calculations it is enough to have correct magnitude for this mass. Usually, the value for this fictive electron mass is in hundreds of atomic unit masses, depending on the nuclear masses and band gap. With lighter nuclei such as hydrogen, there is a need of smaller values. However, working values are always up to some testing. This means that properly done CPMD always includes a test run to see that all is working correctly in the simulation.

As a good starting point 400 a.u. is a good mass value for systems with hydrogen.

The choice of which MD method is used depends on the goal of the simulation. Ehrenfest dynamics has small time step (about 0.01 fs), because it is limited by electron propagation. On the other hand it is the most accurate method for electronic state propagation and is thus used when the electronic state is of primary interest.

In BOMD, the time step depends on nuclears and can be in the range of 0.5-5 fs, with hydrogen needing 0.5 fs time step. This means that BOMD simulations are capable of producing longer trajectories than Ehrenfest, and are thus suited for situations where nuclear motion is of interest.

The CPMD time step is also limited by electronic state propagation, with the values being between 0.07 and 0.25 fs, but because of the classical field theory, electron propagation is fast. The main reason to use CPMD in the past has been that it is faster than BOMD. Nowadays this advantage has diminished and AIMD has mainly been done with BOMD, which also avoids the hassle with the fictive electron mass.

5.2 QM/MM

In MD studies it is common that only a small part of a system is truly interesting and the rest of the system is there to just "fill surroundings". In these situations the interesting part of the system can be modeled quantum mechanically while the rest of the system is modeled classically [73, 123, 124]. An acronym QM/MM is used for such methods.

From a practical point of view QM/MM methods add an extra layer of complexity in the form of QM-MM boundary. There are in general three cases for the boundary.

1. Chemical bonds pass the boundary
2. Ion or dipole interactions take place over the boundary
3. Only dispersion taken place

Case 1 is common in biological systems, where QM part is commonly an active part of a protein. This is the most problematic case for simulations, as the boundary is prone to cause errors and special measures need to be taken into account to handle it [123]. In case 2, an extra information is given in input file to assign a partial charge to each atom in the QM system that can then be coupled to MM. Finally, in the last option, 3, only dispersion forces cross QM-MM boundary and only the description of dispersion forces is needed to be given.

5.3 INTEGRATORS

To perform a MD simulation the system needs to be propagated in time, which means that the associated differential equation (DE) needs to be integrated. In molecular dynamics it is important that the conserved quantities stay conserved during dynamics, meaning that only sympletic integrators [125] that are designed to conserve periodic movement, can be used [126]. Secondly it can be expected that the DE is also stiff. A simple rule of thumb is that, if DE has two variables that change at different time scales, the DE is likely to be stiff [127]. These requirements mean that the commonly used integrators like Runge-Kutta [127] cannot be used.

The most basic integrators used are variants of Verlet [128] or Velocity-Verlet [126, 129] algorithms. Also the newer leapfrog algorithm [130, 131] is in common use. The main difference between the different algorithms is at what length of the time step they become inaccurate.

If MD is done under constraints to atom movement, different set of integrators need to be used. SHAKE [132] and RATTLE [133] are versions of the Verlet and velocity-Verlet algorithms that can handle constrains. In simulations where pressure is also variable, the ROLL algorithm [134] can be used.

In gas-phase simulations additional care needs to be taken to make sure that the CoM movement and rotation are eliminated. The issue here is that, because of thermostat, extra energy can accumulate to these degrees of movement, which will distort the system from the desired temperature [73]. MD programs have options to do this after the integration step, and to use them is mandatory, when a thermostat is used in local mode with gas-phase systems.

5.4 STATISTICAL MECHANICS

A fundamental feature of statistical mechanics is the relation that gives the probability to find the system of interest in a certain state. Feynman stated: [135]

> This fundamental law is the summit of statistical mechanics, and the entire subject is either the slide-down from this summit, as principle is applied to various cases, or the climb-up to where the fundamental law is derived and the concepts of thermal equilibrium and temperature T clarified.

Derivation[1] of this fundamental law is started by stating the following axioms

1. Cluster decomposition principle - matter is composed of particles that can be studied independently [42].
2. There exists a probability that a particle is in a certain state.
3. Different states with the same energy have same probability.
4. Laws of physics are independent of the zero energy level.

Axioms 1 and 4 are symmetries, with the latter one being continuous, meaning that there is a Lie group associated with it. Axiom 2 defines that there is a probability ρ to find system a state n with energy E_n and 3 (also symmetry) defines that this probability depends only on the energy

$$\rho_n = \rho(E_n). \tag{5.5}$$

Probability is defined relative to other states

$$\frac{\rho(E_n)}{\rho(E_m)}. \tag{5.6}$$

Axiom 4 states that this relationship does not change, when zero-energy level is changed

$$\frac{\rho(E_n)}{\rho(E_m)} = \frac{\rho(E_n + E_0)}{\rho(E_m + E_0)}. \tag{5.7}$$

The simplest way to satisfy this is that probability is multiplied with some constant when the zero-energy level changes

$$\rho(E_n + E_0) = g(E_0)\rho(E_n), \tag{5.8}$$

where $g(E_0)$ is a Lie group element that can be expressed using an exponential map

$$g(E) = e^{-\beta E}, \tag{5.9}$$

The Lie group in this case is called as the general linear group over real numbers [45]. It is the same group that is behind, e.g., first-order reaction dynamics.

1 Derivation is based on Feynmans derivation [135], with some changes.

where β is a constant with the unit of one over energy. By noting that

$$\rho(E_n) = \rho((E_n - E_m) + E_m) = e^{-\beta(E_n - E_m)}\rho(E_m), \tag{5.10}$$

the Equation 5.7 can be expressed as

$$\frac{\rho(E_n)}{\rho(E_m)} = \frac{e^{-\beta(E_n - E_m)}\rho(E_m)}{\rho(E_m)} = e^{-\beta(E_n - E_m)}. \tag{5.11}$$

From this it can be concluded that

$$\rho(E) \propto e^{-\beta E} \tag{5.12}$$

and normalized probability (density) is

$$\rho(E) = \frac{e^{-\beta E}}{\sum_m e^{-\beta E_m}} = \frac{1}{Q} e^{-\beta E}, \tag{5.13}$$

where Q is called as the *partition function*. This equation is commonly know as the *canonical density function*.

In practical considerations it is more convenient to use the equation

$$\beta = \frac{1}{k_B T} \tag{5.14}$$

and call constant T as *temperature* and the unit conversion factor k_B as *Boltzmann constant* .

Thermodynamic quantities can be defined using probability density (V is volume) [135]

$$A_H = -k_b T \ln Q \qquad \text{free energy} \tag{5.15}$$

$$S = -k_b \sum_n \rho(E_n) \ln \rho(E_n) \qquad \text{entropy} \tag{5.16}$$

$$P = -\left(\frac{\partial A_H}{\partial V}\right)_T \qquad \text{pressure} \tag{5.17}$$

$$C_V = -T\left(\frac{\partial^2 A_H}{\partial T^2}\right)_V \qquad \text{heat capacity.} \tag{5.18}$$

When the energy of the system has a known fixed value, Equation 5.13 is not valid. In this case the probability is related to the density of states (DoS). For the most accurate formulation, an *integrated density of states* Ω needs to be used [2]

$$\rho(E) = \frac{\delta(E - H)}{\partial\Omega/\partial E}. \tag{5.19}$$

With this definition the entropy and temperature can be expressed as

$$S(E) = k_b \ln \Omega(E) \tag{5.20}$$

$$T(E) = \left(\frac{\partial S}{\partial E}\right)^{-1} = \frac{1}{k_b}\frac{\Omega}{\partial\Omega/\partial E}. \tag{5.21}$$

2 There has a long time been a discussion among physicists related to "negative absolute temperatures", which came to a conclusion only lately [136]. The result was that a bad definition of entropy leads to the concept of "negative temperatures" and that using a rigorous definition, such as expressed here, would lead to temperature always being positive. The issue here is that this is not yet well known and many sources still use the old, flawed definition.

The major difference between canonical and microcanonical (constant energy) systems is that the canonical system can be defined for all particle numbers, even for a single-particle system, while microcanonical assumes "thermodynamic limit" that is a very large number of particles. The consequence of this to MD is that the temperature of a constant-energy NVE simulation is not a good concept, while constant-temperature, NVT/NPT simulations are valid for even a single molecule.

In MD, the calculated temperature is kinetic energy divided by two times the number of degrees of freedom. This way of calculation is only valid at the "thermodynamic limit". For a small system, an average over time needs to be considered.

5.4.1 *Classical Statistical Mechanics*

In the classical context, energy is fully defined by position and momentum, so that probability ρ only depends on position and momentum, which leads to the concept of phase space [137]

$$\rho = \rho(\boldsymbol{p}, \boldsymbol{r}). \tag{5.22}$$

Additionally the kinetic energy and potential energy commute with each other, so that the classical partition function is a product of kinetic and potential parts (here for N identical particles) [135]

$$Q = Q_{kin} Q_{pot} \tag{5.23}$$

$$= \frac{1}{N!} \left(\frac{m}{2\pi\hbar^2\beta} \right)^{3N/2} \int e^{-\beta U(\boldsymbol{r})} \mathrm{d}^3\boldsymbol{R}. \tag{5.24}$$

This simplifies the calculation of the partition function.

In the case of a harmonic oscillator there exists a law called the equipartition theorem [137], which says that each harmonic mode has the same average energy

$$E = k_b T. \tag{5.25}$$

5.4.2 *Quantum Statistical Mechanics*

In quantum mechanics, the probability ρ becomes an operator $\hat{\rho}$ called the density operator (or matrix), sometimes also called as density operator [126, 135, 138, 139]. In canonical ensemble it has the form

$$\hat{\rho} = e^{-\beta \hat{H}}, \tag{5.26}$$

which has following diagonal expression

$$\hat{\rho} = \sum_n |\psi_n\rangle \, e^{-\beta E_n} \, \langle \psi_n| \tag{5.27}$$

and the partition function can be calculated by taking the trace

$$Q = \mathrm{Tr}[\hat{\rho}]. \tag{5.28}$$

Density matrix allows time-dependent quantum statistical mechanics formulations by taking the time derivative and using the Schrödinger equation [135]

$$\begin{aligned}\frac{\partial}{\partial t}\rho(t) &= \frac{\partial}{\partial t}\left(|\Psi(t)\rangle\langle\Psi(t)|\right)\\ &= \frac{\partial}{\partial t}\left(|U(t)\Psi(0)\rangle\langle\Psi(0)U^{\dagger}(t)|\right)\\ &= -\frac{i}{\hbar}H\rho(t) + \frac{i}{\hbar}\rho(t)H\\ &= -\frac{i}{\hbar}[H,\rho(t)],\end{aligned} \tag{5.29}$$

which is called as *Liouville-von Neuman equation*. To emphasize similarity to classical statistical mechanics this, equation is commonly written as

$$\frac{\partial}{\partial t}\rho(t) = \mathcal{L}(t)\rho(t), \tag{5.30}$$

where $\mathcal{L}(t)$ is the *Liouville superoperator*. Using basis where Hamiltonian operator is diagonal, this equation can be cast in the form (isolated system)

$$\rho_{nm}(t) = e^{i(E_m - E_n)t/\hbar}\,|n\rangle\langle m|\,. \tag{5.31}$$

In this form the diagonal elements always have real values that correspond to probability of finding the system in that state, and off-diagonal elements that rotate in the complex plane, with a frequency corresponding to the energy difference of states.

For practical calculations, the total system density matrix is seldom used. Instead calculations are usually carried out in a system which does not include the states describing environment. In this case, the external states are traced out, to form a reduced or subsystem density matrix

$$\begin{aligned}\rho_{sub} &= \mathrm{Tr}_{\text{external}}[\rho]\\ &= \rho_{nm}\mathrm{Tr}[|\psi_{ext}\rangle\langle\psi_{ext}|].\end{aligned} \tag{5.32}$$

A result of this is that each element of the *reduced density matrix* is a sum of different elements that have a small difference in energy. This leads to decoherence, where off-diagonal elements disappear with time Figure 5.1. [138]

To simulate this, the Liouville superoperator can be added with damping terms for the off-diagonal elements, that at their simplest have the form of an exponential decay. The equation used to propagate this kind of systems (open system) is called as Lindbland equation [138, 140]

$$\frac{\partial}{\partial t}\rho_{sub}(t) = -\frac{i}{\hbar}[H,\rho_{sub}(t)] + \mathcal{D}(\rho_{sub}(t)), \tag{5.33}$$

which can be expressed also as

$$\frac{\partial}{\partial t}\rho_{sub}(t) = \mathcal{L}(t)\rho_{sub}(t), \tag{5.34}$$

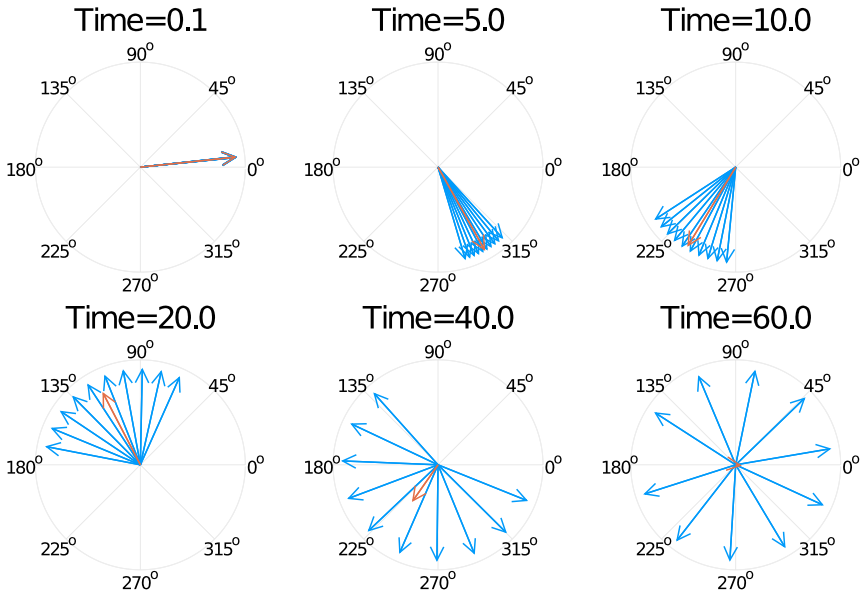

Figure 5.1: Decoherence. With time, the off-diagonal density matrix element (orange arrow) disappears, while the total system elements (blue arrows) lose coherence.

where $\mathcal{L}(t)$ now has additional terms called as *Lindbland operators*.

The following listing sums up different quantum statistical mechanic systems [138]

ISOLATED Time-independent Hamiltonian

CLOSED Time-dependent Hamiltonian

OPEN Time-dependent Hamiltonian with additional terms to model decoherence

5.4.3 *Radial Distribution Function*

Radial distribution function (RDF) is the probability to find two particles at given distance from each other [126, 135]. Its major use is based on its relationship to X-ray scattering. Additionally, calculation of certain thermodynamic functions is possible based on RDF, as well as structure parameters such as coordination number. It is not possible to use X-ray scattering to measure site structure in a matrix-isolation experiments. However, the radial distribution function can be used to give easy-to-read information on site structure, which can be used to distinguish different structures.

A standard way of parametrization the RDF is set to have value 1 for the average density, so that the value of radial distribution function is the probability relative to the average density. An integral yields number of particles minus one

$$4\pi \int_0^\infty r^2 g(r) dr = N - 1, \tag{5.35}$$

where, $g(r)$ is the radial distribution function.

5.5 THERMOSTATS

The "normal"MD is constant-energy microcanonical simulation with constant particle number, volume and energy (NVE) employed and enforced. Constant-temperature simulation in canonical ensemble with constant particle number, volume and temperature (NVT) can be done by adding a thermostat to the system. If the system has added thermostat and barostat, the simulation is then also isobaric addressing constant particle number, pressure and temperature (NPT).

Thermostats are used to generate the canonical density distribution. There are two ways how the termostats work. The first is by extending the system Hamiltonian and the second is by changing particle velocities so that MD would produce a correct velocity partition function.

A simple example of the latter type of thermostat is the Andersen thermostat [141], which samples particle velocities from the Maxwell distribution. A little more complicated is the Berendsen thermostat [142], where system experiences a force when the kinetic energy differs from the expected value ($\frac{1}{2}k_BT$). A modern version of canonical sampling through velocity rescaling (CSVR) [143] does not change the velocities in one step but, instead, accumulates the change through many steps.

Thermostats that extend the system are based on idea of mimicking a heath bath. The system is added with some external system large enough to uphold a heat reservoir. Examples of this kind of thermostats are the Nosé-Hoover thermostat [144–146] and its chain version [147].[3]

In modern use CSVR and Nosé-Hoover chain thermostats are usually good choices.

Different thermostats have different properties in how fast they produce the correct partition function and in which cases they can be applied. For example, it is known that the Nosé-Hoover thermostat does not work for the harmonic oscillator, a thing that is corrected with Nosé-Hoover chain thermostat, or that CSVR does not work for individual molecules.

Another important point when using thermostats is the region on which the thermostat is applied. It is possible to thermostat the global kinetic energy, or a single degree of freedom, resulting in the concepts global and local thermostat. In a global thermostat there is only one thermostat which will make sure that the global kinetic energy will have the correct distribution. In local (also called massive) case the system has a different thermostat for each degree of freedom attached to it. Also, most MD programs allow defining custom regions for thermostats.

Density matrix for constant energy harmonic oscillator for non-ground state has "bunny ears" at the both turning points. On the other hand, thermal density matrix represents a Gaussian distribution. The existence of "bunny ears" tells that the system is not properly thermostated.

The reason why regions are important is that the system might have degrees of freedom that are very weakly coupled to each other. This means that the energy is not exchanged between them, which results in a situation where the degrees of freedom might have a different temperature or that one or more degrees of freedom are not even being thermostated at all.

3 See also books, such as [73, 126], for thermostats, as they usually have a more comprehensive way presenting them than individual articles.

Finally, there exists new generation of thermostats such as colored noise [148–150] that allow not only thermostating, but with fine tuning they possess the ability to excite system in certain predefined ways.

5.6 BAROSTATS

When MD is done for a continuous system, the simulation is built up by repeating the simulation box. Changing the size of this box causes the system to experience different pressure, which is the basis of how barostats work [73, 126].

The simulation box is defined with Bravais lattice vectors $\boldsymbol{a}$, $\boldsymbol{b}$ and $\boldsymbol{c}$. These vectors are commonly expressed using *box/cell matrix*

$$\boldsymbol{h} = \begin{pmatrix} a_x & b_x & c_x \\ a_y & b_y & c_y \\ a_z & b_z & c_z \end{pmatrix}. \tag{5.36}$$

Cell volume is then

$$V = \det(\boldsymbol{h}) \tag{5.37}$$

and the metric tensor

$$g = \boldsymbol{h}^{\mathrm{T}}\boldsymbol{h}. \tag{5.38}$$

Coordinates in the system are given by

$$\boldsymbol{r}_n = \boldsymbol{h}\boldsymbol{s}_n, \tag{5.39}$$

where $\boldsymbol{s}_n$ are scaled variables. Total system energy is thus a function of $\boldsymbol{h}$.

Barostat is added to the system [73] by supplementing the Hamiltonian with a term describing the kinetic energy related to the cell matrix

$$E_k = \frac{1}{2} W \mathrm{tr}[\dot{\boldsymbol{h}}^{\mathrm{T}}\dot{\boldsymbol{h}}], \tag{5.40}$$

where W is the fictive mass that affects how fast the system responds to pressure changes, and a potential energy term due to external pressure p:

$$E = pV. \tag{5.41}$$

When equations of motion are developed for the cell matrix they yield

$$W\ddot{\boldsymbol{h}}_{uv} = V \sum_{k=1}^{3} (\Pi_{uk} - p\delta_{uk})(\boldsymbol{h}^{\mathrm{T}})^{-1}_{kv} \tag{5.42}$$

where δ_{us} is Kronecker delta and Π the internal stress tensor

$$\Pi = \frac{1}{V}\sum_n m_n(\dot{\boldsymbol{s}}_n^{\mathrm{T}} g \dot{\boldsymbol{s}}_n) - \frac{1}{V}\sum_k \frac{\partial E_{tot}}{\partial h_{uk}} h_{kv}^{\mathrm{T}}. \tag{5.43}$$

By adding a thermostat to the cell matrix, its movement can be tuned to respond to thermal fluctuations and thus create a NPT simulation.

6

SPECTROSCOPY

Spectroscopy is nonelastic scattering of light from matter and it is a special case of particle scattering in sense of particle physics [42]. The theory covering spectroscopy is called quantum electrodynamics (QED) [42, 151, 152].

QED is defined within a gauge [42], which can be chosen freely. The choice affects the form of equations and also, most importantly, whether or not charged particles and the electromagnetic field are separate entities or not. In close to the speed of light it is convenient to use the Lorentz gauge, but it results in the charged particle field and electromagnetic field partially merging. In the low-velocity regime, the Coulomb gauge is more useful. It also has a feature that the charged particle field and electromagnetic field are separable. This means that the system can be described as a tensor product of the particle field and electromagnetic field [151, 153]

$$|\Psi_{sys}\rangle = |\Psi_{particle}\rangle\,|\Psi_{em}\rangle\,. \tag{6.1}$$

This allows the electromagnetic field to be handled classically when photon number is very large, i.e., the electric field is not very weak. This further leads to a case where the electromagnetic field can be treated as a parameter [151, 153].

The second important approximation is a result from the fact that molecules are several orders of magnitude smaller than the wavelength of the photons that change their quantum state [151]. This leads to electric dipole approximation where interaction with photons reduces to electric dipole (μ) coupling to electric field

$$E = -\langle\hat{\mu}\rangle \cdot \mathcal{E}(t). \tag{6.2}$$

Spectroscopy can be divided to two parts, linear spectroscopy and nonlinear spectroscopy. Linear spectroscopy has two photons in its processes and nonlinear one has more than two [151, 153]. In this Thesis only linear spectroscopy is considered in form of vibrational infrared and Raman spectroscopies.

There are no one-photon process, because momentum conservation requires at least two photons.

Because two photons are needed in a linear process, a time difference between these two photons is also present. This enters the equations in the form of a time-dependent expectation value [86, 151, 153–155]

$$\langle(\hat{\mu}(t)\cdot\vec{\mathcal{E}}(t))(\hat{\mu}\cdot\vec{\mathcal{E}})\rangle\,, \tag{6.3}$$

where t is now time from the first interacting photon.

For linear polarization this leads to equation [153, 154]

$$\begin{aligned} P(t) &= \frac{i}{\hbar}\int_0^t \mathrm{d}\tau \vec{\mathcal{E}}(\tau)\vec{\mathcal{E}}_0 \left\langle \hat{\mu}(\tau)\hat{\mu}\right\rangle \\ &= \frac{i}{\hbar}\int_0^t \mathrm{d}\tau \vec{\mathcal{E}}(\tau)\vec{\mathcal{E}}_0 \left(\mathrm{Tr}[\hat{\mu}(\tau)\hat{\mu}\rho] - \mathrm{Tr}[\hat{\mu}\hat{\mu}(\tau)\rho]^*\right). \end{aligned} \tag{6.4}$$

The way how to interpret this is that the first dipole operator excites the system and then dipole moment is measured after time t *to get the value of polarization.*

A Linear spectrum, such as infrared, is just a Fourier transformation of this. In practical calculations the electric field magnitude is often ignored, which leads to a response function.

6.1 LINE SHAPES

A mathematical description of spectroscopy starts with a density matrix element [154]

$$\left|\psi_0\right\rangle\left\langle\psi_0\right|. \tag{6.5}$$

The first photon changes this to

$$\left|\psi_1(t)\right\rangle\left\langle\psi_0(t)\right| = e^{-i\omega_{01}t}\left|\psi_1\right\rangle\left\langle\psi_0\right|, \tag{6.6}$$

which rotates in time. If this rotation happens at the same frequency at which the electric field oscillates, absorption happens. This is theoretically equal to a Fourier transformation of an off-diagonal density matrix element. This, however, requires that the off-diagonal element lives forever, meaning that there is no decoherence.

If there is a decoherence that is modeled with the open-system formalism, the off-diagonal element has a finite lifetime. As an example, an exponential decay leads to the form

$$e^{-i\omega_{01}t}e^{-t/T_d}\left|\psi_1\right\rangle\left\langle\psi_0\right|, \tag{6.7}$$

where T_d is a constant called *dephasing time*. A Fourier transform of this leads to a function describing line shape [154]

$$A(\omega) \propto \mu_{01}\frac{1/T_d}{(\omega-\omega_{01})^2 + 1/T_d^2} \tag{6.8}$$

for absorption (μ_{01} is transition dipole moment), which is called as *Lorentzian* or *homogeneous line*. The full width half maximum (FWHM) of the Lorentzian line is

$$\Delta\nu = \frac{\Delta\omega}{2\pi} = \frac{1}{\pi T_d}. \tag{6.9}$$

If there are several overlapping vibrational modes, the resulting line shape takes the form of a Gaussian function and is denoted as *inhomogeneous line*. This kind of situation arises when different molecules have slightly different environments and the environments change slower than the photon absorption time scale.

1. Environment changes faster = homogeneous line shape

2. Environment changes slower = inhomogeneous line shape
3. Environment changes roughly with the same rate = system couples to environment

There are several factors that determine the line width. Thermal movement causes a Doppler shift, collision of gas phase molecules, radiative decay and so on [86]. In general, lower temperature and more inert environment lead to sharper lines.

6.2 RAMAN SCATTERING

Raman scattering is a four-photon process, which depends linearly on the electromagnetic field strength [153]. In Raman scattering a photon gets absorbed and an other photon with a different energy is emitted.

The intensity of the scattered radiation is related to [151]

$$I_{Raman}(k) = \frac{NI_L k^4}{16\pi^2\varepsilon_0^2}\left|\sum_a\left(\frac{\mu_{1a}\mu_{a0}}{E_{a0}-\hbar ck_L}+\frac{\mu_{1a}\mu_{a0}}{E_{a0}+\hbar ck}\right)\right|^2, \tag{6.10}$$

where k_L is the incoming light wave vector, k the scattered light wave vector, N number of molecules, I_L the incoming light intensity and ε_0 vacuum permittivity. The expression in brackets is usually written as

$$\sum_a\left(\frac{\langle\psi_1|\mu_i|\psi_a\rangle\langle\psi_a|\mu_j|\psi_0\rangle}{E_{a0}-\hbar ck_L}+\frac{\langle\psi_1|\mu_j|\psi_a\rangle\langle\psi_a|\mu_i|\psi_0\rangle}{E_{a0}+\hbar ck}\right)=\langle\psi_1|\alpha_{ij}|\psi_0\rangle, \tag{6.11}$$

where the second rank tensor α is called as polarizability.

α is symmetric only in an approximation, which is valid when the incoming light is resonant or near-resonant with the system [151]. When this is not true, α also spans the antisymmetric vector presentation.

Different components of the α_{ij} tensor cause scattering to different directions. When scattering is measured perpendicular to the incoming light components, α_{xy}, α_{xz} and α_{yz} contribute, while in the parallel case the components α_{xx}, α_{yy} and α_{zz} contribute.

Scattered radiation can have its energy either increased or decreased and, as a result, spectrum will have two branches. The names anti-Stokes for the increasing branch and Stokes for the decreasing branch are used [87].

6.3 VIBRATION SPECTROSCOPY

Vibrational transitions happen in the infrared (IR) energy region and the associated absorption spectroscopy is thus called as IR spectroscopy. Usually, the spectrum is measured in the range $200-4000\,\mathrm{cm}^{-1}$ that includes practically all fundamental modes, while the higher-energy regions only include overtone and combination transitions.

The region below $200\,\mathrm{cm}^{-1}$ includes pure rotation transitions. In matrix environment rotations are blocked by surrounding matrix atoms and the spectrum consist of lines where molecule is librating in the matrix site. The libration spectrum is usually ignored, as interpreting it is very complicated.

There are some molecules that are almost spherical and can rotate in matrix, e.g., *hydrogen.*

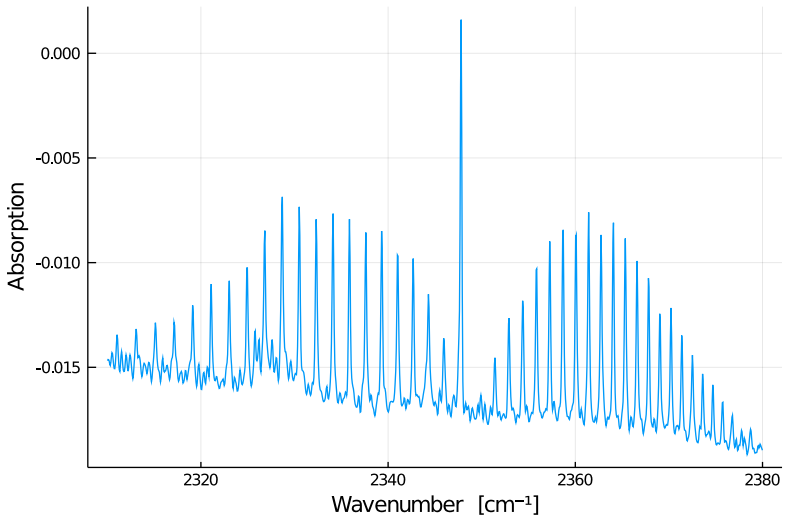

Figure 6.1: CO_2 rotation-vibration spectrum trace in the IR spectrum [157]. Gas-phase CO_2 causes P- and R-branches, while condensed CO_2 causes the tall peak in the middle.

Also in the matrix environment and other condensed systems, coupling between molecules happen at low frequencies, which causes some complications to the spectra.

Photons are particles with ± 1 angular momentum along the momentum axis [42], which has to be conserved in vibrational transitions due to conservation of total angular momentum. The result is a rotation-vibration spectrum, where the vibrational transition either increases or decreases molecular rotation. In an IR spectrum rotation, the angular momentum change is ± 1. This results in two distinguishable branches in the spectrum: the P-branch where the angular momentum decreases, and R-branch where it increases. There is also a Q-branch in between these two, where the internal angular momentum change conserves angular momentum [86, 87, 156].

If rotation is hindered due to condensed phase, such as matrix, the P- and R-branches disappear and the resulting spectrum is considerably sharper, see Figure 6.1.

The Raman spectrum depends on polarizability that is second-rank tensor, which spans representations for $\Delta J = 0, \pm 2$ [86, 87]. $\Delta J = \pm 1$ is also present when the symmetric approximation is not valid. The result is that the Raman spectrum has similar branches that are called the O-branch for -2 and S-branch for $+2$, with Q-branch in the middle for $\Delta J = 0$.

With Raman spectrum, the rotation selection rules depend on which scattering angle has been used the measurements to collect the spectroscopic information, see Equation 2.63 to Equation 2.68. A 90-degree scattering only has y xy, xz and yz components and, thus, does not include the $\Delta J = 0$ component and, thus, only has the Q-branch, if internal rotation is possible. 180-degree angle, on the other hand only has xx, yy and zz components, resulting in total absence of $\Delta J = 1$ components.

6.3.1 *Determination of Active Vibration Modes*

For a vibration mode to be visible in the spectrum it must have a non-zero matrix element. For an IR spectrum this means that the element

$$\langle \psi_1 | \mu | \psi_0 \rangle \tag{6.12}$$

must be non-zero. For Raman, the element is

$$\langle \psi_1 | \alpha | \psi_0 \rangle \,. \tag{6.13}$$

When transitions are from/to the vibrational ground state this means that the excited state needs to have the same symmetry as μ or α, to be visible in the observed spectrum.

To find out which representations the vibrations span it is necessary to find out which representations the nuclear movement spans. This is done by finding out what kind of representations the nuclear position vector R_i can span. This is done by calculating traces, from a matrix representation, for it under each symmetry operation and then forming a linear combination of representations that yields those traces. This linear combination also includes the CoM translations and rotations, which need to be reduced [47, 48, 86].

An easy way of doing this is to calculate traces for atom identities and multiplying that with the sum of x, y and z representations

$$\Gamma_{vib} = \Gamma_{atoms} \otimes (\Gamma_x \oplus \Gamma_y \oplus \Gamma_z) \ominus \Gamma_{CoM} \ominus \Gamma_{rot}. \tag{6.14}$$

Those vibration modes that have same the representation as the components of a vector (x, y, and z in character table) are IR active. With Raman, the selection rules are more complicated. The usual way of looking at them is to use xx, yy, zz, xy, xz and yz markings in character tables to identify the representations that are Raman active. Another possibility is to use the SO(3) representation of the polarizability tensor to find the Raman active modes. The advantage with this approach is that it can tell which rotation selection rules each mode will have. For example, the $J = 0$ representation is always fully symmetric, and because every molecule has at least one totally symmetric vibration mode that only changes the bond lengths, every molecule has at least one Raman active mode.

6.4 CALCULATING VIBRATION SPECTRUM WITH MOLECULAR DYNAMICS

Non-dynamically calculated vibration spectrum is in practice a spectrum of isolated gas phase molecule(s) that does not include line shapes.[1] To calculate line shapes, MD needs to be employed. The reason here is that in condensed phase the phase space in the near the neighborhood of the molecule becomes exponentially large and the methods that are based on eigenvalues cannot scan this phase space.

1 A good overview article on how to calculate the vibration spectrum with MD is Thomas et al. [158].

The spectrum is calculated by taking the Fourier transform of the autocorrelation function [158]

$$\int \langle f(t+\tau)f(\tau)\rangle \, e^{-i\omega t} \mathrm{d}t \tag{6.15}$$

In case of an IR spectrum this is autocorrelation of the dipole moment, see Equation 6.4. The autocorrelation function is usually calculated by Wiener-Khintchine theorem [158, 159]

$$\langle f(t+\tau)f(\tau)\rangle = \frac{1}{2\pi} \int \left| \int f(t) e^{-i\omega t} \mathrm{d}t \right|^2 e^{i\omega t} \mathrm{d}\omega \tag{6.16}$$

to get a better scaling ($N \log N$) compared to raw direct calculation (N^2). The resolution of the resulting spectrum depends on how long the trajectory is. To gain $1\,\mathrm{cm}^{-1}$ accuracy the trajectory needs to be about 60 ps long. The maximum frequency is determined by the time step. The standard time step for MD is about 1 fs, which is enough to have maximum of about $10000\,\mathrm{cm}^{-1}$, which is more than enough to capture fundamental transitions.

Usual IR-spectrum calculations have trajectory length of 20-40 ps. But for matrix spectrum this is too inaccurate and it is recommended to use a longer trajectory for matrix.

In case of QM/MM-calculation the dipole moment can be taken directly from the QM-system. When the spectrum is calculated for a liquid or solid, e.g., liquid water, a simple dipole moment is not available. In this case either Wannier centers (old method) [73] or Voronoi tassellation (new, recommended) [160] needs to be used to get the dipole moments of individual molecules.

A spectrum can be calculated from an individual trajectory or taken as a sum of several trajectories. In either case, if the trajectory or sum of trajectories produces the correct partition function, the spectrum can be considered to be computed correctly.

Calculating Raman spectrum is more complicated than the IR spectrum, because it depends on polarizability rather than dipole. To compute Raman spectra, first a trajectory needs to be generated. Then the same trajectory needs to be computed again for several times while applying a constant electric field to x-, y- and z-directions separately. Then it is possible to extract polarizability with the use of equation [158]

$$\mu = \alpha \mathcal{E} + \mu_0 \tag{6.17}$$

$$\alpha = \frac{\mu - \mu_0}{\mathcal{E}}, \tag{6.18}$$

as a difference in polarization when changing the external electric field.

It is also possible to assign peaks based on MD-spectra. To do this, either the power spectrum [158] or a colored-noise thermostat [148–150] can be used. In practice these are in a way the two sides of the same thing. A power spectrum is calculated from the velocity autocorrelation function

$$P(\omega) = m \int \langle \dot{\mathbf{r}}(t+\tau)\dot{\mathbf{r}}(\tau)\rangle \, e^{-i\omega t} \mathrm{d}t. \tag{6.19}$$

By choosing which atoms are taken into account, the peaks in the spectrum can be localized to a certain part of the system. A colored-noise thermostat, on the other hand, can be tuned to excite the system

with a certain frequency. The resulting trajectory then includes only oscillations that have the given frequency.

Part II

RESEARCH

7 OVERVIEW

The research in this Thesis consist of two different topics: calculating spectra for molecules embedded in a noble gas matrix and simulating the effects of overtone vibrational excitations in the gas phase and in a low-temperature matrix environment.

The main hypothesis in this Thesis is that the QM/MM method is a good way of simulating molecules in a low-temperature matrix. The research shows how this method can be used to calculate the site structure and link it then to vibrational spectra relevant for experimental studies.

The other hypothesis is that, by manipulating velocities of atoms in a molecule, a vibrational overtone excitation can be modeled. From this it follows that an estimate of how long it takes for the energy dissipate to the matrix and how it causes reactions in the system can be calculated by MD.

Chronologically the work started with gas-phase excitation simulation and followed by creating a framework that allowed simulations in a matrix. This was done by creating easy-to-use programs that allowed calculating and fitting interaction potential energy surfaces for large-scale modeling. These potentials were utilized in a robust MD simulation procedure developed for matrix simulations. Finally, MD-based vibrational spectra of several chemical systems were computed along with an excitation simulation in the matrix.

The created programs and simulation procedures allow squeezing of the human working time to only a couple of hours, and the simulations can be completed in about a week for the spectral calculations of one molecule. For excitations, the simulation time is determined by how long excitation trajectories are needed, with the limit being about 20 ps per day, due to a smaller-than-usual time step.

Because of the QM/MM method, the simulations are very light on resources and a workstation-class computer can perform the required calculations in a month. For small molecules the total cost of calculations is about 50000 core hours when computing the vibrational spectrum. Of this time allocation about 70% is consumed by MD and 30% is consumed by the potential calculation. For larger molecules the potential calculation part can be expected to take considerably more resources, because of the scaling difference between DFT and CC.

8 RESEARCH METHODS

8.1 DEVELOPED PROGRAMS

In this Thesis research several computer programs were developed. The source codes and documentation for these programs are available at Github https://github.com/MatrixLabTools. The most up-to-date information on how to use every program is given in the online documentation of each program and is thus omitted here. Instead the emphasis here is on the capabilities of each program and why they were done.

The program that calculates and fits PES was divided into three different programs which either calculate, fit or store the PES. The reason for this division is to limit the needed dependencies to the minimum, which will help run the software on supercomputers and makes it easier to develop the individual parts. All three programs where written using the Julia programming language [161].

8.1.1 *Calculating PES*

The program made to calculate PES between two molecules can be found from https://github.com/MatrixLabTools/PotentialCalculation.jl

It will call an external program to do electronic structure calculations. The programs currently supported are ORCA [162, 163] and Psi4 [164].

The program itself samples input coordinates used in electronic structure calculations. The Sampling, which can be configured by user, is done by first taking a random orientation of the two molecules and then finding a minimum distance where the interaction potential is smaller than a given cut-off value. When this point is found, the called external program calculates the interaction potential on several points with a distance larger than the cutoff point, in a "straight line fashion", see Figure 8.1 for a visualization. The number of points, the maximum distance and the maximum energy are input parameters of the sampling.

BSSE is taken into account when the energy is calculated, using counterpoise correction [58], with monomers frozen in the calculation. There is a more accurate method to take BSSE into account [165]. However, such a correction would need the calculation of gradients, which would we extremely costly at the CCSD(T)-F12 level. Also, F12 and basis-set limit estimation restricts the benefit of a more accurate method.

The result of these features is that the program only needs to be given the geometry of the molecule(s), maximum distance, maximum energy and number of computational points as an input. It also has the ability to make restart files, so that long calculations can be interrupted

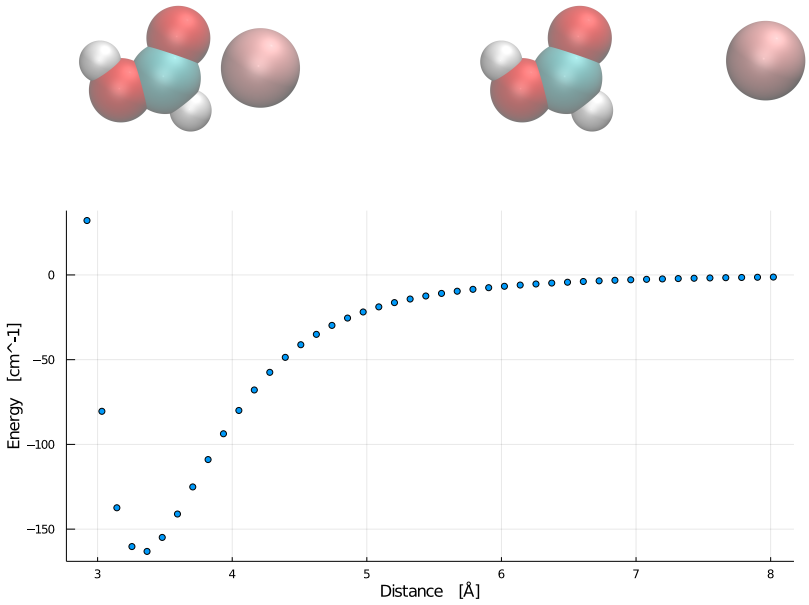

Figure 8.1: Potential is sampled in lines that can be visualized.

and then restarted from a saved point. Finally, the program can be run in parallel across different nodes.

8.1.2 *Fitting Potential*

Fitting and visualization program can be found from
https://github.com/MatrixLabTools/PotentialFitting.jl

The fitting can be done using any linear model [166] supported by Scikit-Learn [167], such as least-squares, ridge regression, support vector machines etc. The type of potential can be customized easily. The standard potential type is a polynomial with negative powers

$$E(r) = \sum_n \frac{c_n}{r^n}. \tag{8.1}$$

The powers are input parameters that can be customized for each individual atom in a molecule. New potential types can be written easily with Julia, and the program can handle both pair- and cluster potentials, as long as they can be linearly fitted.

Fitting can also be customized by applying weights on the fitting data. These weights can be applied based on energy or geometry of molecules, such as bond angles or bond lengths.

This program allows plotting PES, as shown in Figure 8.1 and fitting the PES using Scikit-Learn .

Finally, the program has tools to visualize the calculated and fitted data. Calculated data can be visualized with plots Figure 8.1. The plotting also allows representing the data in the same figure, which allows easy visual comparisons in order to identify where the fit deviates from the data significantly.

8.1.3 *Storing PES*

To store the calculated PES data, a special storage program was made https://github.com/MatrixLabTools/PotentialDB.jl
The purpose of this program is to make handling the potentials easy and also to make them easily available.

There is also a long term goal that, once a large number of potentials have been stored, they could be used to generate deep-learned potentials which could be used to a large set of molecules. This would be especially good for large molecules, for which CC becomes too expensive.

8.1.4 *IR spectrum calculation*

To make IR spectrum calculation easy, a program
https://github.com/MatrixLabTools/IRSpectrum.jl
that calculates spectrum from dipole moment trajectory was made. This program is a very simple and its main point is to automate the IR spectrum calculation.

8.2 USING PROGRAMS TO GENERATE AND FIT PES

8.2.1 *General Guidelines to PES calculation*

PES calculation itself was done by first generating a gas-phase trajectory for a molecule at high temperature, around 500 K. This trajectory is then used as an input for the potential calculation program that samples random points from it.

The number of "lines" that needs to be sampled depends on the molecular system studied. In general, something around 30 proved to be good value for small molecules such as the formic acid.

The number of points per "line" needs to be large enough that the potential minimum is captured. This means than the points need to be separated by less than 0.2 Å. If the maximum distance is 9 Å and the lower cutoff is around 2-3 Å. This means that at least 50 points need to be calculated per "line".

These kind of minimum requirements lead to about 1500 points needed to be calculated in total. Then, in the case of benzene, for example, for a PES of type

$$E(r) = \sum_{n=6}^{12} \frac{c_n}{r^n} \tag{8.2}$$

this results to 750 points per atom and over 100 points per potential parameter.

The maximum energy in the PES defines on what kind of calculations the PES can be used for. If the maximum value is low, such as 5000 cm^{-1}, the potential can be used to calculate the fundamental vibrational region of the IR spectrum. On the other hand, for calculating vibrational excitations it is not usable, because the excitations

are higher in energy. For this reason it is recommended to calculate the potential with relatively large maximum energy, such as 15000 or 20000 cm^{-1}.

The calculations employed in this Thesis were done by first sampling the calculation points with a cheap method, such as MP2, and then calculating the final energy with CCSD(T)-F12 [80, 168] with the cc-pVDZ-F12 basis and complementary auxiliary basis set (CABS), to improve accuracy.

8.2.2 *Fitting Potential*

The type of fitted potential is limited by the capability of the used MD-program. In this study, CP2K [169] was used. The QM/MM implementation in CP2K only supports pair potentials, which gives an ability to freely tailor the pair potential to the needs for the systems under study. This means that any pair potential that is linearly fittable can be used with CP2K.

In most of the cases pair potential was found out to be adequate. After some trial-and-error testing, the form in equation (8.2) was found out to be the most generally applicable. There was, however one notable exception - nitrogen. When trying to fit pair potential for formic acid interacting with the nitrogen molecule, the accuracy was unacceptable, with relative errors being more than 100% in some areas. In this case the fit quality could be improved considerably with a cluster potential of the form

$$E(r,\theta) = \sum_{n=6}^{12} \sum_{m=0}^{4} \frac{c_{nm} \cos^m \theta}{r^n}, \tag{8.3}$$

where θ is the angle between the bond axis of N_2 and the distance vector from nitrogen atom to the atom, for which the potential was fitted for. With this form relative errors were around 20% at maximum. On the other hand, usually the errors were much smaller. Nevertheless, since such potentials are not supported by CP2K, the calculations in the nitrogen matrix had to be dropped for time being in this context.

For noble-gas matrices, of which Ar and Ne matrices were studied in this Thesis, there were no problems in fitting the pair potential.

To do a fit on calculated PES, constraints are needed, because the potential of a form like equation (8.2) is used for fitting. The fit is heavily influenced by short-distance repulsion, because the potential can have very large values here. Thus, there is a need to add a small weight on the large values at short distance. Another issue is the bottom of the potential well, which is defined with a relatively small number of points, and thus possesses a small weight in fitting. But for the applications of potential, the bottom of the well is the most important part of PES. Thus, extra weight need to be applied to points in the potential well.

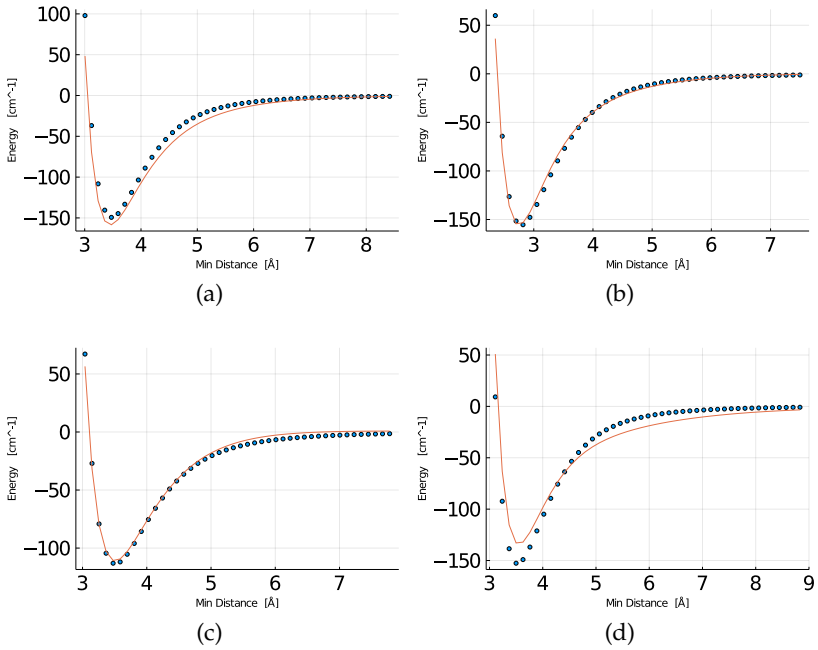

Figure 8.2: Examples of the potential fit quality on the cis-formic acid. Blue balls are the calculated values and the continuous line is the fitted potential.

Based on these consideration, a scheme for applying weights was made as follows:

$$w = \begin{cases} 0.01 & E > 5000\,\mathrm{cm^{-1}} \\ 0.1 & 1000\,\mathrm{cm^{-1}} < E \leq 5000\,\mathrm{cm^{-1}} \\ 1 & \text{-}50\,\mathrm{cm^{-1}} \leq E \leq 1000\,\mathrm{cm^{-1}} \\ 2 & \text{-}75\,\mathrm{cm^{-1}} \leq E < \text{-}50\,\mathrm{cm^{-1}} \\ 4 & \text{-}100\,\mathrm{cm^{-1}} \leq E < \text{-}75\,\mathrm{cm^{-1}} \\ 16 & E < \text{-}100\,\mathrm{cm^{-1}}. \end{cases} \tag{8.4}$$

For argon potentials this scheme worked for all the tested molecules, including interactions with formic acid, glycolic acid, benzene and nitrogen. Changing the weight scheme a little can cause small improvement in the fitted PES. However, no major changes were found with the systems studied in this Thesis. Finally, if the potential has a very large maximum value in the sampling phase, an extra term for the existing, very large values need to be added. This situation comes from the very short distances, where the potential is very steep, which can lead to a situation, where the maximum value in the potential can be significantly larger than the threshold value given to the program. The extra term, in fitting process, is needed to limit the contribution of this point to not distort the potential in more important points, such as at the potential well minimum. Finally, for other elements than argon, a change in the threshold values needs to be made in order to take into account the different potential well depths.

In Figure 8.2, an example of what a potential looks like after the fitting is presented. The general trend is that the fit is pretty good in (b) and in (c), but there are small deviations (a) and a little bit larger deviations (d) here and there. In general, the maximum relative errors at the bottom of the potential well are about 20% relative to the well depth, but remaining usually below 10% on average.

The quality of the fit could be expressed with root-mean-square deviation (RMSD), but it will suffer from the same issues than the fit itself. This means that it is heavily influenced by areas which are not that important for the actual calculations. However, if the calculation of RMSD is limited to the potential well area, by only taking points that have energy less than -10 cm^{-1}, a typical fit with the above weight scheme should give around 10 cm^{-1} RMSD.

Finally, the potential fitting program allows flagging two or more atoms as symmetric, meaning that the program knows they need to have same pair potential. With this feature, e.g., the benzene potential fit is done so that all carbons use the same potential.

8.3 MD SIMULATIONS

The point of using CP2K [169] was that it includes a good collection of thermostats, barostats, constraints, functionals and custom potentials packed to a single package, together with the QM/MM framework. This means that a single program could be used to do all the MD calculations, which was useful to devise an easy-to-use approach to support the experimentalist with relevant computational matrix data.

8.3.1 *System Preparation*

The MD simulations were done by first generating an initial gas-phase state and then condensing that to a solid matrix, where the actual calculations were done.[1] In total there are three phases in the system preparation: The first step is the equilibration of the gas-phase system. Secondly, the system is condensed to a solid matrix. At the third stage, the computational level is elevated (from semi-empirical to DFT) and the equilibration is repeated.

To save computational resources the condensation phase is done using semi-empirical methods. This way it can be done on a desktop computer, using a single core in about three hours. The exact semi-empirical method is not important, as there will be a equilibration phase later. In this Thesis, AM1 [170] and PM6 [171] methods were used in the semi-empirical step. If the studied system is a complex of two or more molecules, the semi-empirical method also needs an additional dispersion functional for the cluster to be more appropriately adjusted to describe intermolecular interactions. In this case, it is also better to use more accurate semi-empirical methods, such as PM6.

1 The online documentation has a complete working example, including input files, of a MD simulation
https://matrixlabtools.github.io/PotentialFitting.jl/stable/exampleusecase/

The initial gas-phase system was chosen to have 1000 atoms for the matrix in a 86 pm box, in all of the studied cases. The studied molecule was first put in the center of the simulation box. Temperature was chosen to be close to the boiling point of the chosen matrix atom, e,g., for argon 80 K was used. This system was run with NVT ensemble for 10 ps to equilibrate it.

The condensation was done in the NPT ensemble. At this point the temperature was made equal to the final matrix temperature. CSVR thermostat was used with massive region setting. The system was condensed by propagating in time for 100 ps. The time constant for the CSVR thermostat was set to 250 fs during the condensation process. This latter point is very important! While 250 fs is very large in normal use, here it is necessary, as it influences heavily the rate of condensation. If smaller values are used the condensation takes longer and the system might not condense even in 1 ns. The temperature also influences the condensation. This was especially an issue with the neon matrix, which needed a 5 K final temperature to condense, while argon system can be condensed in temperature as high as 80 K.

In the final preparation step, the system was swapped to use DFT and it was equilibrated for 10 ps in the NPT ensemble with the massive CSVR thermostat.

8.3.2 *Spectral Calculation*

To calculate spectrum a set of trajectories is generated. The initial point of each trajectory was generated separately with the method described above. The trajectory was generated using the NVE ensemble to generate trajectories of 40-60 ps long. The spectrum is then generated from the dipole moment trajectory, by taking a Fourier transformation of the autocorrelation function,[2] see section section 6.4.

The longer-than-normal trajectories give the IR spectrum a sub-wavenumber accuracy, which then allows classification of different site structures. The classification is based on the fact that when in a single trajectory the site structure does not change, its spectrum can be compared to other trajectories, see Figure 8.3. This, in turn, can be used to identify the site structures from experimental spectra.

Site identification is based on the fact that the whole trajectory stays in the same site. However, for practical calculations some of the trajectories do change sites, which can be seen as the peaks splitting in to several peaks. To reduce this, it is recommended to use a low temperature during the simulation.

As demonstrated in Figure 9.1, the resulting spectra have all the fundamental modes in the $200 - 4000\,\mathrm{cm}^{-1}$ region (a) and the first overtones and peaks representing the combination transitions in the $4000 - 8000\,\mathrm{cm}^{-1}$ region (b). Also very small traces of the second OH-

2 A program was made to make this step trivial. It takes as an input the dipole trajectory generated by CP2K.
https://github.com/MatrixLabTools/IRSpectrum.jl

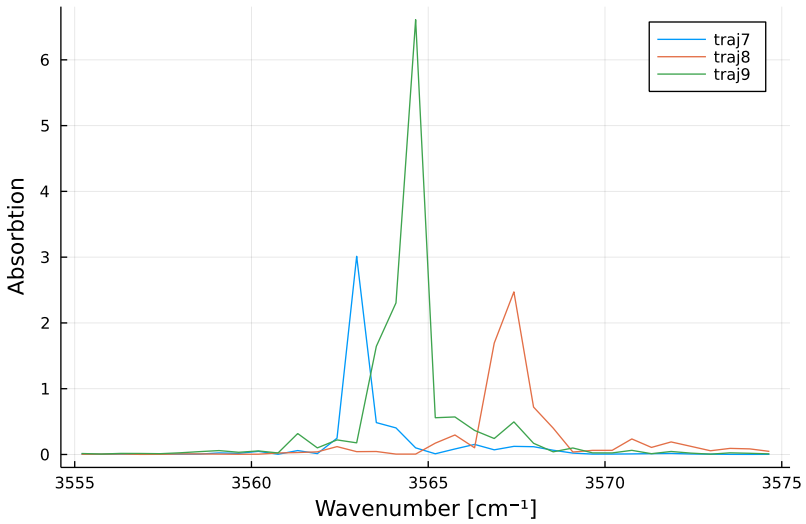

Figure 8.3: Example of the site structure appearing in the computed vibrational spectrum of formic acid.

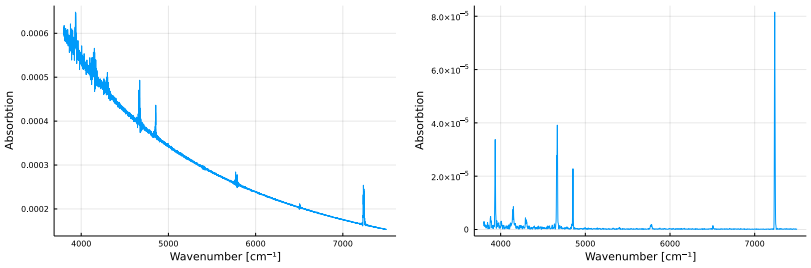

(a) (b)

Figure 8.4: Normal (a) and deconvoluted (b) spectrum

overtone can be seen in the $> 10000\,\mathrm{cm}^{-1}$ region, but these are so small that they are ignored here.

In the vibrational overtone region, the peaks are of low intensity and in some cases noisy. To make them more readable, peak finding software [172–175] was used to deconvolute the spectra, Figure 8.4.

8.3.3 *Simulating Excitations*

Molecular dynamics allows calculation of dynamical properties and one of the applications is simulating vibrational overtone excitations. This was done for gas-phase and matrix-embedded molecular systems.

In the gas phase the system was prepared by simply doing an equilibration run for a single gas-phase molecule. In the matrix, the system preparation procedure was the same as used for the spectrum calculation.

The way the excitation was simulated was that the energy of the excitation was added as kinetic energy to the molecule, by changing the velocities of O- and H-atoms so that the OH-bond would stretch while the center of mass would not move.

After this the system was propagated in the NVE ensemble to see if the molecule would change orientation or conformer.

9 CALCULATED SPECTRA

9.1 FORMIC ACID

The formic acid - argon potential used was made by combining the 5440 points of tFA and 5440 points of cFA to a total of 10880 points. Out of these points, 1280 were calculated with very high cutoff value of 20000 cm^{-1} and rest were calculated with low 5000 cm^{-1} cutoff.

This potential was found to have almost the same accuracy as the potential fitted for only one conformer. Thus, the data of both conformers were combined to create a potential that could later be used to do vibrational-excitation simulations as well.

Total of 20 trajectories for both conformers were generated, all represented at the temperature of 20 K. The generated trajectories were 60 ps long, the time step was 0.25 fs and the computed dipole moment was saved at every time step. The reason for using a small time step was to see its possible influence on the accuracy of the computed spectrum.

9.1.1 *Trans-Formic Acid IR Spectrum*

The spectrum is depicted in Figure 9.1, with the locations of peaks[1] listed in Table 9.1. Identification reveals all the fundamental peaks, and combinations of fundamental transitions are present in the spectrum. No Fermi resonance peaks where found. There is a very small trace of peak around 11000 cm^{-1} that could be identified as $3\nu_1$, but it is so small that it is left out from the discussion. No other peaks can be found at $> 7000\,cm^{-1}$.

Zoom in on the OH stretching vibration is shown Figure 9.2a. This reveals a four peak fine structure. Individual trajectories are depicted in Figure 9.2b in deconvoluted form, which was chosen because many of the trajectories had a lot of noise. It should be noted that because there were only a total of 20 trajectories, this fine structure could be a coincidence rather than a general finding.

Finally, the RDF was calculated for all the trajectories. From these, the H_{oh}-Ar distribution, Figure 9.3, was the most varied one, indicating that it would be the best one to identify different site structures.

Comparing calculated spectrum to the experimental one Table 9.1, we can see that there is shift in positions that is in order of ten wavenumbers for the fundamentals and of the order of hundred for

1 The calculated peaks are given as a range in which the peaks appear in the spectrum instead of the location of maximum peak position. The reason is that there is noise in the spectrum, which could move the location of the peak and secondly because MD allows calculation peak shapes. So the intent is that the range gives more information of the peak than simple peak maximum.

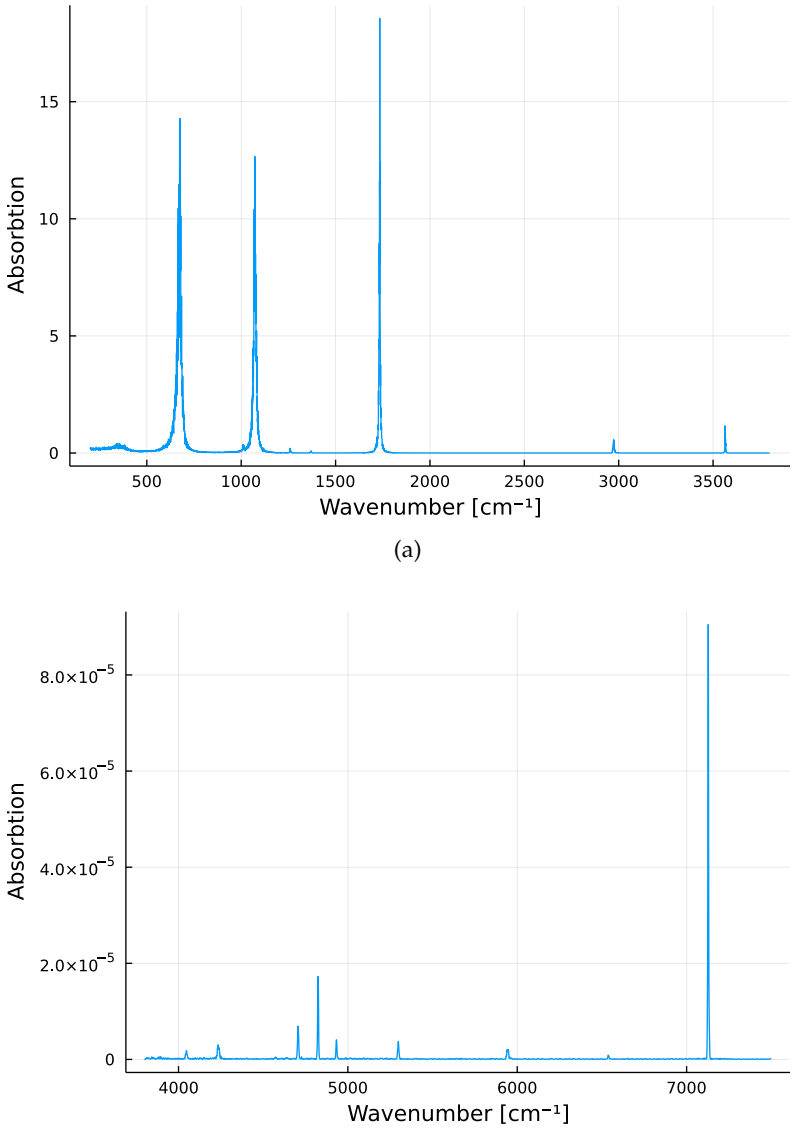

Figure 9.1: tFA IR-spectrum, fundamental (a) and overtone (b) regions.

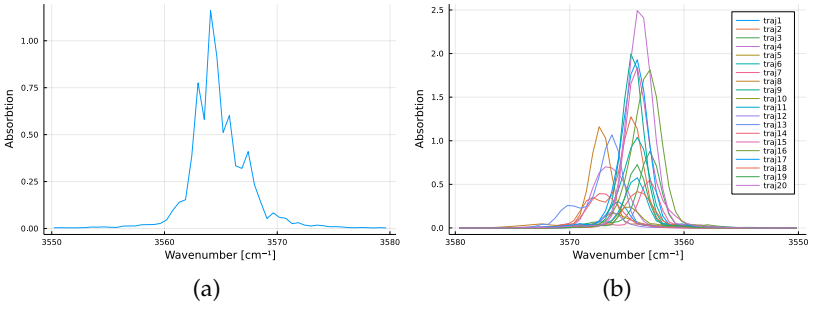

Figure 9.2: tFA acid OH-stretch. Average (a) and individual deconvoluted trajectories (b).

Table 9.1: Trans-formic acid peak positions. Different sites are indicated for experimental data with "/"-mark.

	MD	VCI[176]	Exp [13]	Exp[177]		MD	VCI[176]	Exp[177]
ν_7	667-673	627	629.2	628.0/629.3	$\nu_2+\nu_6$	4041-4045	4043	4059.7/4055.3
ν_9	675-680	638	635.2	635.4/635.4	$\nu_1+\nu_9$ or $\nu_2+\nu_5$	4230-4240		
ν_8	1008-1013	1034	1037.4	1037.4/1038.5	$\nu_2+\nu_3$	4702-4710	4713	4707.0/4706.0
ν_6	1069-1075	1108	1103.4	1103.9/1103.6	$\nu_1+\nu_5$	4822-4827		
ν_5	1259-1261	1222	1215.8	1214.8/1215.8	$\nu_1+\nu_4$	4930-4935		4928.7
ν_4	1367-1372	1380	1381.0	1384.4/1381.0	$\nu_1+\nu_3$	5295-5300		5315.4/5317.2
ν_3	1732-1737	1783	1767.2	1768.9/1767.2	$2\nu_2$	5938-5950		5803.0
$2\nu_6$	2130-2160	2205	2194.8	2196.1/2195.1	$\nu_1+\nu_2$	6535-6542		6411.2
ν_2	2970-2976	2938	2952.9	2956.1/2953.1	$2\nu_1$	7125-7130		6930.3/6934.8
$2\nu_3$	3460-3470	3547	3515.9	3519.0/3515.7				
ν_1	3562-3567	3575	3550.5	3548.2/3550				

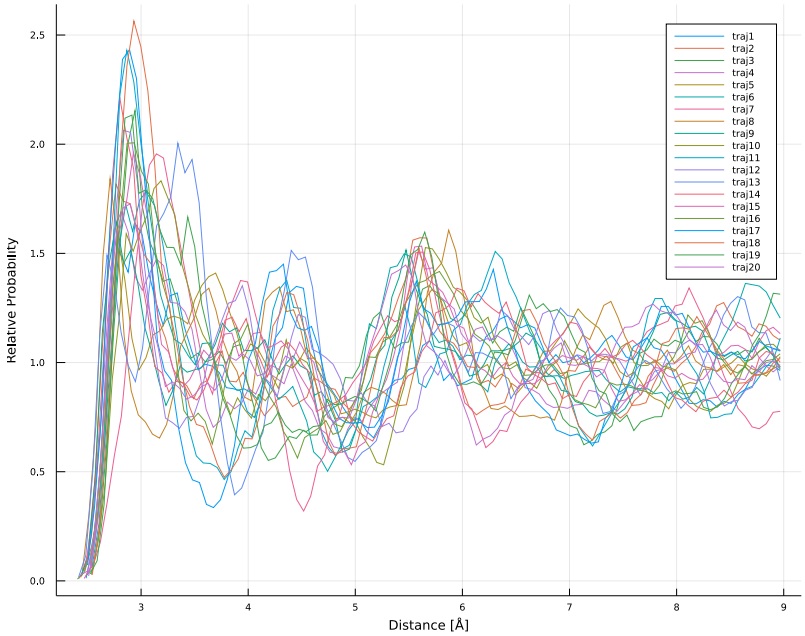

Figure 9.3: tFA RDF (H_{oh}-Ar) for individual trajectories.

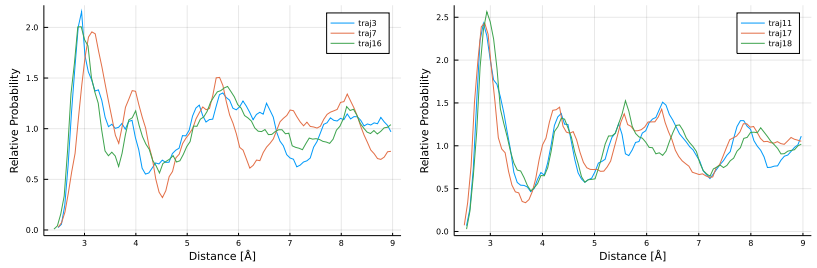

(a) (b)

Figure 9.4: Radial distribution functions (H_{oh}-Ar) for the two identified tFA sites, square (a) and triangle (b).

the overtones. These shifts were expected, as BLYP has limitations in accuracy.

9.1.1.1 *Site Structure*

There are two ways of finding out the site structures from the computed data. First, this is done by grouping the individual trajectories based on similar locations of peaks. The second way is based on the similarity of the obtained RDF. Ideally, we would like these two to agree with each other.

By using the first method, based on Figure 9.2b, there are two groups of peaks for the OH-stretch and, thus, we could expect these two to be due to different sites. However, this is not supported by the RDF, where the same grouping does not exist.

Using the second option, grouping based on the RDF, leads to two groups, as shown in Figure 9.4. The spectra of these two groups also forms two groups (Figure 9.5). Visual inspection of the site structures seen in Figure 9.6 confirms that these form two groups, noted as

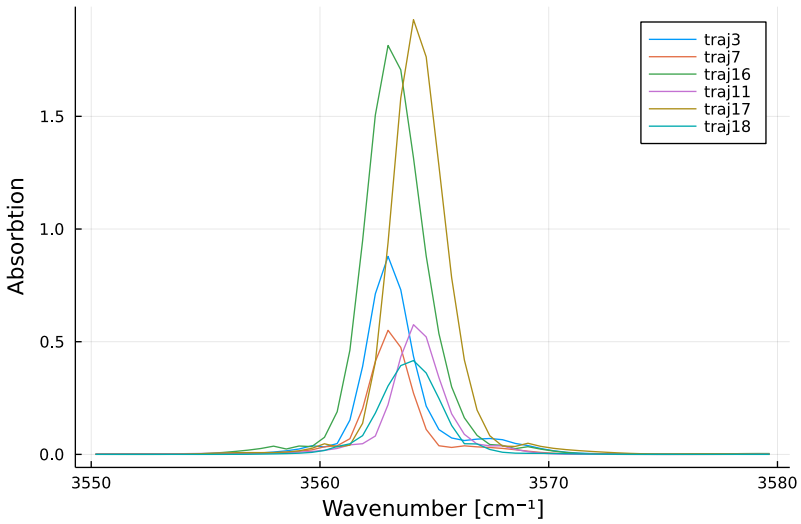

Figure 9.5: Deconvoluted spectra of the two identified tFA sites.

"square" Figure 9.6a and Figure 9.4a and "triangle" in Figure 9.6b and Figure 9.4b. From these two sites, the "triangle" one has an OH stretching band appearing at about 2 cm^{-1} higher than for the "square" site structure. The two sites are the two leftmost subpeaks shown in Figure 9.2a.

The other trajectories, around 60% of all trajectories, mainly form peaks mostly higher than or, in some cases at the same location than what is obtained for the "triangle" site. the RDF data of these trajectories do not group up and looking at trajectories themselves confirms this. There are essentially two kinds of trajectories here: Fore some the site site structure is changing, whereas some have a chaotic structure.

9.1.2 *Cis-Formic Acid Spectra*

The calculated spectrum for cFA, and the OH peak can be found from Figure 9.7. The peak positions are listed in Table 9.2. Computed RDFs for the individual trajectories are depicted in Figure 9.8. Computed trajectories and the overall OH stretching peak are shown in Figure 9.9.

The overall spectrum shown in Figure 9.7 has visible peaks for the fundamental combinations and first overtones, like in the case of tFA. The difference is that the local site structure for OH-stretch is more complicated than in case of tFA, which is seen from the RDF visually and by calculating the RMSD between trajectories. Individual trajectories differ from each other much more and there seems not to be a similar division to two groups as in the case of tFA. The consequence of this is that it is not possible to identify different site structures for cFA. The only thing that can be said is that the OH-hydrogen has the same kind of triangle-square local structure as found for tFA, see, e.g., Figure 9.10. However, it is not possible to identify the distinct peaks because the OH-tail site structures seem to change in the trajectories.

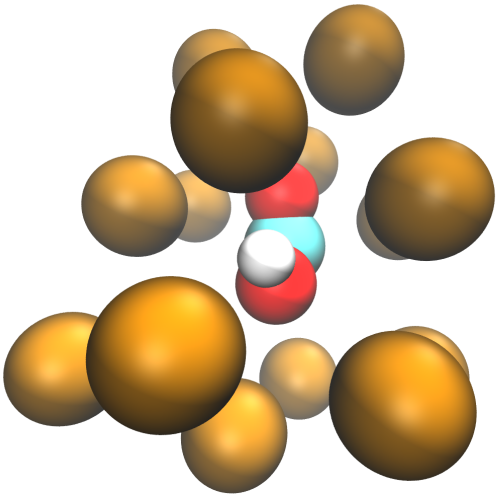

(a)

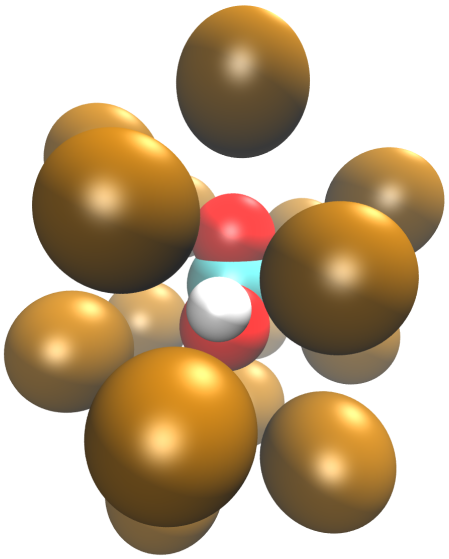

(b)

Figure 9.6: Identified tFA sites “square” (a) and “triangle” (b)

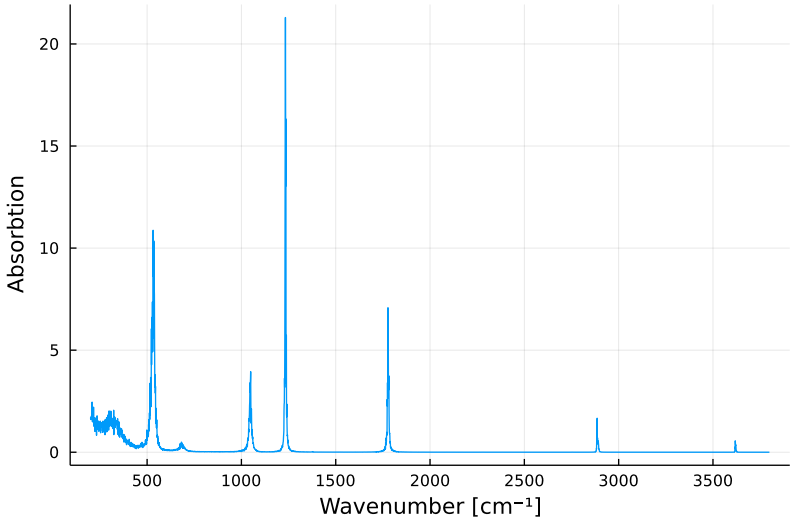

(a)

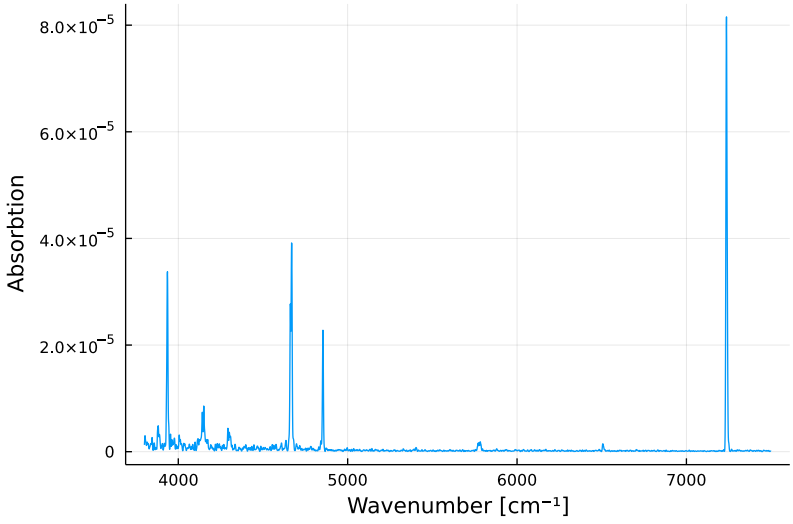

(b)

Figure 9.7: Cis-formic acid IR spectrum, fundamental (a) and overtone (b) regions.

Table 9.2: Cis-formic acid peak positions. The entries marked with * have different assignment than given in the experimental data source [177].

	MD	VCI[176]	Exp[13]		MD	Exp[177]
ν_9	520-540	492	503	$\nu_2+\nu_6$	3932-3940	
ν_7	677-685	661	661	$\nu_1+\nu_9$	4137-4157	
ν_8	1045-1050	1038	1108	$\nu_1+\nu_7$	4290-4310	
ν_5	1231-1235	1255	1244	$\nu_2+\nu_3$	4660-4675	4704.0/4700.0
ν_4	1375-1380	1394	1396	$\nu_1+\nu_5$	4850-4857	4847.7/4854.4*
ν_3	1775-1780	1824	1808	$2\nu_2$	5765-5790	
$2\nu_8$	2082-2088	2074		$\nu_1+\nu_2$	6502-6510	
$\nu_5+\nu_8$	2275-2282	2304		$2\nu_1$	7232-7240	7062.2/7065.7
$\nu_5+\nu_6$?	2382-2386	2340				
$2\nu_5$	2460-2470	2503				
$2\nu_4$	2754-2758	2759	2760*			
ν_2	2884-2887	2880	2899			
$\nu_3+\nu_6$?	3075-3100	3084				
$2\nu_3$	3550-3562					
ν_1	3615-3625		3618			

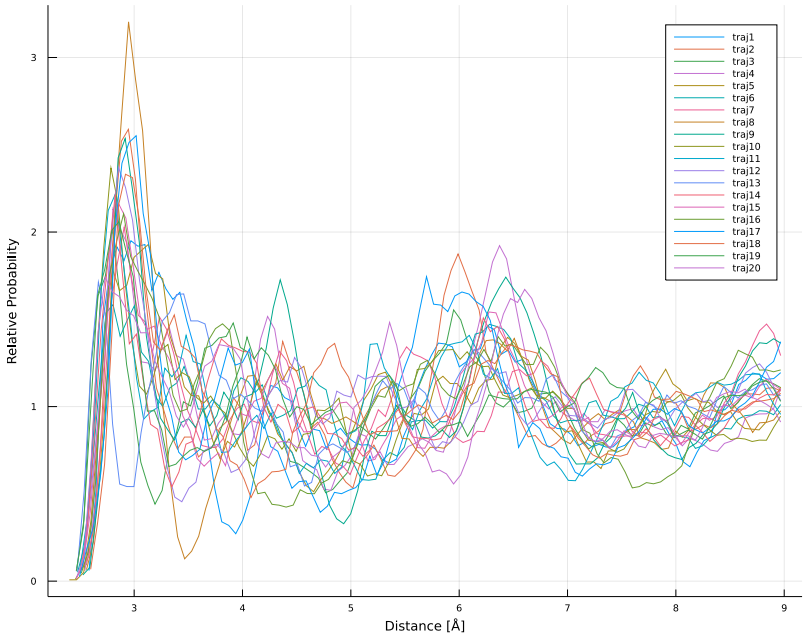

Figure 9.8: Cis-formic acid radial distribution function (H_{oh}-Ar) for individual trajectories

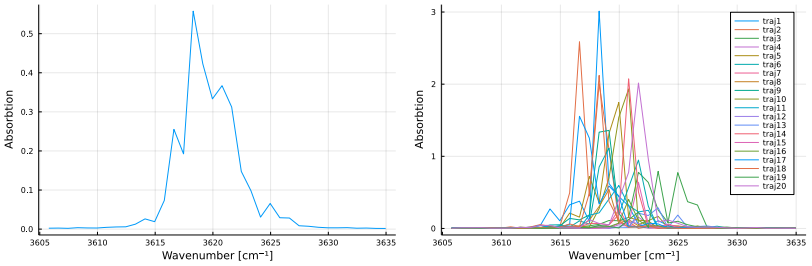

(a) (b)

Figure 9.9: cFA OH-stretch mean (a) and individual trajectories (b)

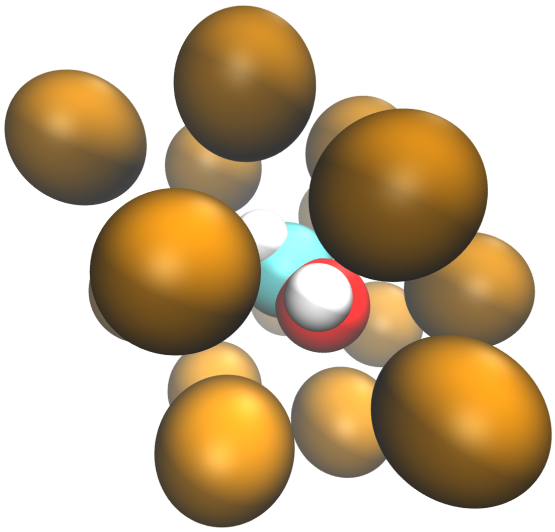

Figure 9.10: cFA site example

9.1.3 *Formic Acid Spectra Conclusions*

For tFA the two identified sites coincide well with the two sites identified by Maçôas et al. [177]. For example, there is the 2 wave number difference in peak positions in agreement between simulations and experiment. The same sites can also be identified from OH overtone vibrational region and they are in agreement with the experiments there as well. Moreover, the triangle state in the simulations has a lower energy than the square state since more argon atoms are close to each other. Thus, we can expect the triangle site to have a larger population, which results in a higher intensity in the spectrum. This is in agreement with experimental data of Maçôas et al. [177].

The experimental data is not in complete agreement here, as Lundell et al. got 3 peaks [178] for the OH stretch, while Maçôas et al. [177] had two and 3rd very small one. The difference of these two is that, in the first study, the deposition was done at 15 K, whereas the latter used 8 K. This could be interpreted that increased deposition temperature causes the 3rd peak to appear. This can be considered to be in agreement with the computed data in this Thesis, which indicate that the third peak is caused by a site that has no specific structure and is affected by thermal energy deforming the site. This could be further verified by doing the calculations at lower energy.

An issue in the calculated spectrum is that the identified site peaks have a broad FWHM, which means that they cannot be identified from the average spectrum as separate peaks. This is partly due to the use of peak fitting to counteract noise in individual trajectories and the question is would calculating more trajectories solve this issue.

Specific cFA sites could not be identified at all. This could result from the previously mentioned issues or by the fact that cFA has a more complicated site structure than tFA. Also, in the experiments cFA is not produced directly by the deposition of gas-phase sample. Instead, it is formed by a selective IR irradiation from tFA. This could result in a completely different site structure where cFA is trapped in a more tight and strenuous site instead of a relaxed site produced in a slow deposition and cooling process.

The study leaves the cFA site structure for further study, which ideally would need more trajectories. Also using lower-temperature simulations should be considered.

Table 9.3: tFA nitrogen complex peaks

	MD	Exp [178]			MD
ν_7	520-580	636.8		$\nu_2 + \nu_6$	4075-4110
ν_9	700-780	679.5		$\nu_1 + \nu_9$ or $\nu_2 + \nu_5$	4250-4350
ν_8 and ν_6	1090-1135	1114.3		$\nu_2 + \nu_3$	4710-4730
ν_5	1275-1285	1226.9		$\nu_1 + \nu_5$	4845-4855
	1310-1325			$\nu_1 + \nu_4$	4950-4965
ν_4	1375-1420			$\nu_1 + \nu_3$	5310-5320
ν_3	1730-1760	1764.9		$2\nu_2$	5950-5980
	2332-2337			$\nu_1 + \nu_2$	6550-6555
	2395-2400			$2\nu_1$	7120-7170
ν_2	2975-2992	2954.5			
ν_1	3563-3586	3531.7			

9.2 FORMIC ACID - NITROGEN COMPLEX

The Formic acid - nitrogen complex was calculated with the same settings as formic acid, so that the results could be compared. The only addition on the previous formic acid (FA) system setup was the inclusion of nitrogen to the quantum mechanics (QM)-calculation and the use of a 0.5 fs time step. The nitrogen-argon potential only used even powers

$$E(r) = \sum_{n=3}^{6} \frac{c_{2n}}{r^{2n}}, \tag{9.1}$$

because it was found during the fitting procedure of the potential that the accuracy did not improve when odd powers where added. A total of 20 trajectories was computed for further analyses. Out of the total 20 one trajectory failed[2] for unknown reasons for both conformers, leaving 19 trajectories for each conformer.

9.2.1 *Trans-Formic Acid - Nitrogen complex IR Spectrum*

The spectrum computed for the FA-N_2 complex is depicted in Figure 9.11 and the computed peak positions are summarized in Table 9.3.

A closer look at the OH-stretching vibration is shown in Figure 9.12. The OH-stretching peak consists of a tall peak Figure 9.13a at the lowest energy. This vibrational band is connected with a FA-N_2 structure in which the N_2-bond axis is on a straight line towards the OH bond. The second peak at around 3568 cm^{-1} reflects a structure where the N_2 molecule is bent out from the FA plane, as shown in Figure 9.13b. There appears also a shoulder band structure, which is caused by

2 Some of the N_2complex trajectories crash and the crash is reproducible for the given initial state. The reason might be that N_2 or FA might wonder to the edge of the simulation box, which could cause Poisson solver to fail, resulting in a crash. The crash mentioned happened in spectrum calculation phase.

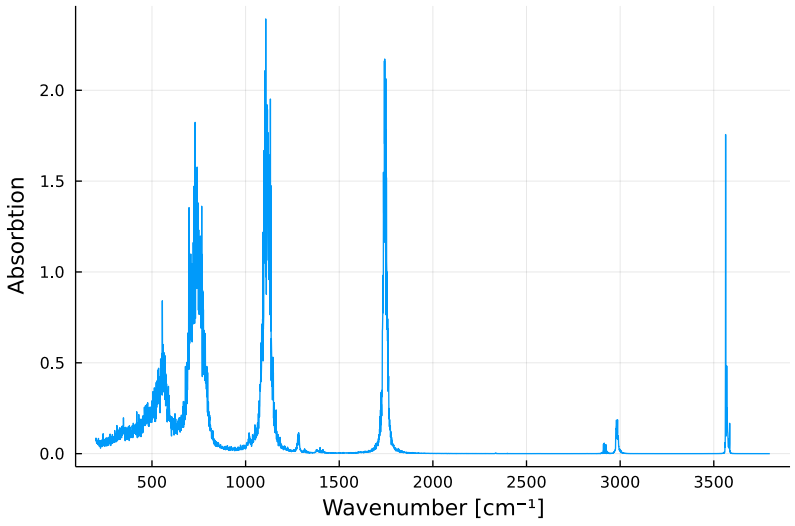

(a)

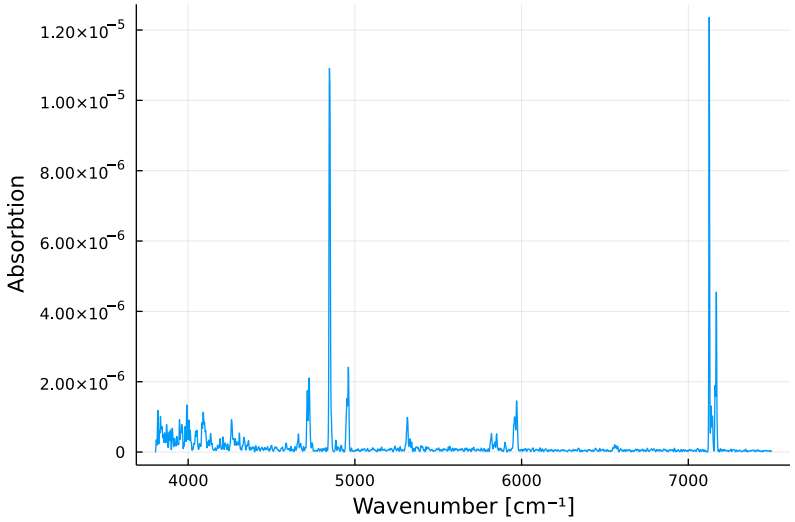

(b)

Figure 9.11: tFA nitrogen complex spectrum, fundamental region (a) and overtone region (b)

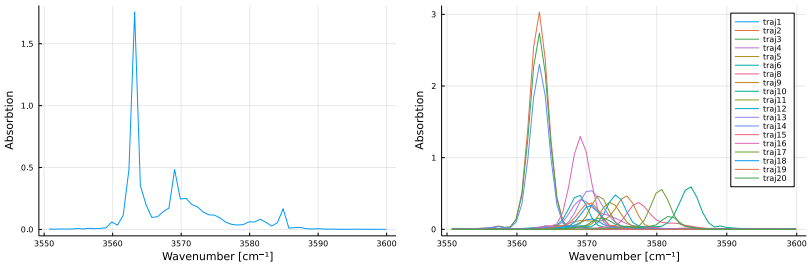

(a) (b)

Figure 9.12: tFA nitrogen complex OH stretch, average (a) and individual trajectories (b).

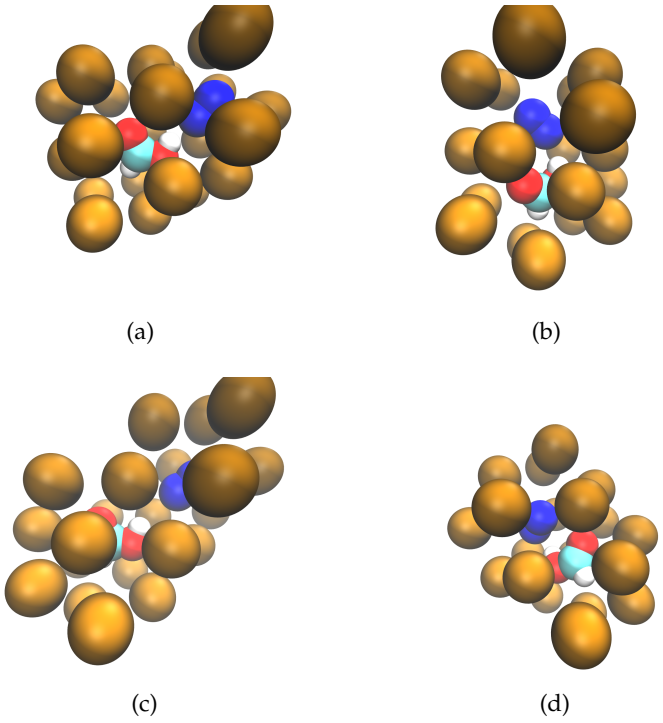

(a) (b)

(c) (d)

Figure 9.13: Trans-formic acid nitrogen complex

structural sites where N_2 is pointing into different directions. An example of such local structure is shown in Figure 9.13c. Finally, there is a site where N_2 is located is a "side to side" position with FA. This site structure contributes to the highest-energy part of the spectral band. The same sites are also shown without Ar atoms in Figure 9.14.

9.2.2 *Cis-Formic Acid - Nitrogen complex IR Spectrum*

The simulated spectrum of cFA-N_2 is shown in Figure 9.15. The vibrational bands appearing are listed in Table 9.4. The OH-stretching vibration in the complexes are depicted in Figure 9.16.

The difference of cis and trans FA conformers is that, in the cis form, the hydrogen atoms are on the same side of the FA molecule, and in tFA the two hydrogens are on the opposite sides of the C-O bond in the molecular plane. Therefore, for cFA, one nitrogen atom from the N_2 molecule can then be between these two hydrogens and the other is either in same molecular plane as cFA Figure 9.17a (lower energy) or out of the plane compared to cFA, Figure 9.17c (higher energy). Also, the simulations reveal a site structure where the N_2 molecule is next to the cFA molecule with both nitrogen atoms outside the plane of cFA but in between hydrogen atoms, see Figure 9.17b. The peak that comes form the latter case is in the middle of the bands connected with the other site structures.

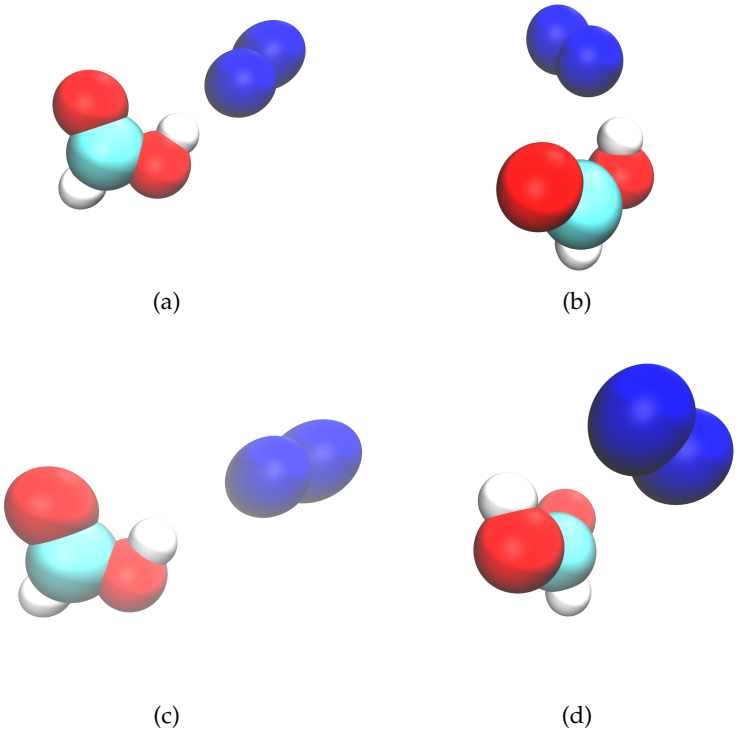

(a) (b)

(c) (d)

Figure 9.14: Trans-formic acid nitrogen complex sites without argon

Table 9.4: Simulated vibrational bands of cFA-N_2

	MD		MD
ν_7 and ν_9	400-600	$\nu_2 + \nu_6$	3955-3970
ν_8	1050-1080	$\nu_1 + \nu_9$	4100-4200
ν_5	1240-1280	$\nu_2 + \nu_3$	4675-4710
ν_4	1380-1390	$\nu_1 + \nu_5$	4870-4910
ν_3	1782-1790	$2\nu_2$	5760-5805
$\nu_5 + \nu_8$	2332-2337	$\nu_1 + \nu_2$	6520-6530
?	2350-2365	$2\nu_1$	7255-7275
$2\nu_4$	2755-2780		
ν_2	2880-2910		
ν_1	3627-3637		

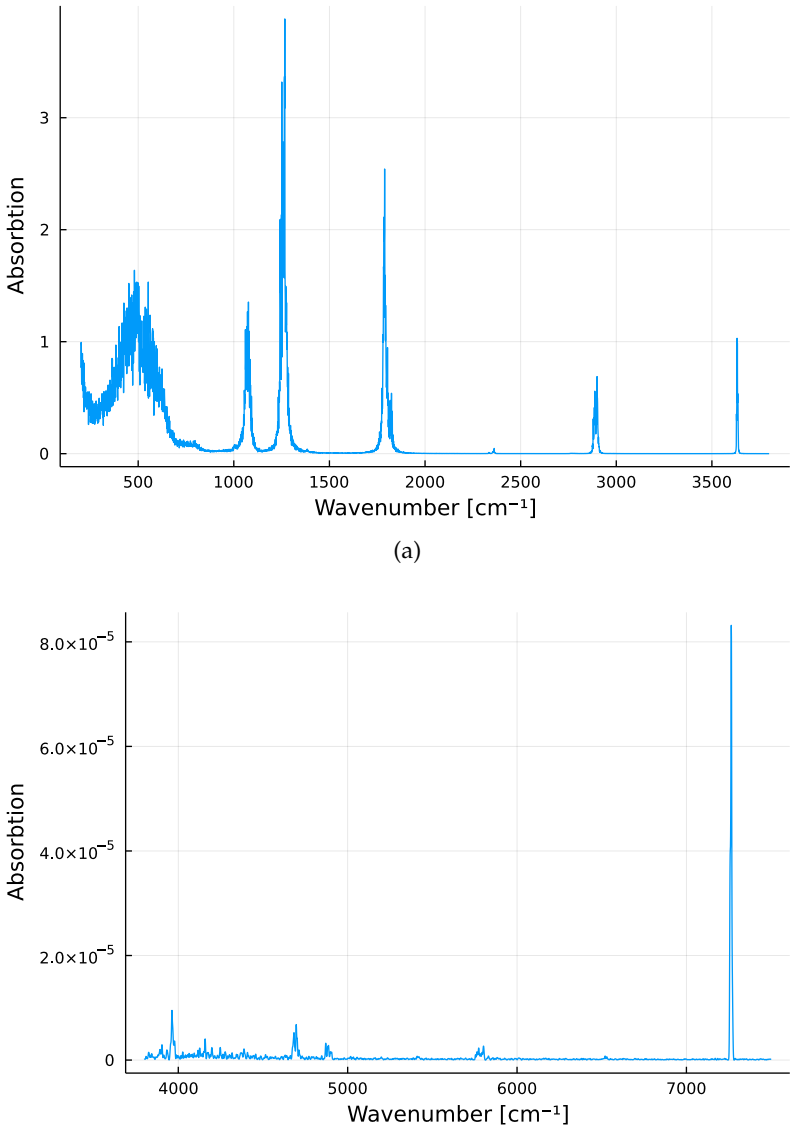

(a)

(b)

Figure 9.15: The simulated IR spectrum of the cis-formic acid nitrogen complex

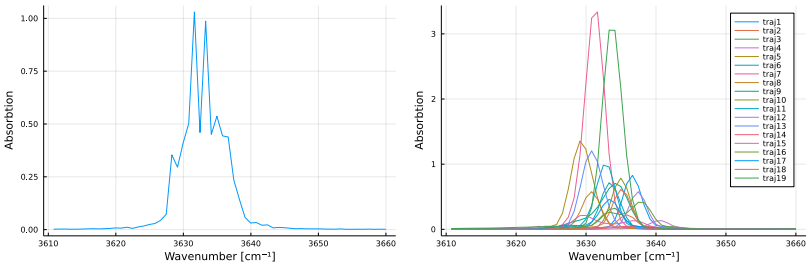

(a) (b)

Figure 9.16: cFA-N_2complex OH streching spectrum, average (a) and individual deconvoluted trajectories (b)

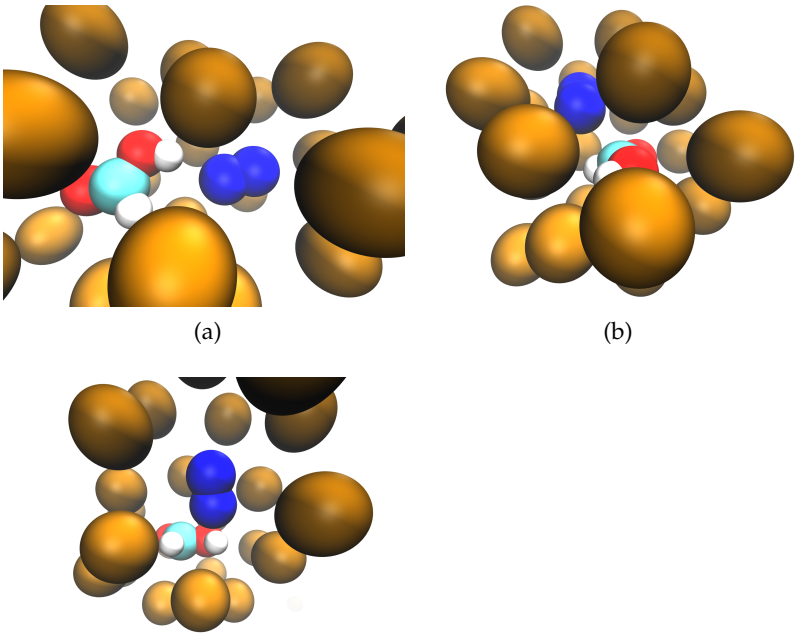

(a) (b)

(c)

Figure 9.17: Cis-formic acid nitrogen complex sites

9.2.3 *Formic Acid Nitrogen Complex Conclusions*

The experimentally observed OH vibration of FA in the FA-N_2 complex consists only of two peaks [178], while the calculated spectrum has 3 peaks. Of these, the two lowest-energy peaks could correspond the experimental band with components at 3531.7 cm^{-1} and 3538.0 cm^{-1}, while the highest-energy part overlaps with the monomer band in the experimental spectrum. There is also a notable similarity in the appearance of the band with the two lowest-energy bands observed in the experimental spectrum.

The experimental study [178] also reports annealing cycles resulting in the depletion of the local higher energy complex structures. Based on the present simulations this could mean that the N_2 molecule is pointing to different directions after annealing, i.e., N_2 is able to rotate or librate upon annealing in the matrix producing multiple structural orientations in the matrix, cage with negligible site-structure energy differences.

For cFA there is a limited experimental data available [179], with the main focus on the C=O stretching vibration. The study mentions two sites where N_2 is in the same plane with cFA interacting either with the OH or CH groups. While the site presented in Figure 9.17a is close to one of the sites proposed in the article, the two other sites appearing in the simulations are not considered by the authors of the article.

The results from the simulations do not fully corroborate the experimental results. The point to note is that the two sites missing are the result of argon atoms taking positions which would yield local

structures lower in energy. Accordingly, the N_2 molecule would end up in more strenuous and tight, higher-energy positions. When the site structures are calculated without the surrounding matrix atoms, this kind of positioning cannot be taken into account. The conclusion is that, in general, the site structures for complexes, when calculated without the surrounding matrix atoms, might not be a fully adequate approach. Thus, it would be recommended to have at least some kind of discussion of matrix atoms affecting the complex structures in the future.

In the matrix community it is well endorsed that at least the first solvation shell is needed to be included as specific atoms, to be able to describe the features of local site structures [180–182].

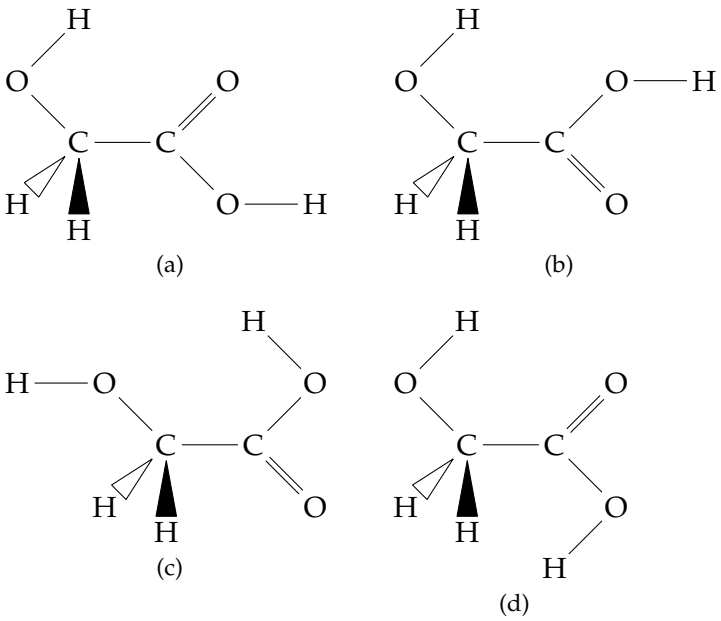

Figure 9.18: Glycolic acid; most stable conformers SSC (a), GAC (b), AAT (c) and SST (d)

9.3 GLYCOLIC ACID

Glycolic acid has been of interest in several recent studies [28, 35–39, 183–188]. The calculations presented here are aimed to give relevant information for these experimental studies. This includes understanding the different sites observed in the experiments, as well as processes induced by IR pumping the first OH-overtone vibration. Especially, the most stable SSC conformer, see Figure 9.18, is of interest since this is the most profound conformer of glycolic acid found in freshly deposited matrix samples. This is also the target conformer used as a precursor for the IR-pumping experiments.

The simulated spectrum for the SSC conformer in solid Ar is presented in Figure 9.19. The simulation temperature of 10 K and total of 20 trajectories were made to generate the simulation data. The peak locations for SSC are listed in Table 9.5. A closer look on the OH-stretching vibrational band (acidic OH) is shown in Figure 9.20. Simulation on the first OH-overtone vibration is shown in Figure 9.21.

Based on the RDFs presented in Figure 9.22, several site structures can be identified. This can also be confirmed by looking at the trajectories themselves. There are the same square and triangle sites that formic acid had, but also additional ones. There, however, were no trajectories with same kind site structure, which made site identification impossible. Thus, we can only conclude that there are several sites that produce peaks that can overlap with each other.

The C=O stretching vibration is shown in Figure 9.23. The peak is not symmetrical and could be considered to consist of two partially overlapping peaks with one higher in energy and having lower intensity. From these two, the lower-energy component does not seem to

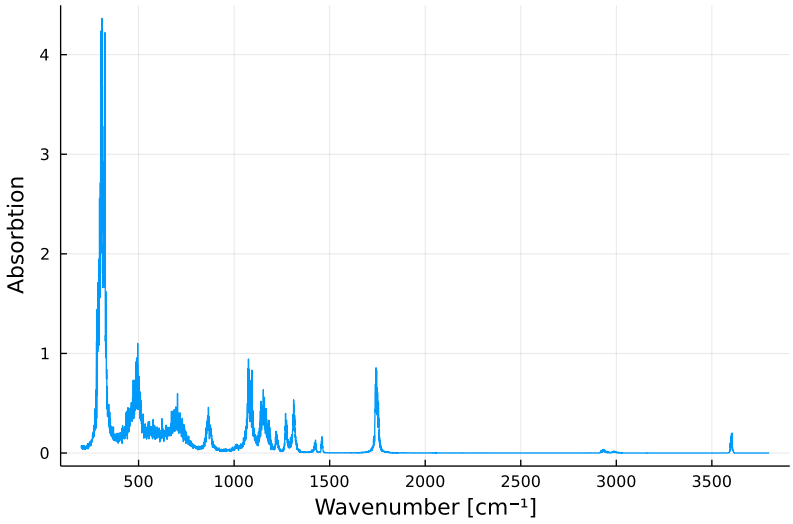

(a)

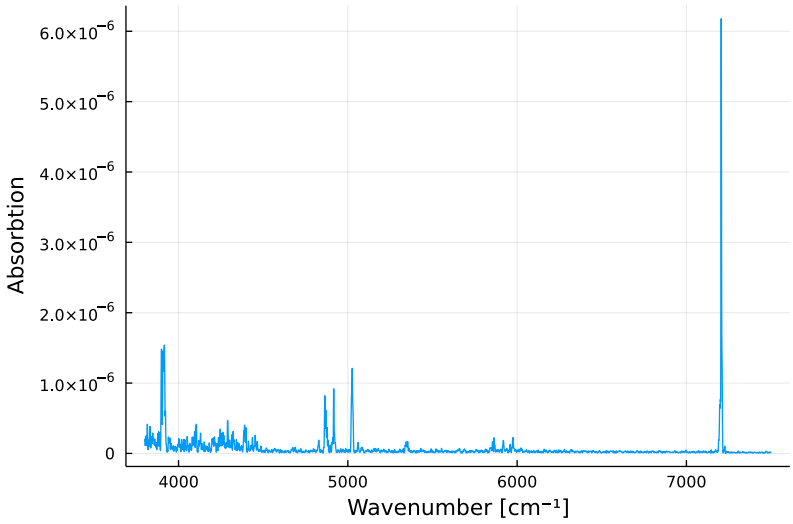

(b)

Figure 9.19: Glycolic acid IR spectrum, fundamental region (a) and overtone region (b)

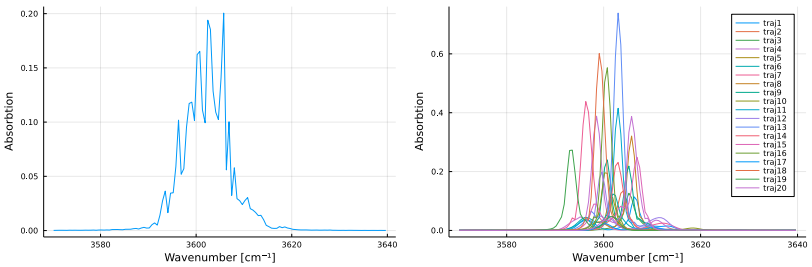

(a) (b)

Figure 9.20: Simulation of glycolic acid OH stretching vibration band

Table 9.5: Simulated glycolic acid (SSC) vibrational peaks

MD	exp [37]		MD	exp [188]
280-330			3780-3925	
450-510	468, 495		4860-4880	
680-720	638		4915-4920	
850-880	854		5020-5035	
1070-1100	1090		5330-5355	
1140-1170	1143		5850-5870	
1215-1230	1231		5910-5980	
1265-1277	1265		7190-7215	6938, 6954
1305-1320	1332			
1420-1430	1439			
1455-1465	1452			
1735-1760	1773			
2920-2950	2929			
2975-3010	2947			
3595-3615	3561			

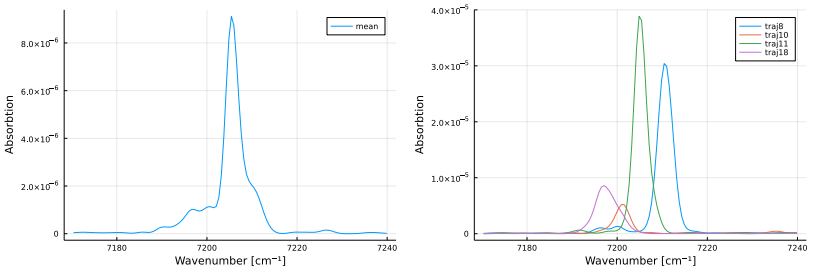

(a) (b)

Figure 9.21: Glycolic acid OH overtone stretching vibration deconvoluted mean (a) and selected trajectories (b)

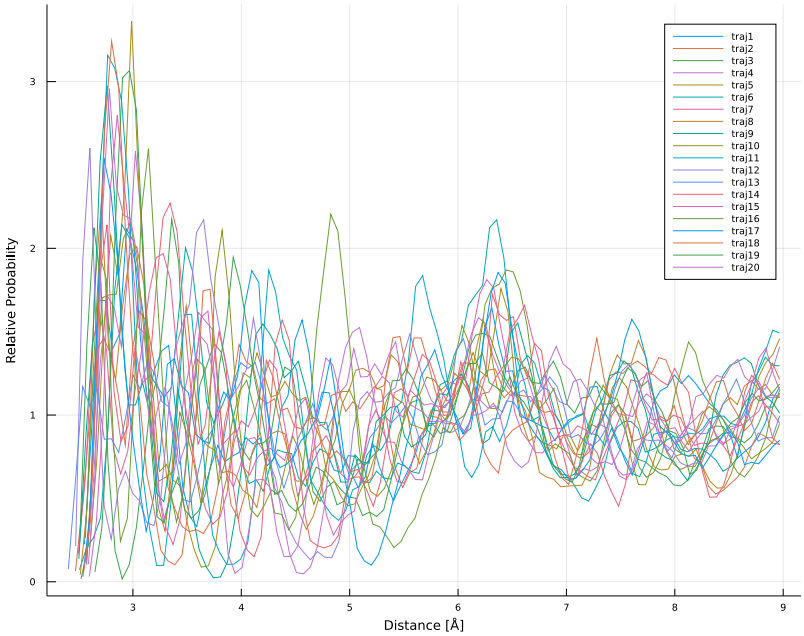

Figure 9.22: Glycolic acid RDF (H_{cooh}-Ar)

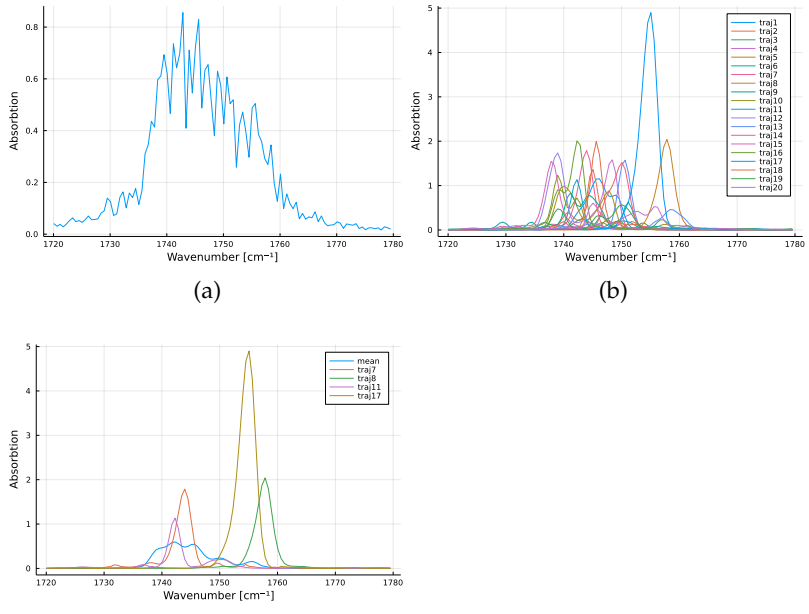

Figure 9.23: Glycolic acid C=O stretching vibration, average (a), deconvoluted trajectories (b) and selected trajectories (c)

have any specific site structure. It has several different sites and one can identify the triangle site, as well as several others (Figure 9.24).

The peak with with the higher energy has a specific site structure as shown in Figure 9.25. The site consists of 5 argon atoms in a plane forming a pentagonal structure around the oxygen, with an argon atom located on the top of the pentagon. This "pentagonal pyramid" structure can be in different directions relative to the C=O bond. The structure in Figure 9.25 has the top of the pyramid on "top of" oxygen, but the pyramid can also be tilted. The defining characters are that the pentagon is in the same plane and all 6 argon atoms are at 3.4-3.5 Å distance from the oxygen. The tilting of the pyramid allows the 7th argon to come close to oxygen, which means that the RDF does not reliably distinguish the site structure.

9.3.1 *Glycolic Acid Conclusions*

Glycolic acid has two OH groups, which create peaks almost on top of each other [185]. This results in a combined single peak in the calculated spectrum. This is probably one reason why it was not possible to identify specific, local structure sites in the OH-band simulations. The other reason might be that there simply are numerous sites, because the OH vibrations are not completely localized and the area that contributes to the peak shift is also broader.

When comparing the peak shape to the experimental spectra [35], we can conclude that for the OH-stretching vibration, the band shape corresponds to the experimental one. The experimental peak is almost symmetrical and has a small bulge next to it on the higher-energy side, which is what we can see from the calculated spectrum (Figure 9.19) as well.

For the C=O-stretching vibration, the experimental peak [35] has one tall peak with a lower-energy shoulder, and a small peak at higher energy. The calculated peak might correspond to this, but with the 20 calculated trajectories it cannot be fully confirmed. The calculated peak does have the pentagonal pyramid site peak at higher energy and there are several sites in the main peak represented. In the experimental spectrum, the two peaks differ about 10 cm^{-1}, which is the same energy difference, as the pentagonal pyramid site peak and main peak have in the calculated spectrum. Also, the pentagonal pyramid site has "pyramid on top" and "tilted pyramid" configurations that have a small energy difference, which could produce the doubly topped peak seen in the experimental spectrum.

Based on these calculations there are several sites that could be targeted with site-selective overtone pumping to the OH-stretching overtone. The calculations indicate that the region could have 3 sites, one at the top peak, one at the shoulder peak at lower energy and one at the higher-energy shoulder. Nevertheless, it is very difficult to identify the defining structure of these sites. It is likely that some kind of machine learning needs to used and more trajectories to be

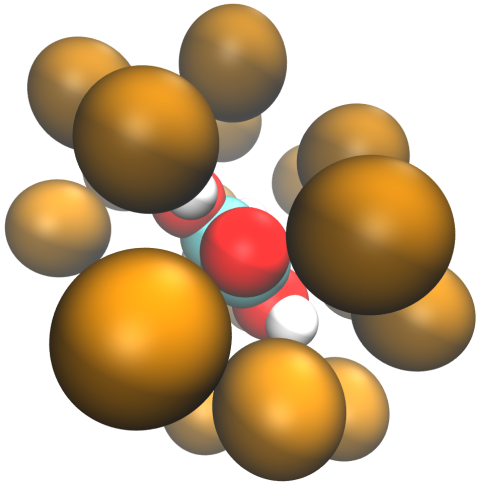

(a)

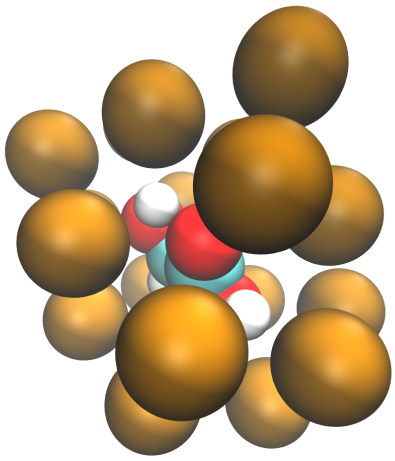

(b)

Figure 9.24: Glycolic acid sites for carbonyl oxygen, triangle (a) and a random site (b)

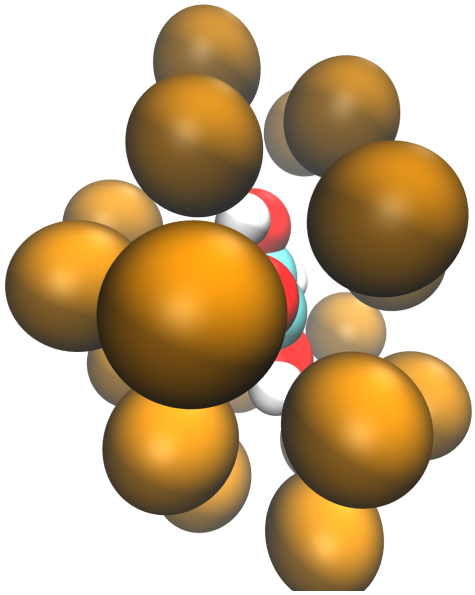

Figure 9.25: Glycolic acid pentagonal pyramidal site

generated in order to classify the sites more carefully. Also, there is a lot of noise in the calculated spectra, which affects the accuracy.

It is possible that the two experimental peaks reported by Halasa et al. [188] at 6938 cm^{-1} and 6958 cm^{-1} are within the computed band structure between 7190 cm^{-1} and 7215 cm^{-1}. The shape of the band supports this, as the higher-energy part of the band has higher intensity similar to the experiments where the higher-energy peak is observed to be much more intense.

Furthermore, the correspondence between the simulated and experimental spectra suggest that MI simulations are able to address the vibrational overtone modes. Based on the discrepancy of the band positions in simulations, it is possible that there are deficiencies in the PES used for the higher wavenumber modes, whereas in the fundamental region, the PES is better described. However, the same kind discrepancies also exist for FA and it is more likely that the used functional, BLYP, is the cause of the discrepancy.

9.4 BENZENE

The story why the spectrum of benzene ended up in the Thesis deserves to be told. It began in early spring in 2018, when Dr. Leonid Khriachtchev suddenly and unexpectedly passed away. Dr. Khriachtchev was a respected and well-known researcher of molecular spectroscopy, nanomaterials and low-temperature matrix isolation field [189].

In 2018, Dr. Khriachtchev studied the spectroscopy of benzene in low-temperature noble gas matrices. The CH-stretch mode of benzene has a Fermi resonance with two other peaks forming a triplet, Figure 9.26. In the fine structure of these peaks he observed features that he suspected could indicate rotational motion of benzene in the matrix. Some calculations had to be done to prove it. However, Dr. Khriachtchev passed away before the calculations were finished. Since Dr. Khriachtchev had asked professor Dage Sundholm whether he could perform the calculations, Prof. Sundholm wanted us to finish the calculations and publish them in the memory of Dr. Leonid Khriachtchev.

The preliminary calculations were performed by Maria Dimitrova, who was then doctoral student in the research group of Prof. Sundholm. These calculations were addressing the rotational energy levels of benzene embedded in a static noble-gas matrix. At the ICQC conference in Menton in summer 2018, I discussed the calculations with Maria Dimitrova, whom I already knew from domestic scientific meetings. I told her that I have recently begun to consider matrix effects by using MD simulations. I discussed the project with my supervisor professor Jan Lundell and we decided to perform MD calculations on benzene in noble gas matrices.

It soon became clear that the responsibility for the calculations rested on my shoulders. I also wanted to finish this project in honor of Dr. Leonid Khriachtchev. While the calculations are technically easy to perform, the results are indeed difficult to interpret. It is a notoriously difficult task to determine the motion of the vibration modes of benzene and, even after decades of work, there is still some controversy about it [190]. We needed more experimental data to interpret the benzene spectrum. Docent Markus Metsälä promised to help and looked for the original data through Dr. Khriachtchev laboratory notebooks. To our surprise, the original spectra was recorded in the spring of 2012, but Dr. Khriachtchev had come back to the interpretation in early 2018. This is when we took the challenge of trying to understand the spectroscopy of benzene embedded in noble gas matrices combining the experimental and computational efforts together.

9.4.1 *Experimental Spectra*

The spectrum of benzene in neon matrix is shown in Figure 9.26a. In the experiment, the deposition and recording of the IR spectrum

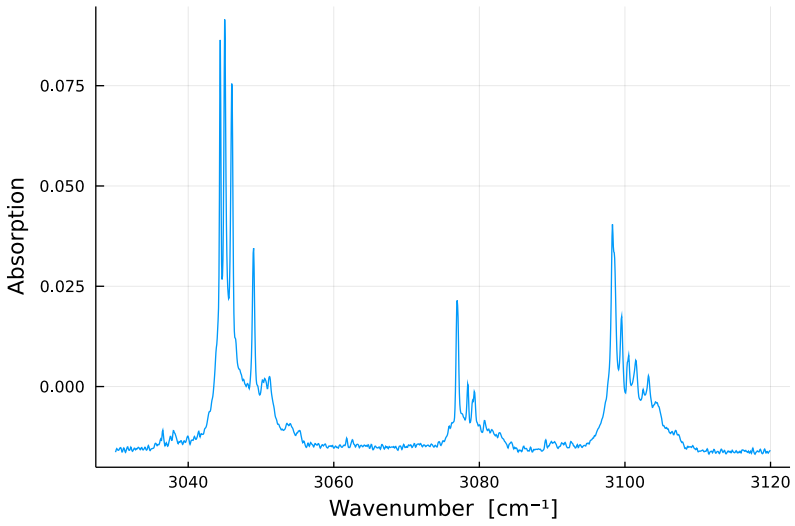

(a)

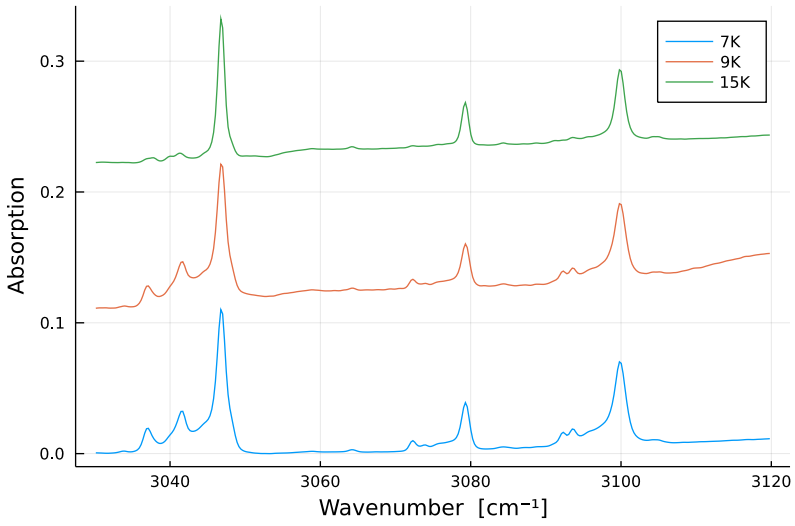

(b)

Figure 9.26: The Fermi triplet experimental IR spectra of benzene [157]. Ne matrix (a) and Ar matrix (b).

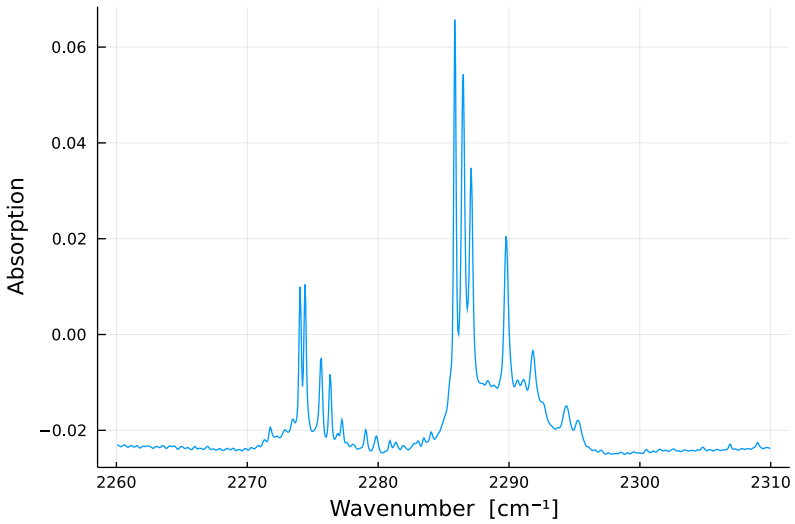

Figure 9.27: Deuterated benzene in a Ne matrix [157] experimental spectrum.

were done at the temperature of 8 K using a matrix ratio of 1 : 2000. Deuterated benzene were prepared and measured in the same way Figure 9.27.

The spectrum of benzene in an argon matrix is shown in Figure 9.26b. The matrix ration of Benzene:Ar was 1:2000 similarly to the neon matrix. The first samples were prepared and measured at the temperature of 7 K. Additionally, other samples with increased matrix ratio of 1:4000 were prepared both at 9 K and 15 K. The IR spectra were recorded for these samples at the same temperatures. For the sample prepared at 15 K, a subsequent annealing cycle was performed where the matrix was warmed up to 30 K for 5 minutes before recooling the sample back to 15 K for recording the IR spectrum.

9.4.2 *Calculated Spectra*

The spectra of benzene embedded both in neon (shown in Figure 9.28) and argon were computed with MD simulations. The theoretical calculations were performed at the temperatures of 5 K and 10 K for argon and at 5 K for neon. A total of 20 trajectories were run for each case.

The CH-stretching vibration region of benzene spectrum is depicted in Figure 9.29, which only exhibits one peak. Interestingly, the vibrational overtone mode of the CH-stretch (Figure 9.30) consists of three separate, individual peaks.

In a more closer look, the 5 K spectrum has small peaks at 3103 cm^{-1} and 3140 cm^{-1} that could be the missing peaks, which are expected to be present based on experimental spectrum. Peak locations wary depending on temperature. In fundamental region, (Figure 9.29) peaks have $5 - 10\,cm^{-1}$ difference in the positions and in the overtone region (Figure 9.30) the difference is around 20 cm^{-1}, with higher temperature having lower energy.

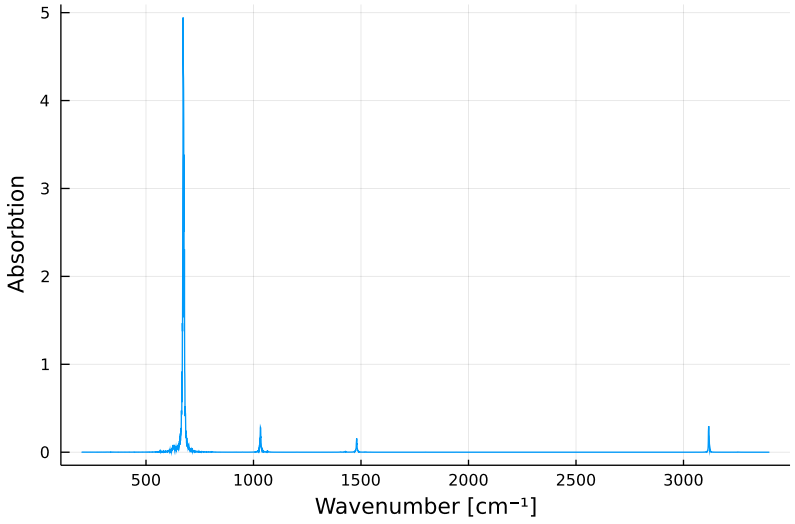

(a)

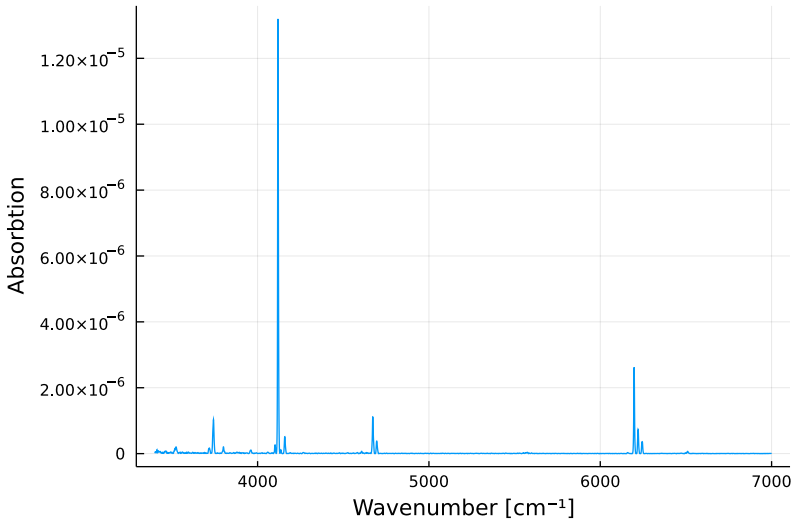

(b)

Figure 9.28: Calculated IR spectrum for benzene in a neon matrix, (a) fundamental region and (b) overtones.

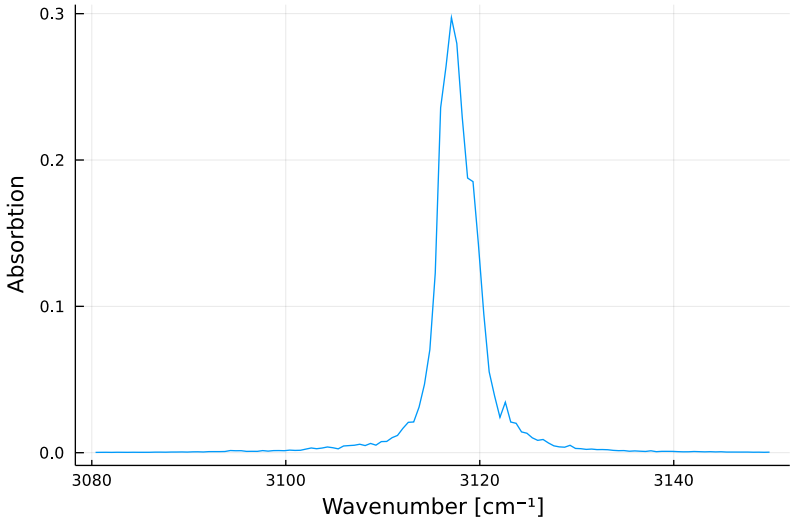

(a)

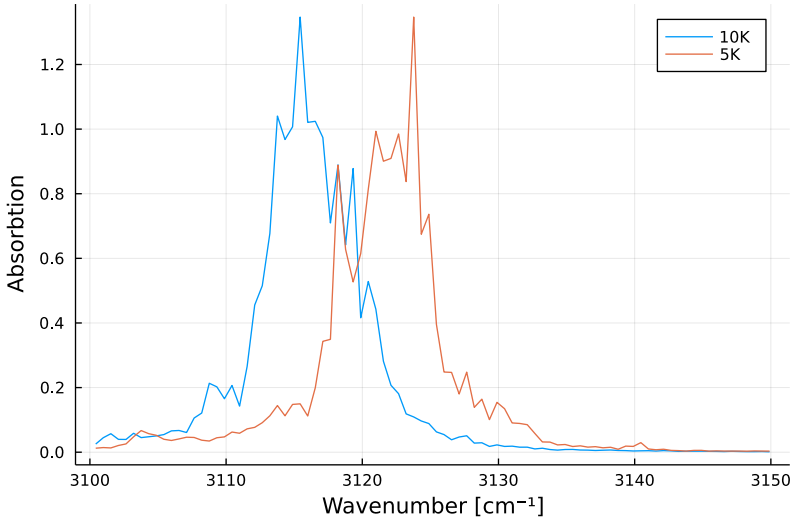

(b)

Figure 9.29: Computed benzene CH-stretching mode in neon matrix (a) and argon matrix (b).

There are also other peaks than the mentioned 3103 cm^{-1} and 3140 cm^{-1} peaks that only appear in certain temperature, e.g., around 3250 cm^{-1} in 5 K spectrum appears an extra peak that is not in 10 K spectra (**??**). This peak is also present in 5 K neon matrix spectrum. In general, 5 K argon and 5 K neon matrix spectra look more similar than 5 K and 10 K argon matrix spectra. However, the similarity is not complete, e.g., the mentioned 3103 cm^{-1} and 3140 cm^{-1} peaks are only visible in 5 K argon matrix.

Trajectories from the MD reveal that there is a large variation between them Figure 9.32a. Looking closely, there are (at least) two separable groups (see Figure 9.32b) of trajectories to be identified.

For benzene in the neon matrix, the defining site-structure feature is the neon atom located centrally above the benzene molecular ring. This Ne atom is surrounded by 6 other neon atoms in the same plane as the central Ne-atom (see Figure 9.33a). The site with the Ne-atom

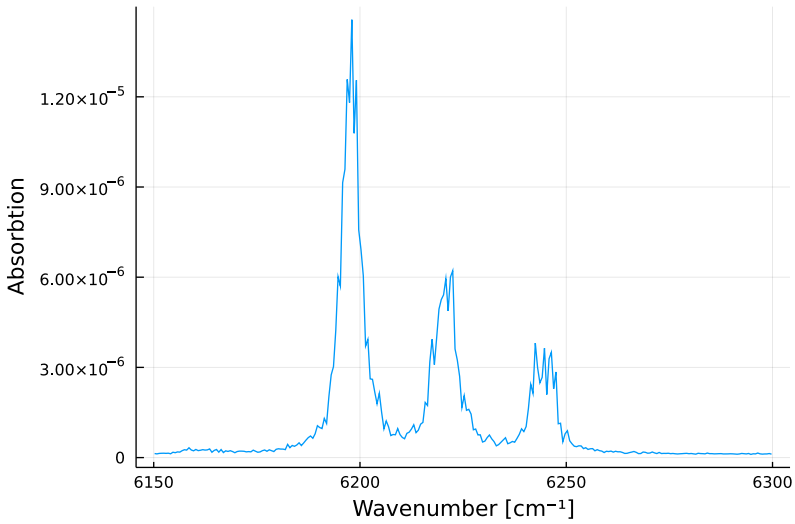

(a)

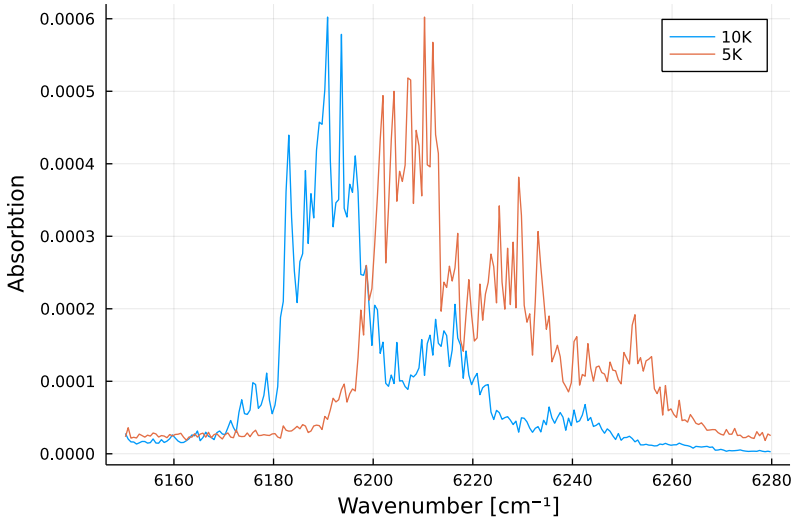

(b)

Figure 9.30: Benzene CH-vibrational overtone mode calculated in a neon matrix (a) and in a argon matrix (b).

in the center forms beautiful hexagonal shapes with other neon atoms around the central Ne. This happens, however, only on one side of the benzene molecular ring. The other side has a more random structure (e.g., see Figure 9.33b).

Analysis of the individual trajectories related to vibrational overtone peaks reveals that all trajectories contain three peak components. This indicates that they are true vibrational peaks and not separate sites. Also, the trajectories are ordered according to if one trajectory has a lower energy than the peaks relative to other trajectories. This same ordering of trajectories holds also for other peaks (see Figure 9.34), as well.

The MD simulations reveal that, for benzene in an argon matrix, a wide variety of sites are found. In fact, the selection is much more diverse than in the case of the neon matrix. It was impossible to identify a pair of trajectories that would result in a peak precisely at the

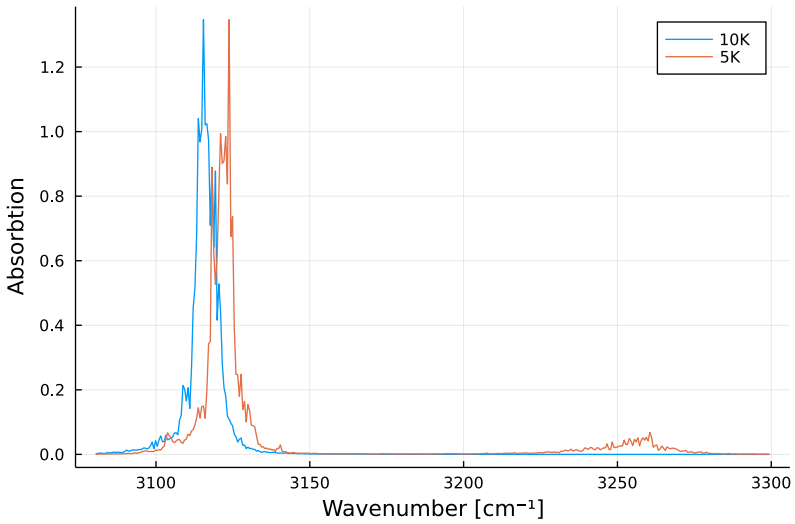

Figure 9.31: Temperature dependence of the calculated benzene spectra in an argon matrix.

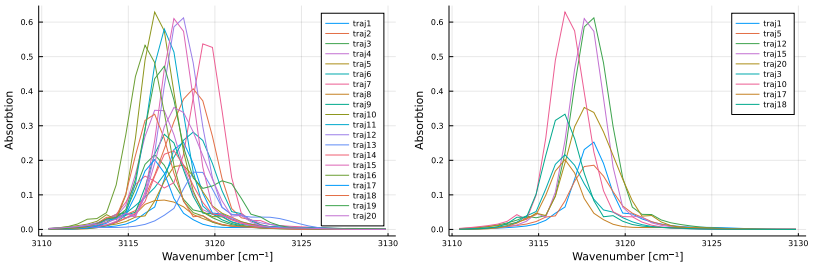

(a) (b)

Figure 9.32: Calculated deconvoluted trajectories for benzene in a Ne matrix: All trajectories (a) and a selected set that shows two subgroups (b).

same position in the spectrum. That being said, the same hexagonal site shape that was observed in the neon matrix, is seen in several trajectories (see Figure 9.35). Also a double-sided hexagonal structure is found. The double-sided structure corresponds to the lowest-energy peak that is identified and correlated with the small shoulder peak at wavenumbers lower than the main peak. One-sided structure with the hexagonal structure only on one side of the benzene molecular plane is seen appearing towards higher wavenumbers. Finally, the highest wavenumber peak correlates to structures without any distinct argon atoms.

9.4.3 *Interpretation of Spectra*

The general status of the identification of benzene spectral bands has a long history and is still under investigation [190]. This is seen in different identifications of the three main bands seen in the 3040 cm^{-1}

to 3100 cm^{-1} region in the IR spectra. There is Herzberg's assignment [191] $\nu_{13} + \nu_{16}$, $\nu_2 + \nu_{13} + \nu_{18}$ and ν_{13} from the lowest to the highest. Then there is Brodersen and Langseth's assignment where the order is reversed [191]. Finally, some other sources [192] have ν_{20}, $\nu_1 + \nu_6 + \nu_{19}$ and $\nu_8 + \nu_{19}$. Common to all the sources is that all the bands are assigned with the E_{1u} symmetry and that there is a complicated Fermi resonance present.

In order to avoid a long discussion of the details of the assignment, the following discussion speaks in general terms like C-H or C-C stretching and H-C-C bending and the main focus is on the site structure and in explaining why there are such enormous difficulties to calculate the spectrum.

Referring to the character Table 2.1 reveals that benzene has IR-active vibrations of either E_{1u} or A_{2u} symmetry. The CH-stretching mode (ν_{CH}) is has the E_{1u} symmetry. In addition, there are CC-stretching (ν_{CC} also E_{1u}) at $\sim$ 1500 cm^{-1} and HCC-bending (δ_{HCC} - E_{1u}) around 1050 cm^{-1} [190, 191, 193]. These modes are coupled by Fermi resonance with each other and the triple peak (also called as Fermi triad) is observed, as shown in Figure 9.26.

Further complication for explaining the spectrum of benzene arises from the fact that E_{1u} is doubly degenerate. This means that there are two states from ν_{CH}, three from ν_{CC} and four from δ_{HCC}. Thus the three peaks are linear combinations of total of 8 states. Due to anharmonicity the degeneracies of ν_{CC} and δ_{HCC} are also broken, which means that the Fermi triad peaks are further split by a (very) small amount and we could possibly see this in the fine structure of the peaks.

The Fermi resonances present are 2:1 for ν_{CC}:ν_{CH}, 3:1 for δ_{HCC}:ν_{CH} and 3:2 for δ_{HCC}:ν_{CC}. From these resonance VPT2 can only calculate the ν_{CC}:ν_{CH} resonance. Standard VCI (that, e.g., Molpro has) can calculate ν_{CC}:ν_{CH} and δ_{HCC}:ν_{CH} resonances, because it is in practice VCISDTQ. To calculate the δ_{HCC}:ν_{CC} resonance, nonlinear quintuple excitations need to be taken into account. This means that a specific calculated PES needs to be generated to allow such calculations. On top of this, there is the symmetry, which the program has to also understand or there will be small energy split that results from symmetry breaking. There are no generally available programs that can fulfill all these requirements.

For deuterated benzene, the effective masses of ν_{CH} and δ_{HCC} oscillators change, while ν_{CC} stays the same. This means that there is only Fermi doublet, as seen in Figure 9.27. This is an experimental proof that the three peaks are a result of Fermi resonance.

Based on the MD simulations, only one peak is observed instead of a triplet (see Figure 9.29) for the CH-stretching mode, in 10 K spectrum. This indicates that MD does not take into account Fermi resonances and that what is in the simulated spectrum is only the pure fundamental CH vibrational mode.

In 5 K spectrum the two peaks at 3103 cm^{-1} and 3140 cm^{-1} would complete the expected Fermi triad structure. In the experimental spectra, the two outmost peaks are are separate by about 45 cm^{-1},

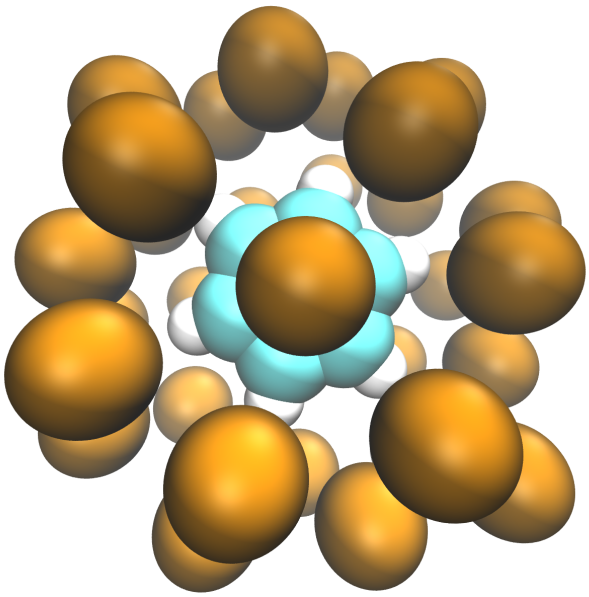

(a)

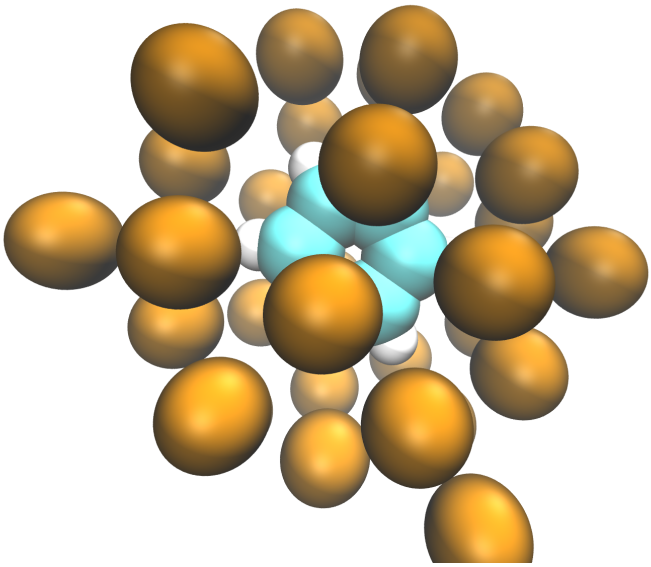

(b)

Figure 9.33: Example sites of benzene in a neon matrix

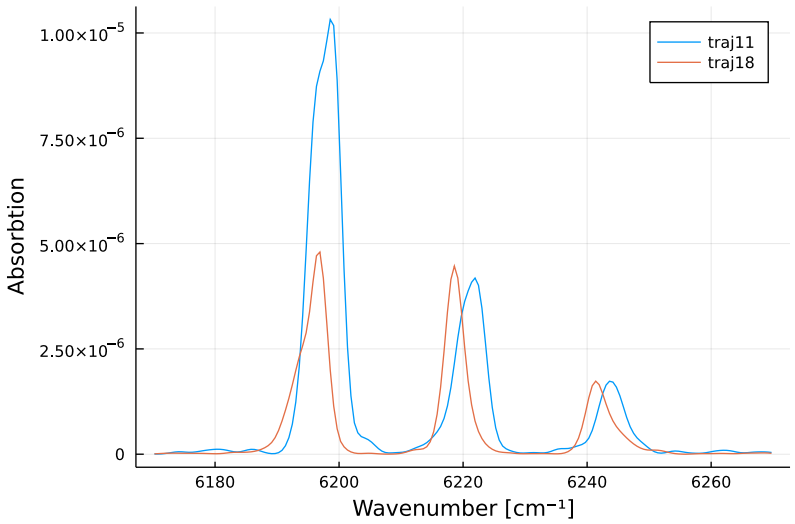

Figure 9.34: Ordering with trajectories in the overtone region of benzene in a neon matrix.

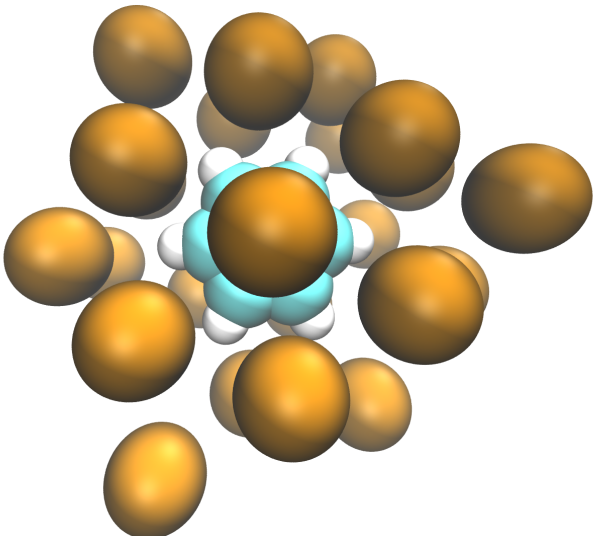

Figure 9.35: Hexagonal site of benzene in an argon matrix.

which corresponds to the 47 cm^{-1} separation in the calculated spectrum. There is, however, no notable intensity increase, which is the hallmark of Fermi resonance. This, most likely, means that the 3103 cm^{-1} and 3140 cm^{-1} peaks are combination peaks that are not in Fermi resonance with the main peak.

The three peaks in overtone region (Figure 9.30b) appear to be similar in intensity. The energies (5 K) of these peaks coincide with the combinations of the three peaks at 3103 cm^{-1}, 3125 cm^{-1} and 3140 cm^{-1} (denoted ν_1, ν_2 and ν_3 now on). The assignment would therefore be $2\nu_1$, $\nu_1 + \nu_2$ and $\nu_1 + \nu_3$. This assignment is problematic since there is no $2\nu_2$ peak, which we would expect to appear around 6250 cm^{-1} that would coincide with the highest energy peak. This would then leave the assignment of the two lower energy peaks unknown. If the $2\nu_2$ peak is the middle peak, then its energy is about 20 cm^{-1} less than two times the fundamental (3125 cm^{-1}). The other peaks would then have assignment of $\nu_1 + \nu_2$ and $\nu_2 + \nu_3$. In this case there would be notable anharmonicity present.

There is also an issue with the band intensities of the peaks. Based on the spectra of other molecules, the spectra only has combinations of two fundamental modes. No combinations of three peaks were observed. The ν_1 and ν_2 peaks are not fundamental. This would mean that peaks like $\nu_1 + \nu_2$ are combinations of three different fundamentals or a fundamental and an overtone. The intensity of this kind of peaks would be very low. This means there must be intensity exchange between the peaks, which would indicate that there is a Fermi resonance between the peaks. In this case the assignment is also unknown due to complicated interaction between the states.

This leaves the question, why only overtone vibration of ν_{CH} has Fermi resonance and not the fundamental? From literature we know that MD can model Fermi resonance in CO_2 [194], when employing CP2K with similar computational settings. The difference here is that, in the example with CO2, the Fermi resonance is of the type 2:1, while in benzene it is much more complex. Thus, it could be possible that using the BLYP functional the modes are not completely aligned for Fermi resonance and using some other functional it could be addressed. This is supported by the fact that 5 K and 10 K spectra have some differences in peaks, i.e., 3250 cm^{-1} is only present in 5 K spectrum. This 3250 cm^{-1} peak is not observed in the experimental spectrum, so it is an unexpected effect of temperature to MD spectrum.

On the other hand, this raises some questions on the reliability of the functional, if temperature has a large effect on the appearance of the peaks in the spectrum. It might be a good idea to explore this more in the future.

9.4.3.1 *Argon Matrix*

For argon matrix the calculations suggest that the lowest-wavenumber bands are composed of the double-sided hexagonal structure in the argon lattice. Energetically thereafter is one-sided hexagonal structure, and finally the higher wavenumber structure is not composed of any

distinct hexagonal local site structures. Pure argon crystal structure is face-centered cubic (fcc), which contributes to the hexagonal forms. Thus, if a site has hexagonal structure on one side of the benzene, then the argon atoms on that side can be considered to be composed of a fcc structure, while a local site without hexagonal structure is locally amorphous.

This interpretation means that the site that has the hexagonal shape on both sides is in a broader view, a fcc argon lattice that has a benzene molecule embedded within one layer of argon atoms. The one-sided structure is a benzene molecule on a fcc surface that has a pile of amorphous argon on top of it. Additionally, there is the locally amorphous site.

In the experiments, the two lowest-energy peaks disappeared when the system was heated at 30 K for 5 min and thereafter cooled back down to 5 K. If we take that the two lowest peaks correspond to sites connected with local fcc structure, this means that heating destroys the local crystal structure and forms a local amorphous structure upon the annealing and cooling cycle.

The three experimental peaks span an area of around 10 cm^{-1} Figure 9.26b, which is the same spectral range found for the calculated peaks (see Figure 9.29b). The issue is that the calculated spectra do not have as good resolution as the experiments. As a result there is no separation to different-site bands in the simulation.

An other possible issue is that the total number of trajectories is small, only 20 and, as such, there is only one trajectory that has the double-sided structure. To have a better confirmation more trajectories would need to be calculated.

9.4.3.2 *Neon Matrix*

In calculations the same hexagonal structure appears as found in the argon matrix (see Figure 9.33a). However, there are differences between the Ar and Ne cases. The Lennard-Jones potential minimum for neon is 2.7 Å, while for argon it is 3.4 Å. This means that the hexagon has a better fit within argon than in neon. With argon the surrounding argon atoms are further away and seem to fit nicely between benzene's hydrogen atoms (see Figure 9.35). For the neon matrix the neon atoms surrounding the center atom partially stand on top of benzene hydrogens (see Figure 9.33a). The neon matrix data had only a few trajectories with hexagonal structure on one side of the benzene molecular plane, while for argon there were several trajectories representing structure. Based on this it can be concluded that benzene does not fit as well to the neon fcc structure as to the argon fcc structure.

For the vibrational overtone peaks the calculations suggest that there is an ordering between the different sites. If one local site has a higher energy on one peak, it would have higher energy on the other spectral components (peaks) as well. From the experimental spectrum Figure 9.26a we can calculate that there are 7 to 8 subpeaks within every peak, depending on how the shoulder peaks are accounted for.

The experimental peaks span an area of about 10 cm^{-1} , which is about the same as the area that the computational peaks span. Therefore, it could be argued that the computational peaks just have a poor resolution and that they merge together because of this. There is definitely enough variation between the trajectories that the computational spectra could include all the sites that the experimental spectra has evidence for. Nevertheless, identification of local site structures is very difficult and the number of trajectories used here is unfortunately small, which are main reasons why the site structures cannot be fully solved for the neon matrix spectra.

9.4.3.3 *Does Benzene Rotate*

To solve the question of whether or not benzene rotates in the matrix, the rotation potential was calculated. This was achieved by taking one frame from the trajectory which was used for spectrum calculation and rotating benzene on the spot. The positions of matrix atoms was frozen on place and only benzene was rotated. With the use of the rotation potential, rotational states where also solved to, using finite difference method [127].

The rotation potential does depend on the local site structure, but the general trend is that, for neon matrix, the potential is 120 cm^{-1} to 400 cm^{-1} wavenumbers deep and, for argon matrix, it is 300 cm^{-1} to 1200 cm^{-1} deep, Figure 9.36.

For benzene to rotate, a quantum state needs to span over all angles. This happens only when the energy is equal to or higher than the potential wall height for the rotational motion. Thus, for the neon matrix the first rotating states appear around 120 cm^{-1} in energy and for argon matrix around 300 cm^{-1}. These numbers are considerably higher than the few-wavenumber differences in peak positions seen in the spectrum (see Figure 9.26a). Based on these calculations, benzene does not rotate in the low-temperature matrices addressed here. If the potential would be around 10 cm^{-1} to 50 cm^{-1}, the rotation could be likely, but now even the weakest neon potential is several times larger than observed energy scale.

In fact, the libration excitations within the rotation potential seem to be tens of wavenumbers in size, so even then could produce peaks that are much further separated than the few wavenumbers we observe in the experimental spectra.

Based on the MD simulations presented here, the local site structures appear quite tight and encompassing around the benzene molecule. This leads to a conclusion that benzene does not exhibit either rotation or libration in Ne and Ar matrices.

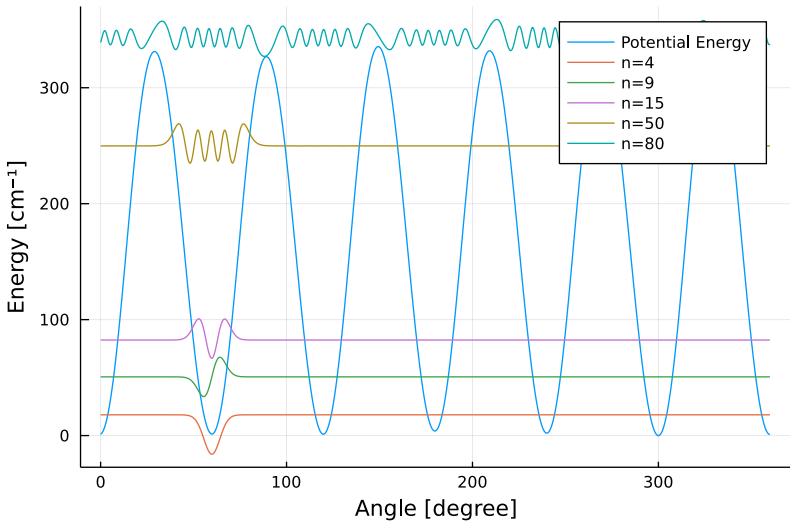

(a)

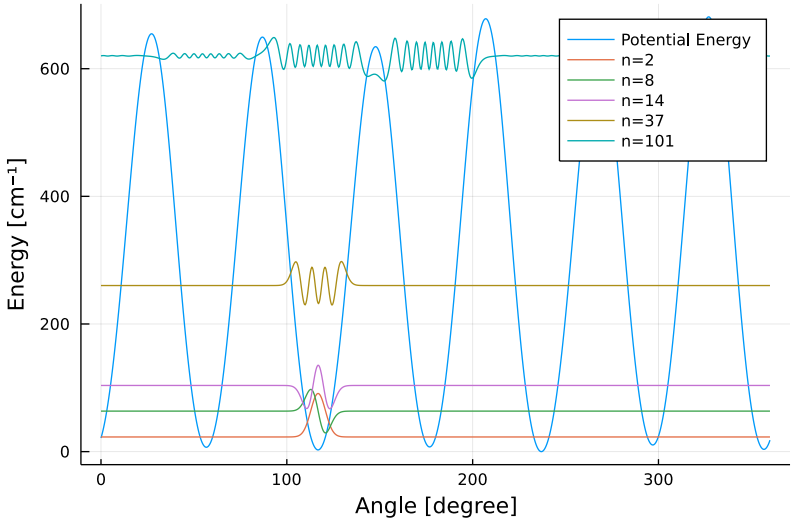

(b)

Figure 9.36: An example of benzene rotation potential and some quantum states for neon (a) and argon (b) matrices.

9.5 CONCLUSIONS ON SPECTROSCOPY

9.5.1 *Site Structure*

The calculated spectra provide significant insight to the local site structures for all studied molecules. There are also some trends that can be identified from the data, such as triangle and square sites encompassing the carboxylic acid's OH-tail hydrogen. For tFA this results to two main sites. For the other molecules the site structure was not completely resolved, such as benzene in Ne matrix. The data does indicate that there is a large variation for different sites.

The main issue with site identification is that it is very difficult to do unequivocally. For FA, RDF was enough to identify sites, but for the other molecules this was not working. The other issue is that there can be a large number of sites which are merged together in the resulting spectrum and a large number of trajectories is needed to identify the individual sites. This leads to increased complexity in identifying the sites. To solve this, it might be a good idea to develop a sophisticated machine learning method to automatize identification and to be able to do the identification in the first place.

Describing a site structure is somewhat challenging and needs to be done with 3D pictures. To help to describe them, it is suggested to follow a graph-based approach

- Matrix atoms are located in vertices
- If two matrix atoms touch each other they are connected with a line
- Only matrix atoms that the closest to the molecule are drawn
- Individual atoms of the molecule are marked with symbols on the graph to mark their location on the "surface" formed from matrix atoms

In Figure 9.37a is the tFA square site illuminated in Figure 9.6a and in Figure 9.37b is triangle site (Figure 9.6b). The cFA site example given in Figure 9.10 is in Figure 9.37c. Additionally, any movement that happens within the site can be described by adding an arrow to point the direction where the movement happens. This way it is possible to easily draw and discuss even complicated site structures and changes that happen in them.

9.5.2 *Accuracy of the Spectra*

The position of the calculated peaks is off compared with the experimental ones, as was to be expected due to the use of DFT. Temperature also has a significant effect on the position of peaks and appearance of combination and Fermi resonance peaks. Together these mean that the accuracy of peak positions is always up to some scaling factor.

To understand the root of temperature dependence of MD spectra, it is necessary to understand how classical anharmonic oscillator behaves

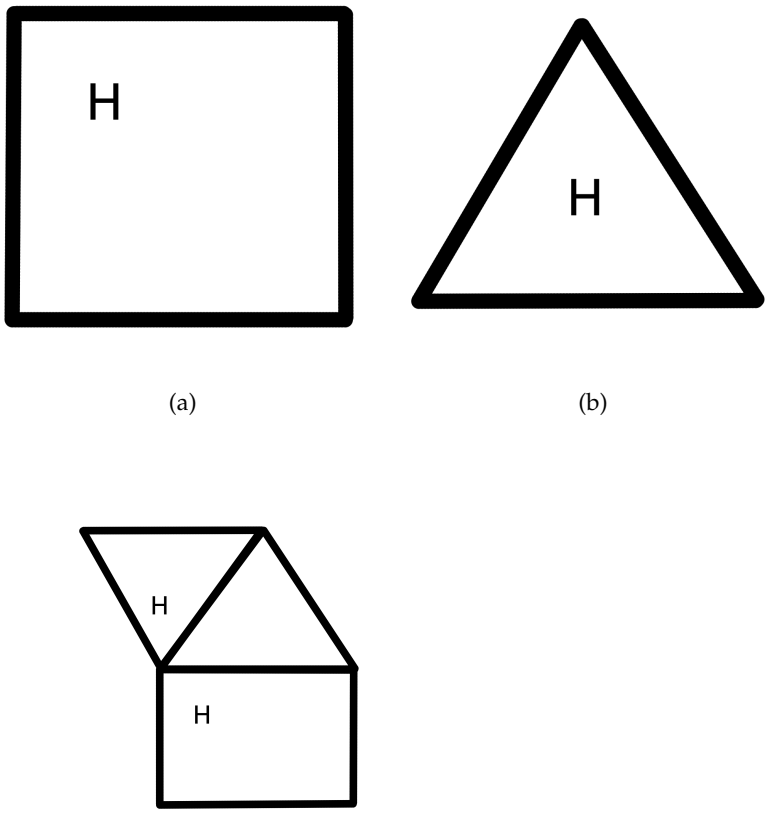

(a) (b)

(c)

Figure 9.37: Site diagrams for tFA square (a) and triangle site (b). In (c) is a cFA site example.

[195]. The resonance frequency of harmonic oscillator does not depend on the energy. This changes in the anharmonic case. The resonance frequency depends on the energy of the oscillator. For a Morse type potential potential the the resonance frequency is the highest at the bottom of the well. When energy increases the resonance frequency gets lower and approaches zero when energy approaches dissociation energy.

The average energy of a singe mode in MD depends on the thermal energy by equipartition theorem ($E_{average} = k_B T$). Lower temperature means lower energy. Higher temperature means higher energy and thus also lower resonance frequency. This can be seen in benzene argon matrix spectra (Figure 9.29b and Figure 9.30b), where 5 K spectra peaks have higher energy than corresponding peaks in 10 K spectra.

For the quantum oscillator the transition energy is the energy difference between the initial and final states. In classical oscillator the transition energy is the resonance energy of the oscillator at its initial energy level. This means, that in order for the classical oscillator to give same frequency than the quantum counterpart, it needs to have energy that is close to the initial and the final states of the quantum oscillator. This means that, if MD is done on a very low energy the oscillator has a very small anharmonic contribution and will give energies that are too large. Ideally thermal energy should be close to zero-point energy, so that classical oscillator would give similar results than its quantum counterpart.

Overtone transition energy is also different between quantum and classical cases. In quantum case there is no difference to normal transition, where the energy represents the difference between the initial and final states. In classical case the oscillator can only access the energy level in which it currently is. This means that the overtone transition energies are multiples of the fundamental energy. This is seen, e.g., in this Thesis for spectra of formic and glycolic acids spectra. In case of Fermi resonance, the interaction between the modes lowers the energy and the overtone energy differs a little from the multiple of fundamental energy. This was seen, e.g., in this Thesis in the benzene spectra (Figure 9.29b and Figure 9.30b). In general, if the overtone energy in MD differs from the multiple of fundamental energy, it is reason to believe that there is some kind of resonance present.

The reason why MD works well for the site structure identification is that the zero-point energy of the QM-molecular mechanics (MM) potential is actually close to the thermal energy. At 10 K the average thermal energy is 7 cm^{-1}, which compared to well depth of 100 − 150 cm^{-1} is about 4-10% of the well depth. The thermal energy can also be compared to the benzene rotation levels (Figure 9.36), to confirm this.

All this means that it is in practice impossible to get completely accurate spectra for matrix isolation with MD. The peak position will never be completely accurate, but site structure information is well coded in the spectra, because the QM-MM potential has relatively good accuracy and the thermal energy is close to its zero-point energy.

The main point with the spectra calculations is the line shapes and the information we can extract from them. Ideally we would like to have accurate line shapes. This would require a large number of trajectories to be calculated in order to get a fully representative thermal average. However, this would then increase the cost of the calculations notably.

The time to calculate the spectra for 20 trajectories and the corresponding PES is about 25000 core hours for small molecules. This means that the calculation can be performed with a single desktop computer in a month. Thermally accurate spectrum, on the other hand, is out of the reach of desktop computers and it needs supercomputer resources.

The main goal is to get information from the site structure. The methodology presented here, using 20 trajectories, can do that in most cases. For some molecules such as benzene, a larger number of trajectories would be needed to get more trajectories representing similar site structures, so that the identification would have more validity. The shape of the spectrum does not in itself give information from the site structure. It would give information from relative probabilities of different sites. Thus, it is most likely more reasonable not to calculate thermal averages of the spectra and only use a small number of trajectories.

The second point that affects line shapes and site structures is the way how the studied system is prepared. Or rather, how well it corresponds to physical experiments. The condensation process (computed) is designed to represent the experimental condensation on a window of a cryostat, and it appears to be a good representation. An alternative way is that there is a surface of matrix atoms onto which the molecules land and then gets buried under other matrix atoms landing on top of it. It can be argued that this would be the more accurate way. It could be simulated, but the system preparation would be much more complicated. Also, the QM-MM potential has significant contribution from the first solvation shell. This means that the spectra does not differentiate on long-range crystal structure and the spectra is solely determined by the first solvation shell.

This way of preparing the system also ends up to the same point as the issue with the number of trajectories. Which is more important: to get information about the site structures or to have more accurate line shapes? If the goal is to get the most accurate line shapes, then it is probably a good idea to simulate the condensation differently. But if the goal is to get information from the site structures then it is best to use a method that gives the maximum variation of sites, so that we can identify as many of them as possible.

9.5.3 *Accuracy of the Potential*

Related to the line shapes, there is also an issue with the potential used to describe the interatomic interactions. How much do the small variations in the potential affect the line shapes? This is a difficult

question and cannot be answered accurately with current methods. To answer this, a set of calculations with different potentials would be needed. The problem is that, in this kind of calculation there is a statistical variation present in the results and, thus, a very large number of trajectories would need to be calculated.

The best way to figure out how much the potential affects the results, is to use differentiable programming [196] to calculate the gradient of the (power) spectrum relative to the potential. This would be a simple use of forward mode automatic differentation. This kind of calculation would consume only about twice the amount of resources compared to a single-trajectory calculation and would give superior accuracy. The problem is that CP2K, used in this research, is not differentiable and this method can not be used with it. To use this method, a completely new MD program would need to be written.

For practical calculations, the greatest issue is that N_2 cannot be used as matrix substance in the simulations, because the pair potential is not adequate. For this case, a general cluster potential would need to be implemented. Since there are no programs available that allow custom potential definition at the time being, this also leads to a situation where a new program needs to be written for such a special case.

N_2 simulations would be interesting also from the experimentalists point of view as in the N_2 matrix especially light-induced molecular processes are often different from experiments performed in lighter noble gas matrices [182].

10 EXCITATIONS

Molecular dynamics allows modeling chemical reactions and investigations to energy transfer mechanisms. This includes also modeling vibrational overtone-induced reactions.

The way how the OH-vibrational overtone was modeled here was based on the change of the velocities of H- and O-atoms, so that the increased kinetic energy would correspond to the energy of vibrational excitation by a photon. After this, MD was used with the NVE ensemble to propagate the system in time.

These simulation studies were done for gas-phase and matrix-embedded molecular systems. From these two, the gas-phase simulations were done first and it was the first part done in this Thesis. The matrix part was the last part of this Thesis, and its purpose was to see how well the developed QM/MM methodology would work with excitations and to give some information on the time scale of vibrational overtone-induced reactions.

10.1 GAS-PHASE SIMULATIONS

The gas-phase simulations used CPMD implemented in the CPMD program [197] and the full description of it is in publication 1.

The main point in the study was to demonstrate that overtone-induced reactions can indeed be simulated with MD. The excitation energy used in the calculations was 532 nm (18787 cm^{-1}), which corresponds the energy of Raman laser used in the vibrational overtone pumping experiments [14].

The simulations showed that exciting the OH vibration in the gas phase caused the conformer to interconvert. However, this change was highly dependent on the initial temperature the simulation was adjusted to correspond to. Using lower excitation energy also lowered the conformational change probability. For the OH-vibrational excitation, the study indicated that the conformational change probably only takes place for trajectories with energies above 14000 cm^{-1}. That being said, the gas-phase simulation was only run for 1 ps, which for matrix simulations is a very short time span, to give conclusive results. For CH-vibrational excitation the conformational interconversion had a higher probability and needed about half of the energy that was needed for OH-vibrational excitation.

This study also included a simulation of the FA-water complex in the gas phase to be compared with the simulations on monomeric formic acid and experimental results on the molecular complex in the matrix [198]. These simulations indicate that there could be a proton-exchange reaction between FA and water, which is connected to the conformation change of FA. This is an interesting new insight

for the experimental work as well and should not be overlooked when trying to understand the experimentally studied molecular processes.

The last contribution of this study was a test on the accuracy of the different functionals in describing proton exchange and high vibrational excitations of the OH bond. The result was that BLYP had problems with high-energy excitations and the conclusion was that it is probably better to use some other functional when the excitation energy is over 10000 cm^{-1}.

10.2 EXCITATIONS IN MATRIX

For matrix simulations, the system was prepared in the same way as for the spectral calculations. After the system was prepared the velocities of the O- and H-atoms were changed to add excitation.

In this case the excitation energies were chosen differently. Classical MD does not include zero-point motion and to compensate for it, a corresponding extra amount of energy was included in the excitation energy. Zero-point energy is in the harmonic approximation one half of the absorption energy in fundamental transition and. For example, the OH fundamental is 3550 cm^{-1} [13], so 1775 cm^{-1} was used for the zero-point energy.

The first overtone has an energy of 6934 cm^{-1}, so the corresponding excitation was 8709 cm^{-1}. This excitation is called as "low" in the following. The other excitation in the simulation was 532 nm to simulate the high overtone excitation [14] that together with the zero-point motion, amount to 20572 cm^{-1}. This is called as "high" in the following.

For low excitation, the BLYP functional was used, but for high we had to use a different functional. This was because in the gas-phase study the functional accuracy test revealed some problems with BLYP when using high-energy excitations.

Optimally the functional would be both accurate and fast, so a gradient-corrected, pure DFT functional was looked for that would be more accurate than BLYP. After some testing we ended up with the M06l functional [68], which exhibits almost as good performance as B3LYP, but would also be more cost effective.

The CP2K settings for high excitation were M06l functional, 350 Ry planewave cut-off, with relative cut-off of 50 Ry, GTH pseudopotentials for PBE-functional and TZVP-MOLOPT-GHT basis functions. 10-Å cubic box was used for the QM part, with the Martyna-Tuckerman Poisson solver [76] to decouple periodic images. The time step used was 0.2 ps.

Low simulation used the same settings that were used for the spectrum calculation for FA, and are the same as for high, but using the BLYP functional instead of M06l. Total of 20 trajectories where run for both excitations.

For high excitation, Figure 10.1 has an example of how the OH-bond length and torsional angle develop after the excitation (at zero time) has been introduced. There is a general trend that almost all

of the excitation energy is transported to the matrix in the first 5 ps. Therefore, only a small trace of the excitation was left in FA. This was the case for all 20 trajectories.

Out of the 20 trajectories only one trajectory changed the conformer from trans to cis. Astonishingly, immediately after this it changed the conformer structure back from cis to trans. For the other trajectories the torsion angle had a maximum in the 40-80 degree range whereas the transition state for the conformer interconversion is about 90 degrees [176].

For low excitation Figure 10.2 sums up the situation for every trajectory. The energy does not move away from the OH stretching vibration to anywhere with in 20 ps.

Looking at the trajectories reveals the reason behind the difference between high and low cases. In the high-case trajectories the energy starts to move after the hydrogen has collided with an argon atom. Before that the energy stays in OH in the same way as it does with a low-energy excitation. The collision with argon seems to induce chaotic movement in FA which results in additional collisions and every such collision transfers a little bit of the energy away from the excited FA molecule. In Figure 10.1a there are some sudden drops in the computed OH-bond length that result from these collisions. In the low-energy case trajectories there are no collisions and, thus, all energy stays in the OH-stretching vibration.

The outcome of this is that the time scale of overtone-induced reactions depends on the excitation energy. Based on this study we could say that in high-overtone excitations (532 nm), the window for reactions is about 5 ps, after which the system has relaxed. For low overtones this study says that the time scale is at least tens of picoseconds and possibly extends to hundreds of picoseconds, which is the experimental estimate for the relaxation time for FA in matrix [199].

The interaction of the molecule with the surrounding matrix seems to only play a crucial role and at least based on this study, it is needed for conformational change to happen in FA.

This is in a qualitative agreement with experimental findings attesting that the conformational changes in small carboxylic acids in low-temperature matrices are coupled to the phonon bath in the solid [200]. Such resonance-assisted tunneling processes have increased tunneling probability for conformational interconversion [201, 202]. Because they couple to the surrounding phonon bath.

10.3 EXCITATION CONCLUSIONS

The time step in CPMD is smaller than in BOMD and, in case of an overtone simulation this is an advantage. This is because the time step is limited by overtone movement when using BOMD, while with CPMD, the overtone does not affect the time step, because the time step is already very small due to orbital propagation.

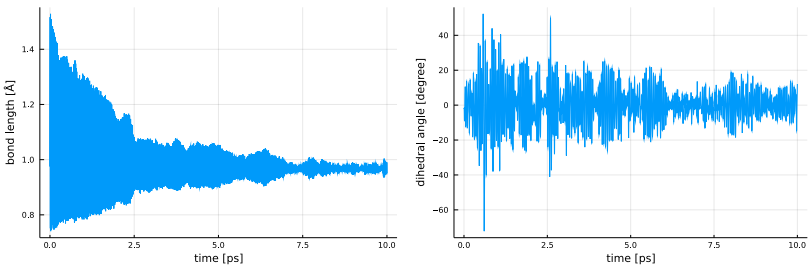

(a) (b)

Figure 10.1: High-energy excitation, OH-bond length (a) and dihedral angle (b).

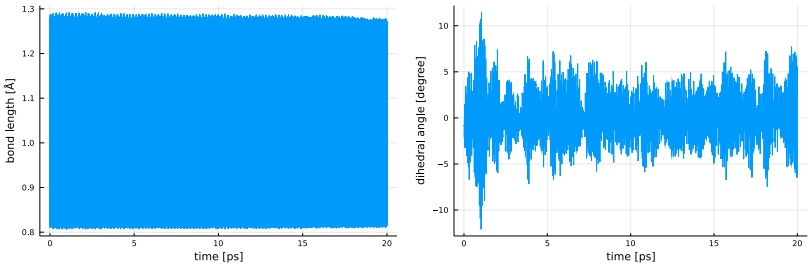

(a) (b)

Figure 10.2: Low-energy excitation, OH-bond length (a) and dihedral angle (b).

With CPMD, the time step was 3 a.u. $\approx$ 0.07 fs, while with BOMD, time step of 0.2 fs was used. Using larger time step for BOMD caused the energy conservation error to be too large, about 10^{-3} for 0.5 fs, and using a smaller time step did not increase the accuracy from 10^{-5} to 10^{-6} range. For CPMD, the accuracy of energy was around 10^{-8} to 10^{-9}. This means that BOMD is both less accurate than CPMD, and also needs more resources (around 3-5 times).

The advantage of BOMD and particularly CP2K is that it has all the needed components in one computational package. It has good integrators, QM/MM in one program and a wide range of functionals. These points together add up to the point that CP2K is overall a better choice than the CPMD program.

In the end the cost of excitation simulation for low excitations is very high due to the small time step, long trajectory and large number of needed trajectories. It is, thus, important to plan the simulations well, as it is possibly a huge waste of resources with very little to be gained.

Another issue is the way how the excitations are initiated. Changing velocities is in practice a hand-waving approach, and ideally a better way to do excitations should be looked for. It should be noted that high vibrational overtones are in practice localized due to the Darling-Dennison resonance. The issue is, however, that there is no way to characterize how much they are localized. It is just a general approximation and it is based on the hope that the approach is adequate when performing the simulation.

One solution to the excitation issue in the simulations would be to use a colored-noise thermostat [148–150], by tuning the thermostat so that it only excites at a given frequency. However, this method has its own problems, too. In order, for anything to happen, enough energy would need to be accumulated, e.g., to get over a potential barrier. With a colored-noise thermostat this accumulation takes time, while in the experiments the energy is transferred the moment the photon is absorbed. The other issue with colored noise is that the excitation is in the vibrational overtone region and thus responds weakly to the thermostat excitations, which is not tested, and it is not sure would it even work.

All this being said, there is certainly some potential with vibrational excitation simulations. It is the only way to get insight into reaction mechanisms. There is, of course, the possibility of using non-linear spectroscopy for this, but at this moment no experimental group has the capability of doing it and because MI experiments are mainly done in a cryostat, it is also much more complicated to achieve.

11 FUTURE DEVELOPMENT

In this chapter we propose several plans on further developments on the basis presented in this Thesis. Some of these proposals are simple and obvious, some are rather advanced and need special programs to be developed.

11.1 IMPROVE THE ACCURACY OF THE CALCULATED SPECTRA

There is a variation in the accuracy of the spectra. The variation is seen in two cases: As decoherence in the background and as noise in the peaks.

Background variation is clearly seen in the overtone region, where there is a difference for different molecules and, for some molecules, even between different trajectories. This most likely means that there are issues with the way MD is done. These issues could be, e.g., the QM box size, convergence criteria, thermostat, barostat etc. Based on this work, the changes in the time step did not have any notable effect on the spectra. This was evidenced in the simulation on the FA spectrum.

The highest accuracy in the computed spectra was found in the computed spectrum of benzene embedded in a Ne matrix, and the most inaccurate was the FA-N_2 complex spectrum. Based on these findings, the issue could be dispersion-functional or box-size related.

To figure out which parameters affect the accuracy, a spectrum needs to be calculated with variations on each of the possible parameters and then compared to each other. This is methodologically easy to do, but time consuming. However, this would be very important for further optimization of the methodology.

11.2 MACHINE LEARNING METHOD TO IDENTIFY SITE STRUCTURES

Identification of the different sites was found out to be a challenging task that only can be done relatively reliably for simple cases. For example, for FA, this task is rather straightforward since only a few matrix sites appear in simulations that corresponds to the three vibrational bands observed in the experiments [177]. For more difficult cases such as benzene in the neon matrix, a machine learning method needs to be developed.

This is a classification problem that is reflected upon in the literature [166]. For example, a support-vector machine classifier might be a good starting point.

One way to implement such a classifier would be to use the graph based method to represent the first solvation shell that was presented in subsection 9.5.1, as computers can handle graphs efficiently. Classi-

fier algorithm would then classify the graphs to groups and combined to peak finding software to compare the locations of peaks, to identify potential site structures.

A good classifier would need to be tested with large number of molecules, which is an extensive computational task. There is also a possibility that this would need several attempts to make a general classifier instead of a one that works for a single molecule. It is thus recommended that development of these machine learning methods would be done in small pieces over time.

The "site classifier", when completed would then automate site identification and also speed up the most time consuming part of matrix simulations considerably.

11.3 GENERAL CLUSTER POTENTIAL

Nitrogen matrix modeling is not possible with the presented pair potential formulation. Tackling this needs to be a major direction in future development. The other direction in development is to increase the accuracy of the currently used pair potentials, which usually have maximum relative errors off about 10%. Both of these need cluster potentials, which depend on "cluster of atoms" in a more complicated way than just relating to the distance between atoms. These cannot be implemented with the current programs.

This is also related to the question on how accurate the potential needs to be in order to get "close enough" results. This is not known at the moment. This could be answered by studying on how stable the local site structures are relative to the potential used.

The usefulness of the nitrogen matrix simulations is self-evident. Argon and nitrogen matrices are the most common experimental matrix solids used, and they are also mixed in some experiments. Having a cluster potential would allow to calculate informative spectra for such cases.

Implementing general cluster potential is not a simple task. The existing MD programs do not allow defining cluster potentials. Thus a new program needs to be made. The easiest way is to use automatic differentation (AD) [196]. Here, only an energy definition is needed and the gradient is automatically calculated. With forward-mode AD [203] there will be no extra cost for gradients and the calculation is also vectorized to get a faster code.

To implement the potential, a pair/cell list [204–207] needs also to be made in order to speed up the calculation. This should be easy, as only the QM-MM interaction needs to be modeled. So, a simple cell list, having cell with the QM system in it and its neighbouring cells will most likely to be sufficient.

The other possibility is to use some kind of neural network potential [208, 209]. However, this would need a large amount of data to train on. Also a potential of the form

$$E(r,\theta) = \sum_{n=6}^{12} \sum_{m=0}^{4} \frac{c_{nm} \cos^m \theta}{r^n} \tag{11.1}$$

was proven to be capable of modeling N_2 potential well, which would most likely be a better option. Given that it would need considerable fewer points for PES calculation than what would be needed to train a neural network.

11.4 ADD MATRIX ENVIRONMENT TO VCI/VPT2 CALCULATIONS

VCI and VPT2 calculations are done on isolated gas-phase molecules. For matrix spectra this means that there is a small error, few to tens of wavenumbers, due to ignored matrix effects.

The matrix atoms change the molecular PES a little bit, which results in a change of the energy levels. If the location of matrix atoms is known their effect to the PES can be calculated and added to the vibrational-level calculation. This kind of calculation should give peak positions to about one wavenumber accuracy and it might be possible to identify sites from these calculations.

From the implementation perspective this is not difficult. VCI starts with a PES calculation and the only thing needed is to add the matrix-interaction potential to PES.

Because VCI is based on matrix diagonalisation, it is also possible to implement gradients relative to the matrix atom positions, which will allow site-structure optimization. The gradients can be implemented either analytically or by using AD.

11.5 QUANTUM DYNAMICS IN MATRIX BASED ON VCI WAVE FUNCTIONS

The current classical dynamics-based simulations have two limitations when modeling excitations: Firstly, they lack quantum effects, such as tunneling and, secondly, feature an *ad hoc* way of doing the excitation. If quantum dynamics would be used, both of these problems would be solved.

By using vibration states from VCI as a basis for the QM part and using MM for matrix atoms, it is possible to do quantum simulations for vibrational states using quantum dynamics. With such an approach, also tunneling could be accounted for, and excitations could be addressed by employing a wavepacket approach.

This would need a special program to be done, but the idea of using vibrational states to model the atom movement is already established [210]. So, the only thing this would add is the interaction with the matrix, which would be somewhat challenging to implement in practice. The difficult part is the computation of gradients for matrix atoms. Using AD this should be achievable.

This method does have considerable size limitations, because quantum dynamics is limited by number of quantum states that can be taken into account. This, combined write the huge number of vibrational states that larger molecules have, results in a situation where only small molecules at low vibrational excitation energies can be simulated.

11.6 LONG-TERM GOAL - COMPLETELY DIFFERENTIABLE PROGRAMS

There is a general consensus among computational chemists that quantum computing and machine learning are the current major prospects.

In machine learning there is an emerging branch that is designed to be a bridge between scientific computing and machine learning called differentiable programming [211]. The brief description is that, from an existing program, one can generate other programs with the use of automatic differentation. This means that the program can be derived relative to any input parameter.

An example of what this allows is training neural networks through differential equation solvers [212, 213]. In computational chemistry, an example of this is training neural network density functional through a DFT program [214, 215]. The advantage here is that experimental data, such as dipole moments, bond lengths, e.g., can be used to train the function. This will lead to a situation where the functional then gives in practice results that are similar to experimental data. This means that we now have the means to create functional that would be the ideal "true" functional.

For matrix isolation simulations differentiable programming would also have a huge impact. It would make it easy to implement every future development proposition presented here.

For example, the accuracy of the spectrum could be studied by taking the derivative of the spectrum relative to the input parameters. Taking derivative relative to potential parameters would reveal how much the potential affects the spectra. Cluster potentials and adding a matrix potential to VCI calculations would also be easy with differentiable programming.

The problem is that none of the existing programs are differentiable and most of them cannot be made such (e.g., programs made with C/C++ or Fortran). Some of them can be made differentiable with limitations (Python). The problem is that, to make a program completely differentiable it needs to be written with a special AD library (e.g., PyTorch) or a language that is completely differentiable (e.g. Julia). This leads to a situation where new programs need to be written from the beginning.

Thus, to use features of differential programming in computational chemistry means that a huge effort is needed to make new programs. This is a process that takes several year to complete, but in the end it will lead to ground-breaking results in every branch of computational chemistry. Together with quantum computing this will lead to a great (positive) change in programs used in computational chemistry.

12

SUMMARY

This Thesis centers on developing a QM/MM-based method to model the interaction between studied molecules and host matrix.

To do this, a set of programs that automate PES calculations was developed. With these programs it is easy to produce and fit the PES for a molecule in a noble-gas matrix. The program can also fit potential for N_2 matrix, but because it needs to be a cluster potential and the lack of cluster potential support in common MD programs. This leads to a situation where only noble-gas matrices can be modeled at this moment.

The developed method was then used with two different use cases: calculation of IR spectra and modeling processes following vibrational overtone excitations.

The calculated IR spectra included first overtone peaks and simple combination peaks in addition to the fundamental ones. In some cases also Fermi resonance peaks were present. However, this was inconsistent in the sense that some Fermi resonance peaks were present and some were not. The reason for this unexpected behavior might be connected to the limitations of the chosen functional (BLYP) and to the used temperature. Because the temperature, which affects the vibrational levels and thus affects the coupling of different vibrational modes.

Different site structures were identified based on the calculated spectra for the all studied molecules/complexes. All of the identified structures had also a counterpart in the experimental spectra.

In the case of benzene embedded in an argon matrix, the calculated spectra was used to identify three sites: One with argon fcc-surface on both sides of the benzene, one with the surface only on one side and one with a random, amorphic, structure of the benzene molecular plane. The separation of these three sites corresponds to the separation of three experimental peaks. Based on experiments, the two lowest-energy peaks disappear when heated (annealing of the matrix sample) leaving only one peak. Based on the calculated data the disappearing peaks are the ones that have the fcc-surface, leaving only the amorphic environment as the most prevalent local site structure.

For formic acid, the simulated spectra had evidence of two main sites and one with a random structure. The two main sites could be identified based on the computed RDFs, and the resulting peaks had the same spectral difference as the two main peaks found in the experimental data. The 3rd site, which has a random/chaotic structure, corresponds to a 3rd peak in the experimental spectra that is present in some measurements. The correlation between simulations and experiments can be based on the positional order of all the observed and simulated vibrational bands.

For formic acid-nitrogen complex the calculated spectra show that the peak structure is a consequence of the orientation of the formic acid and nitrogen relative to each other. The simulated band shape in this case has notable similarities with the experimental spectra.

The accuracy of the calculated spectra is qualitatively accurate, but there are issues with noise, which causes some problems with site identification. This can be remedied with peak fitting to some extent, but further work on finding how to improve accuracy would be a good project to do in the future.

The second case focused on here was to address modeling vibrational excitations in molecule. It was started by doing a gas-phase study by modeling excitation by changing velocities of the atoms to create a vibrational excitation in the simulated system. This was proven to be successful in the gas phase and it was then tried for matrix environment, as well.

Based on this test it is possible to model vibrational excitations, but further study is needed to access further requirements of this kind of study. These issues are mainly related to the computational cost of such calculations. The test showed that the duration of generated trajectories depends on the excitation energy and, additionally, a large number of trajectories is needed to capture relevant information. The future prospect is that this method can be used to study, for example, reaction mechanisms and to find out reaction time scales.

From future usability point-of-view the developed method for spectral calculation is very good. The computed spectra capture almost all main features of the investigated spectra, while it also gives useful information about the local site structures within the studied systems. The method is also now very easy to use, and an experienced user can perform the calculations in two weeks, using about two days of real work and couple of days to analyze the results. The calculations themselves are cost-effective and consume about 20000 to 50000 core hours of computing resources on typical current supercomputers. Based on these points it is likely that the presented methodology will become a standard method in the future investigations to support experimental endeavours, besides quantum-chemical calculations widely used today.

Part III

APPENDIX

BIBLIOGRAPHY

(1) Bondybey, V. E.; Smith, A. M.; Agreiter, J. *Chemical Reviews* **1996**, *96*, 2113–2134.

(2) Barnes, A.; Orville-Thomas, W.; Gaufrès, R.; Müller, A., *Matrix Isolation Spectroscopy*; Nato Science Series C: Springer Netherlands: 2012.

(3) Hallam, H., *Vibrational Spectroscopy of Trapped Species: Infrared and Raman Studies of Matrix-isolated Molecules, Radicals and Ions*; A Wiley-Interscience Publication; J. Wiley: 1973.

(4) Khriachtchev, L.; Pettersson, M.; Runeberg, N.; Lundell, J.; Räsänen, M. *Nature* **2000**, *406*, 874–876.

(5) Khriachtchev, L. *The Journal of Physical Chemistry A* **2015**, *119*, 2735–2746.

(6) Toennies, J. P.; Vilesov, A. F. *Angewandte Chemie International Edition* **2004**, *43*, 2622–2648.

(7) Jasinski, J. M.; Frisoli, J. K.; Moore, C. B. *The Journal of Physical Chemistry* **1983**, *87*, 3826–3829.

(8) Miller, Y.; Chaban, G. M.; Finlayson-Pitts, B. J.; Gerber, R. B. *The Journal of Physical Chemistry A* **2006**, *110*, 5342–5354.

(9) Donaldson, D. J.; Frost, G. J.; Rosenlof, K. H.; Tuck, A. F.; Vaida, V. *Geophysical Research Letters* **1997**, *24*, 2651–2654.

(10) Vaida, V.; Feierabend, K. J.; Rontu, N.; Takahashi, K. Sunlight-Initiated Photochemistry: Excited Vibrational States of Atmospheric Chromophores, 2008.

(11) Gutow, J. H.; Klenerman, D.; Zare, R. N. *The Journal of Physical Chemistry* **1988**, *92*, 172–177.

(12) Scherer, N. F.; Zewail, A. H. *The Journal of Chemical Physics* **1987**, *87*, 97–114.

(13) Pettersson, M.; Lundell, J.; Khriachtchev, L.; Räsänen, M. *Journal of the American Chemical Society* **1997**, *119*, 11715–11716.

(14) Olbert-Majkut, A.; Ahokas, J.; Lundell, J.; Pettersson, M. *The Journal of Chemical Physics* **2008**, *129*, 041101.

(15) Marushkevich, K.; Khriachtchev, L.; Räsänen, M.; Melavuori, M.; Lundell, J. *The Journal of Physical Chemistry A* **2012**, *116*, 2101–2108.

(16) Paulson, L. O.; Anderson, D. T.; Lundell, J.; Marushkevich, K.; Melavuori, M.; Khriachtchev, L. *The Journal of Physical Chemistry A* **2011**, *115*, 13346–13355.

(17) Olbert-Majkut, A.; Ahokas, J.; Lundell, J.; Pettersson, M. *Chemical Physics Letters* **2009**, *468*, 176–183.

(18) Sharma, A.; Reva, I.; Fausto, R. *Journal of the American Chemical Society* **2009**, *131*, 8752–8753.

(19) Marushkevich, K.; Khriachtchev, L.; Räsänen, M. *The Journal of Chemical Physics* **2007**, *126*, 241102.

(20) Olbert-Majkut, A.; Ahokas, J.; Pettersson, M.; Lundell, J. *The Journal of Physical Chemistry A* **2013**, *117*, 1492–1502.

(21) Olbert-Majkut, A.; Lundell, J.; Wierzejewska, M. *The Journal of Physical Chemistry A* **2014**, *118*, 350–357.

(22) Olbert-Majkut, A.; Wierzejewska, M.; Lundell, J. *Chemical Physics Letters* **2014**, *616-617*, 91–97.

(23) Fausto, R. In *Frontiers and Advances in Molecular Spectroscopy*, Laane, J., Ed.; Elsevier: 2018, pp 631–666.

(24) Domanskaya, A.; Marushkevich, K.; Khriachtchev, L.; Räsänen, M. *The Journal of Chemical Physics* **2009**, *130*, 154509.

(25) Maçôas, E. M. S.; Lundell, J.; Pettersson, M.; Khriachtchev, L.; Fausto, R.; Räsänen, M. *Journal of Molecular Spectroscopy* **2003**, *219*, 70–80.

(26) Pettersson, M.; Maçôas, E. M. S.; Khriachtchev, L.; Lundell, J.; Fausto, R.; Räsänen, M. *The Journal of Chemical Physics* **2002**, *117*, 9095–9098.

(27) Marushkevich, K.; Räsänen, M.; Khriachtchev, L. *The Journal of Physical Chemistry A* **2010**, *114*, 10584–10589.

(28) Reva, I. D.; Jarmelo, S.; Lapinski, L.; Fausto, R. *The Journal of Physical Chemistry A* **2004**, *108*, 6982–6989.

(29) Marushkevich, K.; Khriachtchev, L.; Räsänen, M. *The Journal of Physical Chemistry A* **2007**, *111*, 2040–2042.

(30) Pettersson, M.; Maçôas, E. M. S.; Khriachtchev, L.; Fausto, R.; Räsänen, M. *Journal of the American Chemical Society* **2003**, *125*, 4058–4059.

(31) Lopes, S.; Domanskaya, A. V.; Fausto, R.; Räsänen, M.; Khriachtchev, L. *The Journal of Chemical Physics* **2010**, *133*, 144507.

(32) Maçôas, E. M. S.; Khriachtchev, L.; Pettersson, M.; Fausto, R.; Räsänen, M. *Journal of the American Chemical Society* **2003**, *125*, 16188–16189.

(33) Maçôas, E. M. S.; Khriachtchev, L.; Pettersson, M.; Fausto, R.; Räsänen, M. *The Journal of Physical Chemistry A* **2005**, *109*, 3617–3625.

(34) Bazsó, G.; Najbauer, E. E.; Magyarfalvi, G.; Tarczay, G. *The Journal of Physical Chemistry A* **2013**, *117*, 1952–1962.

(35) Kosendiak, I.; Ahokas, J. M. E.; Krupa, J.; Lundell, J.; Wierzejewska, M. *Molecules* **2019**, *24*, 3262.

(36) Kosendiak, I.; Ahokas, J. M. E.; Krupa, J.; Lundell, J.; Wierzejewska, M. *Molecules* **2019**, *24*, 3245.

(37) Ahokas, J. M.; Kosendiak, I.; Krupa, J.; Wierzejewska, M.; Lundell, J. *Journal of Raman Spectroscopy* **2018**, *49*, 2036–2045.

(38) Ahokas, J.; Kosendiak, I.; Krupa, J.; Lundell, J.; Wierzejewska, M. *Journal of Molecular Structure* **2018**, *1163*, 294–299.

(39) Ahokas, J. M. E.; Kosendiak, I.; Krupa, J.; Wierzejewska, M.; Lundell, J. *Journal of Molecular Structure* **2019**, *1183*, 367–372.

(40) Hargittai, M.; Hargittai, I., *Symmetry through the Eyes of a Chemist*, 3rd; Springer: 2010.

(41) *Symmetries in Physics: Philosophical Reflections*; Brading, K., Castellani, E., Eds.; Cambridge University Press: 2010.

(42) Weinberg, S., *The Quantum Theory of Fields, Volume 1: Foundations*; Cambridge University Press: 2005.

(43) Neuenschwander, D. E., *Emmy Noether's Wonderful Theorem*; Johns Hopkins University Press: 2010.

(44) Szekeres, P., *A Course in Modern Mathematical Physics: Groups, Hilbert Space and Differential Geometry*; Cambridge University Press: 2004.

(45) Gilmore, R., *Lie Groups, Lie Algebras, and Some of Their Applications (Dover Books on Mathematics)*; Dover Publications: 2006.

(46) Georgi, H., *Lie Algebras In Particle Physics: from Isospin To Unified Theories (Frontiers in Physics)*; Westview Press: 1999.

(47) Tinkham, M., *Group Theory and Quantum Mechanics (Dover Books on Chemistry)*; Dover Publications: 2003.

(48) Bishop, D. M., *Group Theory and Chemistry (Dover Books on Chemistry)*; Dover Publications: 1993.

(49) Jacobs-University Character tables, http://symmetry.jacobs-university.de, Accessed: 2020-07-20.

(50) Arnold, V. I., *Ordinary Differential Equations*; Springer Berlin Heidelberg: 2006; 344 pp.

(51) Olver, P. J., *Applications of Lie Groups to Differential Equations*, 2nd; Springer New York: 2000; 548 pp.

(52) Weinberg, S., *Lectures on Quantum Mechanics*, 2nd; Cambridge University Pr.: 2015; 425 pp.

(53) Richard Courant, F. J., *Introduction to Calculus and Analysis I*; Springer Berlin Heidelberg: 1998; 688 pp.

(54) Wu, G., *Nonlinearity and Chaos in Molecular Vibrations*; Elsevier Science: 2005.

(55) Shilov, G. E., *Linear algebra*; Dover Publications: New York, 1977.

(56) Szabo, A.; Ostlund, N., *Modern Quantum Chemistry: Introduction to Advanced Electronic Structure Theory*; Dover Books on Chemistry; Dover Publications: 1996.

(57) Jensen, F., *Introduction to Computational Chemistry*; Wiley: 2007.

(58) Helgaker, T.; Olsen, J.; Jorgensen, P., *Molecular Electronic-Structure Theory*; Wiley-Blackwell: 2013; 940 pp.

(59) Hohenberg, P.; Kohn, W. *Physical Review* **1964**, *136*, B864–B871.

(60) Kohn, W.; Sham, L. J. *Physical Review* **1965**, *140*, A1133–A1138.

(61) Marques, M. A. L.; Oliveira, M. J. T.; Burnus, T. *Computer Physics Communications* **2012**, *183*, 2272–2281.

(62) Lehtola, S.; Steigemann, C.; Oliveira, M. J.; Marques, M. A. *SoftwareX* **2018**, *7*, 1–5.

(63) Becke, A. D. *The Journal of Chemical Physics* **2014**, *140*, 18A301.

(64) Martin, R. M., *Electronic Structure*; Cambridge University Press: 2015; 650 pp.

(65) Miehlich, B.; Savin, A.; Stoll, H.; Preuss, H. *Chemical Physics Letters* **1989**, *157*, 200–206.

(66) Becke, A. D. *Physical Review A* **1988**, *38*, 3098–3100.

(67) Lee, C.; Yang, W.; Parr, R. G. *Physical Review B* **1988**, *37*, 785–789.

(68) Zhao, Y.; Truhlar, D. G. *The Journal of Chemical Physics* **2006**, *125*, 194101.

(69) Grimme, S. *Journal of Computational Chemistry* **2006**, *27*, 1787–1799.

(70) Grimme, S.; Antony, J.; Ehrlich, S.; Krieg, H. *The Journal of Chemical Physics* **2010**, *132*, 154104.

(71) Goerigk, L.; Grimme, S. *Physical Chemistry Chemical Physics* **2011**, *13*, 6670.

(72) Caldeweyher, E.; Ehlert, S.; Hansen, A.; Neugebauer, H.; Spicher, S.; Bannwarth, C.; Grimme, S. *The Journal of Chemical Physics* **2019**, *150*, 154122.

(73) Marx, D.; Hutter, J., *Ab Initio Molecular Dynamics: Basic Theory and Advanced Methods*; Cambridge University Press: 2012.

(74) Genovese, L.; Deutsch, T.; Neelov, A.; Goedecker, S.; Beylkin, G. *The Journal of Chemical Physics* **2006**, *125*, 074105.

(75) Genovese, L.; Deutsch, T.; Goedecker, S. *The Journal of Chemical Physics* **2007**, *127*, 054704.

(76) Martyna, G. J.; Tuckerman, M. E. *The Journal of Chemical Physics* **1999**, *110*, 2810–2821.

(77) Blöchl, P. E. *The Journal of Chemical Physics* **1995**, *103*, 7422–7428.

(78) Boys, S.; Bernardi, F. *Molecular Physics* **1970**, *19*, 553–566.

(79) Klopper, W.; Samson, C. C. M. *The Journal of Chemical Physics* **2002**, *116*, 6397–6410.

(80) Adler, T. B.; Knizia, G.; Werner, H.-J. *The Journal of Chemical Physics* **2007**, *127*, 221106.

(81) Dunham, J. L. *Physical Review* **1932**, *41*, 721–731.

(82) Inostroza, N.; Letelier, J. R.; Senent, M. L. *Journal of Molecular Structure: THEOCHEM* **2010**, *947*, 40–44.

(83) Morse, P. M. *Physical Review* **1929**, *34*, 57–64.

(84) Dahl, J. P.; Springborg, M. *The Journal of Chemical Physics* **1988**, *88*, 4535–4547.

(85) Atkins, P. W.; Friedman, R. S., *Molecular Quantum Mechanics*, 3rd; Oxford University Press: 1999.

(86) Steinfeld, J. I., *Molecules and Radiation: An Introduction to Modern Molecular Spectroscopy. Second Edition (Dover Books on Chemistry)*; Dover Publications: 2005.

(87) Hollas, J. M., *Modern Spectroscopy*, 4th; Wiley: 2004.

(88) Wu, G. *Chemical Physics* **2001**, *269*, 93–99.

(89) Yu, J.; Wu, G. *The Journal of Chemical Physics* **2000**, *113*, 647–652.

(90) Field, R. W. W., *Spectra and Dynamics of Small Molecules: Alexander von Humboldt Lectures (Lecture Notes in Physics)*; Springer: 2015.

(91) Albert, S.; Albert, K. K.; Hollenstein, H.; Tanner, C. M.; Quack, M. In *Handbook of High-resolution Spectroscopy*; John Wiley & Sons, Ltd: 2011.

(92) Kellman, M. E.; Tyng, V. *Accounts of Chemical Research* **2007**, *40*, 243–250.

(93) Darling, B. T.; Dennison, D. M. *Physical Review* **1940**, *57*, 128–139.

(94) Lehmann, K. K. *Molecular Physics* **1989**, *66*, 1129–1137.

(95) Lehmann, K. K. *The Journal of Chemical Physics* **1992**, *96*, 8117–8119.

(96) Jungen, C. *Journal of Molecular Spectroscopy* **2019**, *363*, 111172.

(97) Renner, R. *Zeitschrift für Physik* **1934**, *92*, 172–193.

(98) Wormer, P. E. S.; Herzberg, G.; Teller, E., 13.

(99) Richardson, J. O. *International Reviews in Physical Chemistry* **2018**, *37*, 171–216.

(100) Mil'nikov, G.; Nakamura, H. *Physical Chemistry Chemical Physics* **2008**, *10*, 1374–1393.

(101) Stohner, J.; Quack, M. In *Handbook of High-resolution Spectroscopy*; John Wiley & Sons, Ltd: 2011.

(102) Watson, J. K. *Molecular Physics* **1968**, *15*, 479–490.

(103) Bauder, A. In *Handbook of High-resolution Spectroscopy*; John Wiley & Sons, Ltd: 2011.

(104) Gong, J. Z.; Matthews, D. A.; Changala, P. B.; Stanton, J. F. *The Journal of Chemical Physics* **2018**, *149*, 114102.

(105) Piccardo, M.; Bloino, J.; Barone, V. *International Journal of Quantum Chemistry* **2015**, *115*, 948–982.

(106) Mills, I. M. *Journal of Molecular Spectroscopy* **1961**, *5*, 334–340.

(107) Barone, V. *The Journal of Chemical Physics* **2004**, *122*, 014108.

(108) Carter, S.; Culik, S. J.; Bowman, J. M. *The Journal of Chemical Physics* **1997**, *107*, 10458–10469.

(109) Neff, M.; Rauhut, G. *The Journal of Chemical Physics* **2009**, *131*, 124129.

(110) Changala, P. B.; Baraban, J. H. *The Journal of Chemical Physics* **2016**, *145*, 174106.

(111) Norris, L. S.; Ratner, M. A.; Roitberg, A. E.; Gerber, R. B. *The Journal of Chemical Physics* **1996**, *105*, 11261–11267.

(112) Christiansen, O. *The Journal of Chemical Physics* **2003**, *119*, 5773–5781.

(113) Scribano, Y.; Benoit, D. M. *Chemical Physics Letters* **2008**, *458*, 384–387.

(114) Strobusch, D.; Scheurer, C. *The Journal of Chemical Physics* **2011**, *135*, 144101.

(115) Christiansen, O. *Physical Chemistry Chemical Physics* **2007**, *9*, 2942–2953.

(116) Seidler, P.; Sparta, M.; Christiansen, O. *The Journal of Chemical Physics* **2011**, *134*, 054119.

(117) Baiardi, A.; Stein, C. J.; Barone, V.; Reiher, M. *Journal of Chemical Theory and Computation* **2017**, *13*, 3764–3777.

(118) Huang, X.; McCoy, A. B.; Bowman, J. M.; Johnson, L. M.; Savage, C.; Dong, F.; Nesbitt, D. J. *Science* **2006**, *311*, 60–63.

(119) Pesonen, J. *The Journal of Chemical Physics* **2014**, *140*, 074101.

(120) Rauhut, G. *The Journal of Chemical Physics* **2004**, *121*, 9313–9322.

(121) Hrenar, T.; Werner, H.-J.; Rauhut, G. *The Journal of Chemical Physics* **2007**, *126*, 134108.

(122) Car, R.; Parrinello, M. *Physical Review Letters* **1985**, *55*, 2471–2474.

(123) Brunk, E.; Rothlisberger, U. *Chemical Reviews* **2015**, *115*, 6217–6263.

(124) Warshel, A.; Levitt, M. *Journal of Molecular Biology* **1976**, *103*, 227–249.

(125) Rackauckas, C. What does "symplectic" mean in reference to numerical integrators, and does SciPy's odeint use them? Computational Science Stack Exchange, https://scicomp.stackexchange.com/q/29154 (version: 2020-07-19).

(126) Tuckerman, M. E., *Statistical Mechanics: Theory and Molecular Simulation (Oxford Graduate Texts)*; Oxford University Press: 2010.

(127) Press, W. H.; Teukolsky, S. A.; Vetterling, W. T.; Flannery, B. P., *Numerical Recipes*; Cambridge University Pr.: 2007; 1248 pp.

(128) Verlet, L. *Physical Review* **1967**, *159*, 98–103.

(129) Swope, W. C.; Andersen, H. C.; Berens, P. H.; Wilson, K. R. *The Journal of Chemical Physics* **1982**, *76*, 637–649.

(130) Mazur, A. K. *Journal of Computational Physics* **1997**, *136*, 354–365.

(131) Cuendet, M. A.; van Gunsteren, W. F. *The Journal of Chemical Physics* **2007**, *127*, 184102.

(132) Ryckaert, J.-P.; Ciccotti, G.; Berendsen, H. J. *Journal of Computational Physics* **1977**, *23*, 327–341.

(133) Andersen, H. C. *Journal of Computational Physics* **1983**, *52*, 24–34.

(134) Martyna, G. J.; Tuckerman, M. E.; Tobias, D. J.; Klein, M. L. *Molecular Physics* **1996**, *87*, 1117–1157.

(135) Feynman, R. P., *Statistical Mechanics: A Set Of Lectures (Frontiers in Physics)*; CRC Press: 1998.

(136) Dunkel, J.; Hilbert, S. *Nature Physics* **2014**, *10*, 67–72.

(137) Landau, L. D.; Lifshitz, E., *Statistical Physics, Part 1: Volume 5 (Course of Theoretical Physics)*, 3rd; Butterworth-Heinemann: 1980.

(138) Breuer, H.-P.; Petruccione, F., *The Theory of Open Quantum Systems*; Oxford University Press: 2007.

(139) Stefanucci, G.; van Leeuwen, R., *Nonequilibrium many-body theory of quantum systems : A modern introduction*; Cambridge University Press: Cambridge, 2013.

(140) Pearle, P. *European Journal of Physics* **2012**, *33*, 805–822.

(141) Andersen, H. C. *The Journal of Chemical Physics* **1980**, *72*, 2384–2393.

(142) Berendsen, H. J. C.; Postma, J. P. M.; van Gunsteren, W. F.; DiNola, A.; Haak, J. R. *The Journal of Chemical Physics* **1984**, *81*, 3684–3690.

(143) Bussi, G.; Donadio, D.; Parrinello, M. *The Journal of Chemical Physics* **2007**, *126*, 014101.

(144) Nosé, S. *Molecular Physics* **1984**, *52*, 255–268.

(145) Nosé, S. *The Journal of Chemical Physics* **1984**, *81*, 511–519.

(146) Hoover, W. G. *Physical Review A* **1985**, *31*, 1695–1697.

(147) Martyna, G. J.; Klein, M. L.; Tuckerman, M. *The Journal of Chemical Physics* **1992**, *97*, 2635–2643.

(148) Ceriotti, M. A novel framework for enhanced molecular dynamics based on the generalized Langevin equation, https://doi.org/10.3929/ethz-a-006233446, Ph.D. Thesis, ETH Zürich, 2010.

(149) Ceriotti, M.; Bussi, G.; Parrinello, M. *Physical Review Letters* **2009**, *102*, 020601.

(150) Ceriotti, M.; Bussi, G.; Parrinello, M. *Journal of Chemical Theory and Computation* **2010**, *6*, 1170–1180.

(151) Craig, D. P.; Thirunamachandran, T., *Molecular Quantum Electrodynamics*; Dover Publications Inc.: 1998; 336 pp.

(152) Berestetskii, V. B.; Lifshitz, E. M.; Pitaevskii, L. P., *Quantum electrodynamics: Volume 4 (Course of Theoretical Physics)*; 2nd, Ed.; Butterworth-Heinemann: Oxford, 1982.

(153) Mukamel, S., *Principles of Nonlinear Optical Spectroscopy (Oxford Series in Optical and Imaging Sciences)*; Oxford University Press: 1999.

(154) Hamm, P.; Zanni, M., *Concepts and Methods of 2D Infrared Spectroscopy*; Cambridge University Press: 2012; 298 pp.

(155) Tannor, D., *Introduction to quantum mechanics : A time-dependent perspective*; University Science Books: Sausalito, Calif, 2007.

(156) Wilson Jr, B. E.; Decius, J.; Cross, P. C., *Molecular Vibrations: The Theory of Infrared and Raman Vibrational Spectra (Dover Books on Chemistry)*; Dover Publications: 1980.

(157) Khriachtchev, L., Unpublished.

(158) Thomas, M.; Brehm, M.; Fligg, R.; Vöhringer, P.; Kirchner, B. *Physical Chemistry Chemical Physics* **2013**, *15*, 6608.

(159) Weisstein, E. W. Wiener-Khinchin Theorem, Text, Publisher: Wolfram Research, Inc.

(160) Thomas, M.; Brehm, M.; Kirchner, B. *Physical Chemistry Chemical Physics* **2015**, *17*, 3207–3213.

(161) Bezanson, J.; Edelman, A.; Karpinski, S.; Shah, V. B. *SIAM Review* **2017**, *59*, 65–98.

(162) Neese, F. *WIREs Computational Molecular Science* **2012**, *2*, 73–78.

(163) Neese, F. *WIREs Computational Molecular Science* **2018**, *8*, e1327.

(164) Smith, D. G. A. et al. *The Journal of Chemical Physics* **2020**, *152*, 184108.

(165) Simon, S.; Duran, M.; Dannenberg, J. J. *The Journal of Chemical Physics* **1996**, *105*, 11024–11031.

(166) Géron, A., *Hands-on machine learning with Scikit-Learn and TensorFlow : Concepts, tools, and techniques to build intelligent systems*; O'Reilly Media: Sebastopol, CA, 2017.

(167) Pedregosa, F. et al. *Journal of Machine Learning Research* **2011**, *12*, 2825–2830.

(168) Tew, D. P.; Klopper, W.; Bachorz, R. A.; Hättig, C. In *Handbook of High-resolution Spectroscopy*; John Wiley & Sons, Ltd: 2011.

(169) Kühne, T. D. et al. *The Journal of Chemical Physics* **2020**, *152*, 194103.

(170) Dewar, M. J. S.; Zoebisch, E. G.; Healy, E. F.; Stewart, J. J. P. *Journal of the American Chemical Society* **1985**, *107*, 3902–3909.

(171) Řezáč, J.; Fanfrlik, J.; Salahub, D.; Hobza, P. *Journal of Chemical Theory and Computation* **2009**, *5*, 1749–1760.

(172) RadiationSpectra.jl, https://github.com/JuliaPhysics/RadiationSpectra.jl, Based on CERN ROOT software.

(173) Mariscotti, M. A. *Nuclear Instruments and Methods* **1967**, *50*, 309–320.

(174) Morháč, M.; Kliman, J.; Matoušek, V.; Veselský, M.; Turzo, I. *Nuclear Instruments and Methods in Physics Research Section A: Accelerators, Spectrometers, Detectors and Associated Equipment* **2000**, *443*, 108–125.

(175) Silagadze, Z. *Nuclear Instruments and Methods in Physics Research Section A: Accelerators, Spectrometers, Detectors and Associated Equipment* **1996**, *376*, 451–454.

(176) Tew, D. P.; Mizukami, W. *The Journal of Physical Chemistry A* **2016**, *120*, 9815–9828.

(177) Maçôas, E. M. S.; Lundell, J.; Pettersson, M.; Khriachtchev, L.; Fausto, R.; Räsänen, M. *Journal of Molecular Spectroscopy* **2003**, *219*, 70–80.

(178) Lundell, J.; Räsänen, M.; Latajka, Z. *Chemical Physics* **1994**, *189*, 245–260.

(179) Marushkevich, K.; Räsänen, M.; Khriachtchev, L. *The Journal of Physical Chemistry A* **2010**, *114*, 10584–10589.

(180) Jolkkonen, S.; Pettersson, M.; Lundell, J. *The Journal of Chemical Physics* **2003**, *119*, 7356–7364.

(181) Trakhtenberg, L. I.; Fokeyev, A. A.; Zyubin, A. S.; Mebel, A. M.; Lin, S. H. *The Journal of Chemical Physics* **2009**, *130*, 144502.

(182) *Physics and Chemistry at Low Temperatures*; Khriachtchev, L., Ed.; Jenny Stanford Publishing: 2011.

(183) Nunes, C. M.; Reva, I.; Fausto, R. *Physical Chemistry Chemical Physics* **2019**, *21*, 24993–25001.

(184) Reva, I. D.; Jarmelo, S.; Lapinski, L.; Fausto, R. *Chemical Physics Letters* **2004**, *389*, 68–74.

(185) Nejad, A.; Meyer, E.; Suhm, M. A. *The Journal of Physical Chemistry Letters* **2020**, *11*, 5228–5233.

(186) Hollenstein, H.; Ha, T. .-.; Günthard, H. H. *Journal of Molecular Structure* **1986**, *146*, 289–307.

(187) Krupa, J.; Kosendiak, I.; Wierzejewska, M.; Ahokas, J.; Lundell, J. *Journal of Photochemistry and Photobiology A: Chemistry* **2021**, *412*, 113236.

(188) Halasa, A.; Lapinski, L.; Reva, I.; Rostkowska, H.; Fausto, R.; Nowak, M. J. *The Journal of Physical Chemistry A* **2014**, *118*, 5626–5635.

(189) Lignell, A.; Lüttschwager (Domanskaya), A.; Gor, G. *Chemical Physics Letters* **2020**, *757*, 137844.

(190) Wang, S. *Scientific Reports* **2020**, *10*, DOI: 10.1038/s41598-020-74872-6.

(191) Kim, H. S.; Kim, K. *Spectroscopy Letters* **1996**, *29*, 667–675.

(192) Chandrasekaran, V.; Biennier, L.; Arunan, E.; Talbi, D.; Georges, R. *The Journal of Physical Chemistry A* **2011**, *115*, 11263–11268.

(193) Miani, A.; Cané, E.; Palmieri, P.; Trombetti, A.; Handy, N. C. *The Journal of Chemical Physics* **1999**, *112*, 248–259.

(194) Basire, M.; Mouhat, F.; Fraux, G.; Bordage, A.; Hazemann, J.-L.; Louvel, M.; Spezia, R.; Bonella, S.; Vuilleumier, R. *The Journal of Chemical Physics* **2017**, *146*, 134102.

(195) Landau, L. D.; Lifshitz, E., *Mechanics: Volume 1 (Course of Theoretical Physics)*; Butterworth-Heinemann: 1976.

(196) Andreas Griewank, A. W., *Evaluating Derivatives: Principles and Techniques of Algorithmic Differentiation*; CAMBRIDGE: 2008; 460 pp.

(197) CPMD, Copyright IBM Corp 1990–2015, https://www.cpmd.org.

(198) Marushkevich, K.; Khriachtchev, L.; Räsänen, M. *The Journal of Physical Chemistry A* **2007**, *111*, 2040–2042.

(199) Maçôas, E. M. S.; Myllyperkiö, P.; Kunttu, H.; Pettersson, M. *The Journal of Physical Chemistry A* **2009**, *113*, 7227–7234.

(200) Maçôas, E. M. S.; Khriachtchev, L.; Pettersson, M.; Fausto, R.; Räsänen, M. *The Journal of Chemical Physics* **2004**, *121*, 1331–1338.

(201) Nunes, C. M.; Reva, I.; Fausto, R. In *Tunnelling in Molecules: Nuclear Quantum Effects from Bio to Physical Chemistry*; The Royal Society of Chemistry: 2021, pp 1–60.

(202) Brodier, O.; Schlagheck, P.; Ullmo, D. *Annals of Physics* **2002**, *300*, 88–136.

(203) Revels, J.; Lubin, M.; Papamarkou, T. *arXiv:1607.07892 [cs.MS]* **2016**.

(204) Heinz, T. N.; Hünenberger, P. H. *Journal of Computational Chemistry* **2004**, *25*, 1474–1486.

(205) Gonnet, P. *Journal of Computational Chemistry* **2007**, *28*, 570–573.

(206) Chowdhury, R.; Beglov, D.; Moghadasi, M.; Paschalidis, I. C.; Vakili, P.; Vajda, S.; Bajaj, C.; Kozakov, D. *Journal of Chemical Theory and Computation* **2014**, *10*, 4449–4454.

(207) Yao, Z.; Wang, J.-S.; Liu, G.-R.; Cheng, M. *Computer Physics Communications* **2004**, *161*, 27–35.

(208) Gao, X.; Ramezanghorbani, F.; Isayev, O.; Smith, J. S.; Roitberg, A. E. *Journal of Chemical Information and Modeling* **2020**, *60*, 3408–3415.

(209) Chmiela, S.; Sauceda, H. E.; Müller, K.-R.; Tkatchenko, A. *Nature Communications* **2018**, *9*, 1–10.

(210) Qu, C.; Bowman, J. M. *The Journal of Physical Chemistry Letters* **2018**, *9*, 2604–2610.

(211) Innes, M.; Edelman, A.; Fischer, K.; Rackauckas, C.; Saba, E.; Shah, V. B.; Tebbutt, W. *arXiv:1907.07587 [cs]* **2019**.

(212) Chen, R. T. Q.; Rubanova, Y.; Bettencourt, J.; Duvenaud, D. *arXiv:1806.07366 [cs, stat]* **2019**.

(213) Rackauckas, C.; Innes, M.; Ma, Y.; Bettencourt, J.; White, L.; Dixit, V. *arXiv:1902.02376 [cs, stat]* **2019**.

(214) Kasim, M. F.; Vinko, S. M. *arXiv:2102.04229 [physics]* **2021**.

(215) Kasim, M. F.; Lehtola, S.; Vinko, S. M. *The Journal of Chemical Physics* **2022**, *156*, 084801.

ORIGINAL PAPERS

I

AB INITIO MOLECULAR DYNAMICS STUDY OF OVERTONE EXCITATIONS IN FORMIC ACID AND ITS WATER COMPLEX

by

T. Järvinen, J. Lundell and P. Dopieralski 2018

Theoretical Chemistry Accounts 137, 100

https://doi.org/10.1007/s00214-018-2280-6

Noname manuscript No.
(will be inserted by the editor)

Ab Initio Molecular Dynamics Study of Overtone Excitations in Formic acid and its Water Complex

Teemu Järvinen · Jan Lundell · Przemysław Dopieralski

Received: date / Accepted: date

Abstract In this article we present results from ab initio molecular dynamics simulation of overtone excitation in formic acid monomer and its water complex in the gas phase. For the monomer a conformation change is observed employing both OH and CH vibrational excitation, which supports experimental findings. In the water conformed a conformer interconversion also takes place but it proceeds via hydrogen exchange together with the water molecule. Simulations raise a questions on effect of quantum and matrix effects to the results. Also a small testing of different computation methods was done on the system.

Keywords formic acid · overtone · proton exchange · vibration induced chemistry

1 Introduction

The high overtone induced processes are initiated by promoting a molecule or a complex to chemically relevant energies in high vibrational excited states through the thermal excitation or direct absorption of visible or near-infrared radiation. Unlike the thermally induced processes, the reactions initiated by vibrational overtone-pumping of ground electronic state molecule through direct absorption of photon can be treated without the need to consider collisional activation processes. In general, it is required that the energy is deposited into the initially excited vibrational state and subsequently transferred by intramolecular vibrational redistribution to other modes of the molecule including the reaction coordinate. For example, it has been demonstrated that high overtone excitation of OH groups in carboxylic acids isolated in low temperature matrices leads to two different unimolecular processes: isomerization and/or decomposition of the molecules [1,2,3,4]. Moreover, overtone pumping was used, for example, in the case of formic acid dimers to produce high-energy conformers within the hydrogen-bonded complexes [5,6,7].

In case of formic acid it has been shown to change conformation from trans to cis [1], see figure 1, and that formed cis conformer reorganises back to to trans form via a tunneling mechanism [8]. But in formic acid water complex this conversion back from trans to cis does not happen [9].

The aim of this study was to try to simulate using ab-initio molecular dynamics these conformation changes that have been observed in experiments. In particular the aim was to try to see if 532 nm excitation energy could produce these results, as this has been the laser wavelength used to produce high-overtone interconversions, for example, for formic, oxalic and glyoxylic acids [2,10].

2 Method

Ab-initio molecular dynamics simulations were done with Car-Parrinello method [11,12], using CPMD v. 4.1 [13]. Calculations were done using BLYP functional with D2 dispersion correction, using Troullier-Martins pseudo potentials [14] with 90 ry cutoff, 3 au time step and 400 au fictitious electronic mass. Simulation box was cubic 10 Å for monomer and 14 Å for water com-

Teemu Järvinen
University of Jyväskylä
E-mail: teemu.j.jarvinen@student.jyu.fi

Jan Lundell
University of Jyväskylä
E-mail: jan.c.lundell@jyu.fi

Przemysław Dopieralski
University of Wrocław

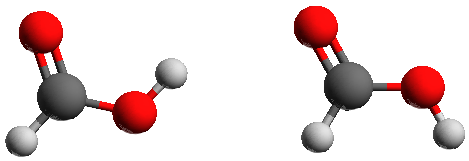

Fig. 1 Trans (left) and cis (right) conformers of formic acid.

plex. Periodic images were decoupled using Martyna-Tuckerman Poisson solver [15]. Simulation box sizes were verified by increasing box sizes and doing geometry optimization, which had no difference in energy or geometry. The plane wave cutoff was chosen because it has been used on a similar system [16].

To generate trajectories system was first propagated using velocity rescaling thermostat for ~ 1 ps, in NVT conditions, followed by ~ 5 ps using Nose-Hoover chain thermostat [12,17], in global mode. After which a total of 100 snapshots were saved in every ~ 1 ps, while continuing with Nose-Hoover chain thermostat.

To simulate vibration excitations velocities in these snapshots were modified, so that kinetic energy is increased by a desired amount. According to hypothesis energy is added to OH stretching vibration. Also for formic acid monomer CH stretching excitations were done. Velocities were changed so that center of mass velocity does not change and that O and H atoms move away form each other. Due to mass difference this means that hydrogen will take most of the added kinetic energy in relation to mass difference. It also should be noted that because only O and H atoms, which form OH bond, have their velocities changed, there is also a little bit of energy added to COH bending and OCOH torsion motions. After adding velocities each snapshot was propagated forward in NVE conditions, thus creating a total of 100 trajectories.

For formic acid monomer the trajectories were propagated for about 1 ps. For water complex the trajectories had to be cut to about 200 fs, because complex dissociates due to added energy and fragments fly out of the simulation box. Also water complex is not stable in 300 K, and thus only 15 K and 200 K trajectories were generated, while for monomer 15 K, 100 K, 200 K and 300 K trajectories were generated. These temperatures are arbitrary chosen, to see how temperature affects the system and such they have no specific meaning. Also when temperature is is addressed later in this article, it always refers to these values before excitation was applied.

In these trajectories we are interested in question is there is a a conformation change. This means that results from these trajectories are in form of probabilities to find something, which can be considered to behave like a binomial-distribution. To assess these probabilities and errors Bayesian-statistics [18] was used. In Bayesian-statistics binomial-distribution has a Bayesian-interface via beta-distribution, from which a probability to find a desired result can be taken as mean and error from associated cumulative distribution function. Even likelihood, $\beta(1,1)$-distribution, was used as a prior. In presented results errors (dotted lines) represent 95% confidence interval.

3 Results

3.1 Monomer

Results from trajectories excited by 532 nm excitations to OH vibration are shown in figure 2. The most prominent feature is that conformation change is more probable in higher temperatures and it was not observed at all in 15 K. In case of CH excitation, figure 3, the conformation change is much more probable and temperature has only a minor effect. Conformation change was observed when excitation energy 1200 nm (8300 cm^{-1}) or more, when CH bond was excited. We didn't find any conformation changes with 1700 nm (6000 cm^{-1}) excitation energy. However due to statistical nature of results, we can only say this in about 95 % certainty. With OH excitation conformation change was observed when energy was 700 nm (14000 cm^{-1}) or more and was not observed when energy was 800 nm (12500 cm^{-1}).

To see how energy is transfered in molecule movement of certain parameters describing molecule was visualized see figures 4 and 5. Kinetic energy is related to square of change, so parameters chosen are square of change in distance and square of change in angle, although it should be noted that for e.g. bending motion kinetic energy depend on angular velocity and bond lengths, so care must be kept in mind when interpreting these figures.

From OH excited case, figure 4, gradual decrease of motion in OH bond and gradual increase of motion in other modes. COH bending motion seem to be excited earlier than OCOH torsional motion. Which could suggest that energy energy transfers from OH stretching to COH bending and then to OCOH torsion. To test this this hypothesis a new set of trajectories was generated with an added constraint on COH bending, which fixed COH angle to its initial value. In these trajectories no

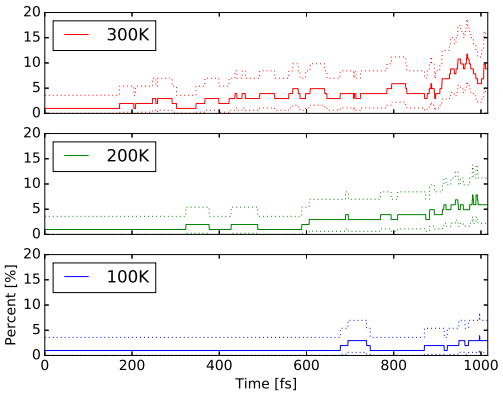

Fig. 2 Probability to find cis conformer after OH excitation (532 nm) in different initial temperatures.

conformation changes were observed, which supports our hypothesis.

CH excitation data, figure 5, differs from OH excitation that OCH bending gains initially some energy and then starts to degrease. This points on possibility of this mode being part of energy channel and to test this a set of trajectories was made with a constraint on OCH motion. This lowered conformation change probability by ten fold of its initial value. From the figure can also be seen that COH bending motion is excited before OCOH torsion, so we could expect it to be part of energy channel, as it is in OH excitation. To test this a set of trajectories was again generated with a constraint on COH angle. This lowered conformation change probability to one third of its initial value. This suggest that there are two channels for energy transfer a one from CH stretch -> OCH bending -> OCOH torsion and an other from CH stretch -> COH bending -> OCOH torsion. However these two depend on each other, as the OCH constraint decreases movement in COH bending considerably. Which suggest that a third channel exists where energy transfers along path CH stretch -> OCH bending -> COH bending -> OCOH torsion.

Also worth of mentioning is that energy added to COH bending and OCOH torsion motions due to our method of exciting molecule is small, as can be seen from the figures at time zero, and thus is not expected to affect results.

3.2 Water Complex

The most prominent feature of trajectories is hydrogen exchange with water molecule (see figure 6). This happens in all trajectories sampled from 15 K temperature (figure 7), while at 200 K the exchange probability diminishes due to increased rotation of the water

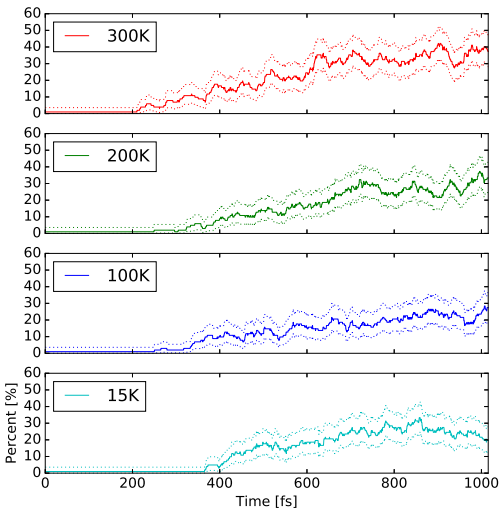

Fig. 3 Probability to find cis conformer after CH excitation (532 nm) in different initial temperatures.

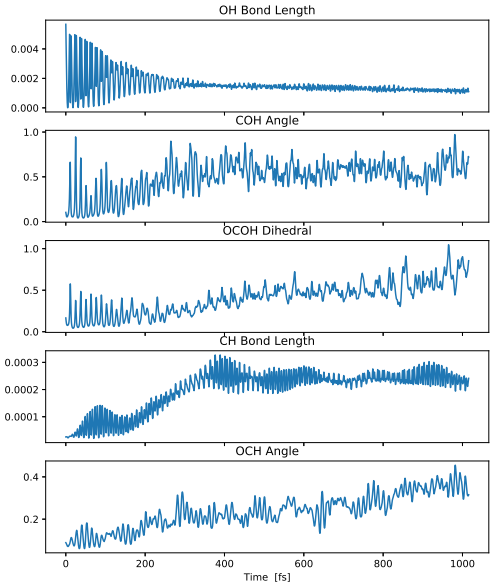

Fig. 4 Square of change in some parameters describing molecule after exciting OH bond. This data is taken from trajectories sampled at 200 K and excited with 532 nm excitation. Note that y-axis is arbitrary and can be used only to make relative estimates of change.

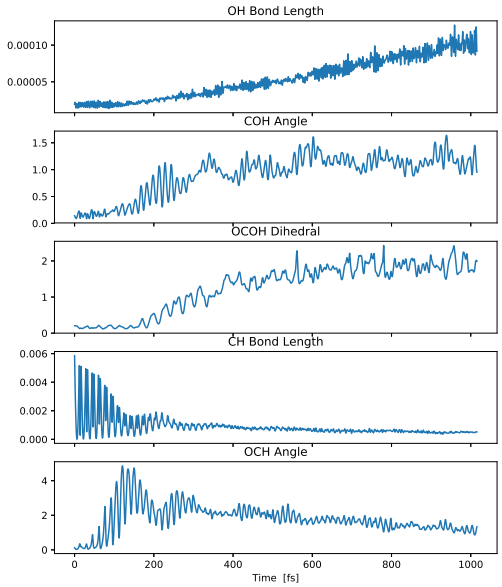

Fig. 5 Square of change in some parameters describing molecule after exciting CH bond. This data is taken from trajectories sampled at 200 K and excited with 532 nm excitation. Note that y-axis is arbitrary and can be used only to make relative estimates of change.

molecule. The exchange could be found in trajectories (200 K) when excitation energy used was 1200 nm (8300 cm^{-1}) or more.

First step of the reaction is formation of H_3O^+ and formate ions, figure 8, and after that one of the hydrogens from the H_3O^+ is given back to the formate ion. This hydrogen can then bounce back to the water molecule to form an H_3O^+ ion again, which can be seen in figure 8 as a second peak. While hydrogen exchange maximum, figure 6, is between these two peaks. Again the H_3O^+ ion gives up one of it's hydrogens to form formic acid and water. This can be repeated for a third time, see small peak appearing at ca. 60-70 fs in figure 8. Ultimately water and formic acid dissociate.

In some rare events formic acid first exchanges hydrogen with water and then changes conformation. This happens in 3 out of 100 trajectories both at 15 K and 200 K, but only at near end of the trajectories close to 200 fs, which compares well with the monomer results, figure 2, with the exception that now it happens in 15 K as well.

Transition state for hydrogen exchange reaction is a little bit of complicated. When transition state is calculated with traditional quantum chemistry methods, by searching a saddle point (done with ORCA v. 3.0.3 [19]), results in geometry represented in figure 9. While in trajectories transition state is usually like a geometry in second from right in figure 6 and in a few cases close to what is represented in figure 9. This would suggest that there are two different reaction paths and associating transition states. This however is not the case.

By inspecting trajectories more reveals that the rarer case is never present in first wave of exchanges, which can be seen in figure 7 as the first peak in around 25 fs. Also in the transition state the distance between water and formic acid is about 0.5 Å shorter than what it's in minimum energy geometry of the complex. So to get to the "true" transition state, water and formic acid would have to move closer. Here comes the fact that we have a lot of energy and that hydrogens move a lot of faster than oxygen. So when hydrogen is transfered to the water, the oxygen does not have enough time to move closer and instead one of the hydrogens will just fly away from the the H_3O^+ ion. In an analogy this could be thought of like playing billiard, when one ball hits hard a group of balls next to each other, or like Newton's cradle.

Energies calculated with different methods and basis for the transition state, figure 9, are listed in tables 1 and 2. These values differ a lot from method to method, which is inspected more later. This calculated energy represent the minimum energy path. But the true energy depends on how long the distance is between the two molecules, which can be explained by a potential energy between two ions increasing with distance. When the distance is around the minimum energy geometry of the complex transition state energy is a little bit over 12000 cm^{-1}, which can be estimated by a simple calculation with constraining the distance or by potential energy along a trajectory (see figure 10). It should be noted too that H_3O^+ and formate ions is not a local minimum energy configuration, when their distance is around the minimum energy distance of the complex. Only when the distance would be more than 0.5 Å longer would it be a local minimum.

All this sums up that depending of reaction path the exchange reaction can have over 7000 cm^{-1} difference in potential energy barrier.

4 Comparing different calculation methods

The large spread of transition state energies between different methods, table 1, in raised a question on accuracy of different methods in general are describing geometries present in trajectories. To get more information in this matter a few trajectories where picked and potential energy was calculated with different methods among them. Some high lights of these calculations are depicted in figures 10, 11 and 12. Basis sets used in these

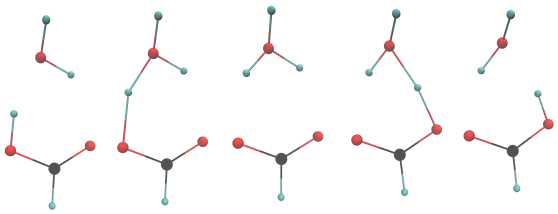

Fig. 6 Hydrogen exchange reaction from left to right after exciting formic acid OH bond.

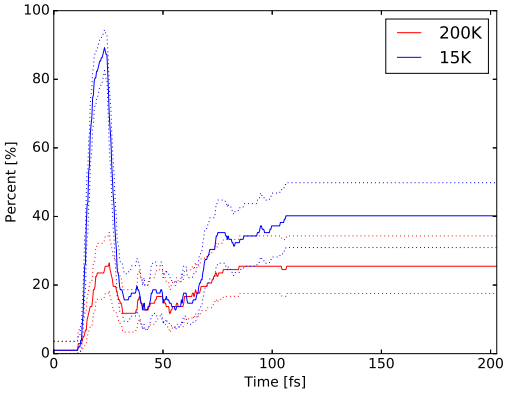

Fig. 7 Hydrogen exchange probability after exciting (532 nm) formic acid OH bond in water complex.

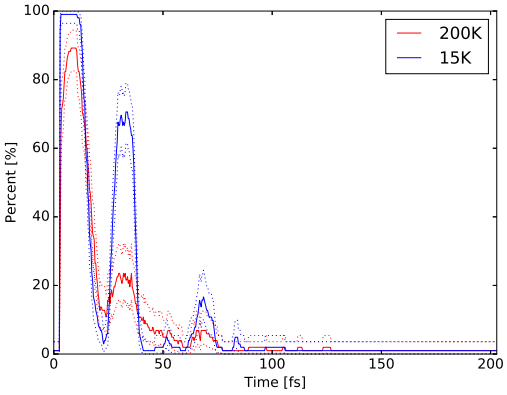

Fig. 8 Chance to find H_3O^+ ion after exciting (532 nm) formic acid OH bond in water complex.

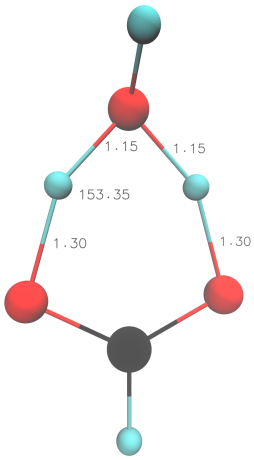

Fig. 9 Transition state geometry for the hydrogen exchange reaction, DLPNO-CCSD(T)/aug-cc-pVTZ. Note that there is a symmetry plane in the middle.

Table 1 Transition state energy comparison for different methods. Dispersion correction (D3BJ) was used with DFT methods.

Method	Transition energy / cm^{-1}
B2PLYP[1]	4952
B3LYP[1]	4811
BLYP[1]	4084
PBE[1]	3102
TPSS[1]	3680
TPSSh[1]	4083
DLPNO-CCSD(T)[2]	5485
MP2[2]	4688

1. ma-def2-TZVPP
2. aug-cc-pVTZ

Table 2 Transition state energy comparison for different basis with BLYP+D3BJ.

Basis	Transition energy / cm^{-1}
def2-SVP	3020
def2-TZVP	3820
def2-TZVPP	4006
ma-def2-SVP	3649
ma-def2-TZVPP	4084
ma-def2-QZVPP	4166

calculations are ma-def2-TZVPP with DFT and aug-cc-pVTZ with MP and DLPNO-CCSD(T). The program used in calculations was ORCA v. 4.0.0.2.

The most important information from these calculations is that ions are problematic. When ever formic acid water complex is in ionic form there is a large spread in potential energy among different methods. While all methods give in practice same results when system is in form of formic acid and water molecules. The energy difference can be as high as 5000 cm^{-1}.

If we make a assumption that DLPNO-CCSD(T) would give the best results, we can then rank the other methods against it. This wound mean that BLYP is the worst method clearly. It does not give the correct potential energy curve shape and it gives energies that can be thousands of wave numbers off of values given by DLPNO-CCSD(T). B3LYP is a large improvement over

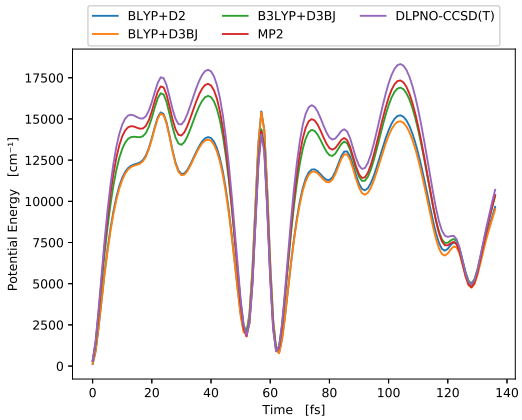

Fig. 10 Potential energy calculated along a trajectory with different methods in formic acid water complex hydrogen exchange reaction. Initial point of this trajectory is sampled from 15 K simulation and it is the point when energy has been added to the system. So this trajectory represents what is visualized in figure 6, as a back and forth reaction. So formic acid and water exist at 0 fs, 45-65 fs and around 130 fs. While the structure is ionic in between.

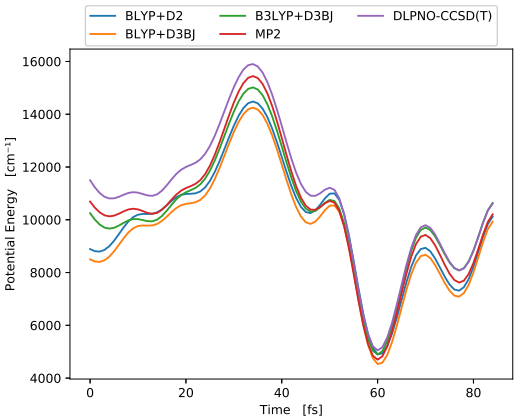

Fig. 11 Potential energy calculated along a trajectory with different methods in formic acid water complex hydrogen exchange reaction.In this trajectory snapshot initial point is near minimum energy transition state and them moves somewhat around it to form formic acid and water around 60 fs, which then goes back to formate and oxonium ions again.

BLYP, but it too fails when system is ionic in form. It does however give the correct shape of potential energy curve. MP2 is within a few exception better option than B3LYP. A special note also to fact that D2 performs better than D3BJ.

For formic acid monomer trajectories, figure 12, the difference between different methods is a lot smaller. Only BLYP gives considerably different values from the other methods. In practice this means that when OH or CH bond is long enough BLYP fails. B3LYP gives very good values for OH bond, but it too will fail a bit on CH bond. But the magnitude of difference to DLPNO-CCSD(T) is of order for few hundred of wave numbers, while for BLYP it can be thousands. But these differences are present only when energy is over 15000 cm^{-1}. MP2 and DLPNO-CCSD(T) on the other hand give in practice same values.

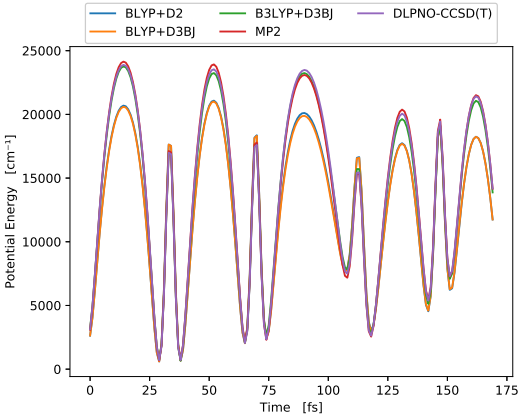

Fig. 12 Potential energy calculated along a trajectory with different methods in formic acid monomer excitation case. Trajectory start from the point when energy is added. Its initial point is sampled from 300 K simulation. So initial potential energy represents thermal excitation at the beginning. Excitation in this trajectory is 532 nm on OH.

5 Discussion

5.1 Monomer

Simulations show conformation change as is observed in experiments when the OH bond is excited, but not at the temperatures used in experiments. This raises a question on role of quantum effects in the process. We already know that transition back from cis to trans happens with tunneling [8] and the whole process is about movement of hydrogen. So we can expect quantum effects, like tunneling and zero-point motion, to be important in trans to cis interconversion too. The fact that we can not see any trans to cis change in simulation when nucleons are treated classically, can be considered as an evidence that not only are quantum effects important, but they are actually crucial for the hole process.

Our simulations showed that increasing temperature increases the probability of the conformational interconversion. This was expected, as formic acid in it's minimum energy configuration is a planar and for symmetry reasons the OH stretch, that is plane symmetric, can not excite torsion, which is not plane symmetric. In quantum nucleons case zero-point motion (and uncertainty principle) distorts molecule a little bit from

plane. Which is somewhat similar to effect of increased temperature.

In the case of CH excitation the importance of zero-point motion is not that clear, as in the simulations the temperature, where initial points of trajectories were generated, had only a minor effect to the final outcome of the simulations. The same symmetry reasoning applies also for the CH stretching mode. This implicates that the CH stretching motion is more strongly coupled to the torsional motion, than the OH stretching mode. Which is also evident based on the finding that the conformational interconversion is much more probable, when excitation is applied to the CH stretching than to the OH.

Because our simulation used classical nuclei, we didn't have tunneling in our simulations. Thus it's expected to need more energy to achieve the conformational interconversion. In our simulation we needed 14000 $cm^{-1}$with excitation on the OH bond, which is about two and a half times more than what is observed experimentally. This difference does sound to be too large effect to be caused by miss of tunneling. As a comparison, in a recent study by Tew and Mizukami [20]. They calculated formic acid vibration overtones and showed that 6th and 7th excited states in torsion-mode tunnel trough barrier to cis conformer. Which in practice meant that barrier of about 4500 cm^{-1}height is effectively only about 3700 cm^{-1}. So we could expect tunneling to lower barrier by about 1000 cm^{-1}.

This could mean that our simulations are to short and running a longer time would show the conformational interconversion happening with less energy. This brings us to the question of role of matrix, which absorbs all the thermal energy [1]. But in what time scale? However dynamics studies of matrix and steric effects of the systems studied here are outside the scope of the current paper.

Third possibility is that we have a wrong excitation. It is assumed that the excitation happens on the OH vibration and that when it happens with 532 nm it excites 6th vibrational state of the OH stretching, based on experimental parameters [21]. But we do not know for sure. Thus it would be good develop a better method to apply an excitation than a simple velocity rescaling.

In addition to repeating simulations with matrix atoms, it might be a good idea to do path integral simulations, to see how much quantum effects matter. These methods have some problems them selfs, but could still be good to see how they differ from purely classical nuclei.

For formic acid monomer the poor performance of BLYP is probably not and issue. Because we did get same results when excitation energy was smaller that the area where BLYP miss performs. But there could be some effect on probability and to how long it takes for conformational interconversion to happen.

5.2 Water complex.

Hydrogen exchange is well along with chemical intuition and it's already studied in many cases [22]. The novelty here is that it can be induced with vibrational excitations and that it can be an intermediate step in a total reaction. But because formic acid is symmetric it cannot be proven experimentally without isotope substitution.

While this study can not provide reason to why in formic acid water complex cis conformer does not tunnel back to trans form. It does imply that mechanism for conformational interconversion very likely includes hydrogen exchange and that this may also be a part of the reason why cis is stable, as was observed by Marushkevich et.al. [9].

A big question for the water complex calculations come from accuracy of the used method BLYP+D2. Normally it would be good idea to do the calculations with a better method. But to do B3LYP calculations with CPMD would need appropriate pseudopotentials, which we do not have. But in the future B3LYP or MP2 calculation should be minimum for the water complex calculations.

Then is the question of, how does the poorly performing method affect results from these simulations. If we look at the figure 10. We see that in that trajectory BLYP does get the shape right, it's only lower. Thus we could expect to get same kind of trajectory, if we just use more energy. So the hydrogen exchange reaction does most likely happen with other methods too. It's only about how much energy it needs and how probable it is. And in any case, this analysis of performance of different methods will prove to be useful in future works regarding the water complex.

6 Summary

The simulation results show that conformational interconversion takes place when OH and CH stretching vibrations are excited, which are in agreement with previous experimental observations. But the simulations also raise questions regarding a role of quantum and matrix effects. For excitations upon the OH vibrational mode, conformational interconversion does not happen at matrix isolation temperatures according to the simulations presented here. This points to the role of zero-point motion. Tunneling is also most likely important, because

in simulations much more energy was needed than what has been shown to work in experiments.

Water complex simulation could not explain explicitly the observed stability of the cis-HCOOH water complex. To address this issue, most likely a simulation with added matrix atoms is needed to mimic the experimental conditions better. In water complex simulations hydrogen exchange reaction was found and it's expected that trans to cis transformation happens via it. Testing accuracy of used method BLYP+D2 raised issues when calculating system when it's in ionic from, which will most likely affect the magnitude of excitation energy needed and reaction probability.

Acknowledgements The CSC - Center for Scientific Computing (Espoo, Finland) is thanked for the computational time allocated to this research. This research was supported by the Academy of Finland research project "Vibrational excitation induced chemistry" (Proj. No 286844) and we (P.D.) gratefully acknowledge financial support from the National Science Center Poland (2016/23/B/ST4/01099).

References

1. M. Pettersson, J. Lundell, L. Khriachtchev, M. Räsänen, Journal of the American Chemical Society **119**(48), 11715 (1997). DOI 10.1021/ja9723621. URL http://dx.doi.org/10.1021/ja9723621
2. A. Olbert-Majkut, J. Ahokas, M. Pettersson, J. Lundell, The Journal of Physical Chemistry A **117**(7), 1492 (2013). DOI 10.1021/jp311749z. URL http://dx.doi.org/10.1021/jp311749z. PMID: 23324029
3. A. Olbert-Majkut, J. Ahokas, J. Lundell, M. Pettersson, Phys. Chem. Chem. Phys. **12**, 7138 (2010). DOI 10.1039/B926658E. URL http://dx.doi.org/10.1039/B926658E
4. A. Olbert-Majkut, J. Ahokas, J. Lundell, M. Pettersson, Journal of Raman Spectroscopy **42**(8), 1670 (2011). DOI 10.1002/jrs.2909. URL http://dx.doi.org/10.1002/jrs.2909
5. K. Marushkevich, L. Khriachtchev, M. Räsänen, M. Melavuori, J. Lundell, The Journal of Physical Chemistry A **116**(9), 2101 (2012). DOI 10.1021/jp209714e. URL http://dx.doi.org/10.1021/jp209714e. PMID: 22280475
6. K. Marushkevich, L. Khriachtchev, J. Lundell, A. Domanskaya, M. Räsänen, The Journal of Physical Chemistry A **114**(10), 3495 (2010). DOI 10.1021/jp911515f. URL http://dx.doi.org/10.1021/jp911515f. PMID: 20166691
7. K. Marushkevich, L. Khriachtchev, J. Lundell, M. Räsänen, Journal of the American Chemical Society **128**(37), 12060 (2006). DOI 10.1021/ja064154b. URL http://dx.doi.org/10.1021/ja064154b. PMID: 16967943
8. M. Pettersson, E.M.S. Maçôas, L. Khriachtchev, J. Lundell, R. Fausto, M. Räsänen, The Journal of Chemical Physics **117**(20), 9095 (2002). DOI 10.1063/1.1521429. URL http://dx.doi.org/10.1063/1.1521429
9. K. Marushkevich, L. Khriachtchev, M. Räsänen, The Journal of Physical Chemistry A **111**(11), 2040 (2007). DOI 10.1021/jp070363m. URL http://dx.doi.org/10.1021/jp070363m. PMID: 17388271
10. A. Olbert-Majkut, J. Lundell, M. Wierzejewska, The Journal of Physical Chemistry A **118**(2), 350 (2014). DOI 10.1021/jp409982f. URL http://dx.doi.org/10.1021/jp409982f. PMID: 24354336
11. R. Car, M. Parrinello, Phys. Rev. Lett. **55**, 2471 (1985). DOI 10.1103/PhysRevLett.55.2471. URL http://link.aps.org/doi/10.1103/PhysRevLett.55.2471
12. D. Marx, J. Hutter, *Ab Initio Molecular Dynamics* (Cambridge, 2009)
13. URL http://www.cpmd.org/. CPMD, Copyright IBM Corp 1990-2015
14. N. Troullier, J.L. Martins, Phys. Rev. B **43**, 1993 (1991). DOI 10.1103/PhysRevB.43.1993. URL https://link.aps.org/doi/10.1103/PhysRevB.43.1993
15. G.J. Martyna, M.E. Tuckerman, The Journal of Chemical Physics **110**(6), 2810 (1999). DOI 10.1063/1.477923. URL http://dx.doi.org/10.1063/1.477923
16. S.D. Ivanov, I.M. Grant, D. Marx, The Journal of Chemical Physics **143**(12), 124304 (2015). DOI 10.1063/1.4931052. URL https://doi.org/10.1063/1.4931052
17. M.E. Tuckerman, M. Parrinello, The Journal of Chemical Physics **101**(2), 1302 (1994). DOI 10.1063/1.467823. URL http://dx.doi.org/10.1063/1.467823
18. P.M. Lee, *Bayesian Statistics An Indroduction*, 4th edn. (Wiley, 2012)
19. F. Neese, Wiley Interdisciplinary Reviews: Computational Molecular Science **2**(1), 73 (2012). DOI 10.1002/wcms.81. URL http://dx.doi.org/10.1002/wcms.81
20. D.P. Tew, W. Mizukami, The Journal of Physical Chemistry A **120**(49), 9815 (2016). DOI 10.1021/acs.jpca.6b09952. URL http://dx.doi.org/10.1021/acs.jpca.6b09952. PMID: 27973803
21. E.M. Maçôas, J. Lundell, M. Pettersson, L. Khriachtchev, R. Fausto, M. Räsänen, Journal of Molecular Spectroscopy **219**(1), 70 (2003). DOI https://doi.org/10.1016/S0022-2852(03)00018-3. URL http://www.sciencedirect.com/science/article/pii/S0022285203000183
22. S. Alavi, M. Taghikhani, Chemical Physics **402**, 105 (2012). DOI http://dx.doi.org/10.1016/j.chemphys.2012.05.004. URL http://www.sciencedirect.com/science/article/pii/S030101041200208X